# ADVANCING THE CLINICAL POTENTIAL OF CARBON NANOTUBE-ENABLED *STATIONARY* 3D MAMMOGRAPHY

Andrew Connor Puett

A dissertation submitted to the faculty of the University of North Carolina at Chapel Hill in partial fulfillment of the requirements for the degree of Doctor of Philosophy through the Joint Department of Biomedical Engineering at the University of North Carolina and North Carolina State University

Chapel Hill
2020

Approved by:

Otto Zhou

Yueh Lee

Jianping Lu

David Lalush

Cherie Kuzmiak

**ABSTRACT**

Andrew Connor Puett: Advancing the Clinical Potential of Carbon Nanotube-enabled *stationary* 3D Mammography
(Under the direction of Otto Zhou)

*Scope and purpose*. 3D imaging has revolutionized medicine. Digital breast tomosynthesis (DBT), also recognized as 3D mammography, is a relatively recent example. *stationary* DBT (sDBT) is an experimental technology in which the single moving x-ray source of conventional DBT has been replaced by a fixed array of carbon nanotube (CNT)-enabled sources. Given the potential for a higher spatial and temporal resolution compared to commercially-available, moving-source DBT devices, it was hypothesized that sDBT would provide a valuable tool for breast imaging. As such, the purpose of this work was to explore the clinical potential of sDBT. To accomplish this purpose, three broad Aims were set forth: (1) study the challenges of scatter and artifact with sDBT, (2) assess the performance of sDBT relative to standard mammographic screening approaches, and (3) develop a *synthetic* mammography capability for sDBT. Throughout the work, developing image processing approaches to maximize the diagnostic value of the information presented to readers remained a specific goal.

*Data sources and methodology.* Sitting at the intersection of development and clinical application, this work involved both basic experimentation and human study. Quantitative measures of image quality as well as reader preference and accuracy were used to assess the performance of sDBT. These studies imaged breast-mimicking phantoms, lumpectomy specimens, and human subjects on IRB-approved study protocols, often using standard 2D and conventional 3D mammography for reference.

*Key findings*. Characterizing scatter and artifact allowed the development of new processing approaches to improve image quality. Additionally, comparing the performance of sDBT to standard breast imaging technologies helped identify opportunities for improvement through processing. This line of research culminated in the incorporation of a *synthetic* mammography capability into sDBT, yielding images that have the potential to improve the diagnostic value of sDBT.

*Implications*. This work advanced the evolution of CNT-enabled sDBT toward a viable clinical tool by incorporating key image processing functionality and characterizing the performance of sDBT relative to standard breast imaging techniques. The findings confirmed the clinical utility of sDBT while also suggesting promising paths for future research and development with this unique approach to breast imaging.

To my beautiful wife, Savannah, who is able to see humor in even the smallest of moments. Thank you for making every day enjoyable. You make me a happier and better person.

To my family, who are a constant source of unconditional love and support. You are my role models and have taught me the importance of working hard and taking care of others.

**ACKNOWLEDGEMENTS**

I feel incredibly fortunate to have joined Dr. Otto Zhou's research team at the University of North Carolina at Chapel Hill in the summer of 2016. By that time, over a decade of work by this group had yielded novel imaging systems for a broad range of applications that were ready for clinical testing. As an MD-PhD candidate, it was an ideal time to join the lab. My mentors have been experts in basic research involving the development of x-ray technologies and clinician-scientists specializing in the translation of new imaging systems to the clinic. I will forever be grateful to Dr. Otto Zhou, Dr. Yueh Lee, Dr. Jianping Lu, and Dr. Christy Inscoe for their guidance and support through my PhD training. Thank you for your investment in me and your incredible mentorship.

Thank you to Dr. David Lalush and Dr. Cherie Kuzmiak for providing me with invaluable feedback over the years. I hope to emulate your dedication to teaching and training.

Thank you to both past and current members of the Zhou lab. My research has built on the work of others, and I have greatly enjoyed collaborating with and getting to know each and every one of you.

Thank you to the UNC MD-PhD leadership team. I am very grateful for your support while navigating this complex training path.

Thank you to Cassandra Houston and Vilma Berg, who have guided me through the administrative side of research. I very much appreciate your kindness and support over the years.

Finally, thank you to my friends, who have helped me enjoy my time outside of the lab.

## PREFACE

Given the potential to identify illness earlier and more accurately through better imaging, research continues into new imaging technologies. At the University of North Carolina (UNC) at Chapel Hill, which has been my undergraduate and now graduate school home, I have had the opportunity to participate in some of these advances. As an undergraduate student in biomedical engineering, I received a Carol Lucas Scholarship, providing me the opportunity to work in an engineering lab. My research experience began with Dr. Paul Dayton. The entire team from post-docs to graduate students included me in their projects. They taught me how to conduct basic research and analyze the results. I learned how to write scientific papers and present my findings as posters and talks, both on campus and at large scientific meetings. Through collaborations with other labs and interactions with physician-scientists, I also learned the excitement of translating research to the clinic. My years with this group changed my life, cementing my desire to pursue a dual MD-PhD degree. It was also during this time that I developed a fascination with nanotechnology, 3D imaging, and the computer processing that creates the 3D images displayed to readers.

As an MSTP-supported MD-PhD candidate, I was honored to stay at UNC for graduate school for two key reasons. First, the UNC School of Medicine offered an innovative approach to medical training, which allowed for the integration of research into a strong clinical experience. Second, I was aware of the commitment of the Joint UNC/NC State Biomedical Engineering Department to become a leader in medical imaging research. As both an undergraduate and a graduate student, I have certainly benefitted from the advanced technologies

and intellectual expertise of the scientists and clinicians brought together at UNC. During my first two medical school years, my interest turned to x-ray imaging, which continues to be the backbone of diagnostic medicine, and I joined the Applied Nanotechnology Laboratory for my PhD work in 2016.

By that time, over a decade of NIH-supported research under the direction of Drs. Otto Zhou and Jianping Lu had resulted in a revolutionary x-ray source using carbon nanotube (CNT) technology. The advantages of these fast and easily controllable x-ray sources for 3D imaging were clear, and the decision had been made to apply them to tomosynthesis, a form of limited-angle 3D imaging. Collaboration with industry allowed a rapid translation of CNT-enabled tomosynthesis to the clinic, and IRB-approved protocols were developed for human studies under the supervision of Dr. Yueh Lee, an MD/PhD-trained translational radiologist.

This has proven to be an ideal environment to train as a clinician-scientist with my interests, allowing me to do basic research on the technology itself and the computer code that processes the images, while also learning how to conduct human studies. My research has focused on evaluating new tomosynthesis imaging systems and developing image processing algorithms to improve their utility. These experiences in basic and clinical research provided the foundation for NIH-funding to complete my dissertation project with an NRSA F30 grant (1 F30 CA235892-01) entitled “Improved cancer screening with synthetic and stationary 3D mammography.”

## TABLE OF CONTENTS

## LIST OF TABLES

## LIST OF FIGURES

### Chapter 2: Literature Review



### Chapter 3: Methodology

**Chapter 4: Findings**

## LIST OF ABBREVIATIONS AND SYMBOLS

| | |
|---|---|
| ° | Degrees |
| κ | Fleiss' kappa |
| μm | micrometer (micron) |
| 2D | Two-dimensional |
| 3D | Three-dimensional |
| 4D | Four-dimensional |
| ACR | American College of Radiology |
| AEC | Automatic exposure control |
| AFV-SIRT | Adapted fan volume modification of the simultaneous iterative reconstruction technique |
| AIP | Average intensity projection |
| Al | Aluminum |
| ANOVA | Analysis of variance |
| AOP | Automatic optimization of parameters |
| ASF | Artifact spread function |
| AUC | Area under the curve |
| BIRADS | Breast Imaging Reporting and Data System |
| BKG | Background |
| BRIC | Biomedical Research Imaging Center |
| CA | California |
| CAR | Caries adjacent to restorations |
| CBCT | Cone beam computed tomography |

| | |
|---|---|
| CC | Craniocaudal |
| CE | Contrast-enhanced |
| CI | Confidence interval |
| CIRS | Computerized Imaging Reference Systems, Inc. |
| cm | centimeter |
| CMOS | Complementary metal-oxide-semiconductor |
| CNR | Contrast-to-noise ratio |
| CNT | Carbon nanotube |
| CT | Computed tomography |
| d’ | Detectability index |
| DES | Dual energy subtraction |
| DQE | Detective quantum efficiency |
| DT | Digital tomosynthesis |
| DBCT | Dedicated breast computed tomography |
| DBT | Digital breast tomosynthesis |
| DCT | Digital chest tomosynthesis |
| DICOM | Digital Information and Communications in Medicine |
| ENH | Enhanced |
| ECS | Electronic control system |
| FDA | Food and Drug Administration |
| FE | Field emission |
| FFDM | Full field digital mammography |
| fSPR | Filtered scatter-to-primary ratio |

| | |
|---|---|
| FWHM | Full-width at half-maximum |
| GE | General Electric |
| HE | High energy |
| HIPAA | Health Insurance Portability and Accountability Act |
| IEC | International Electrotechnical Commission |
| Interp | Interpolation |
| IRB | Institutional Review Board |
| keV | kiloelectron volts |
| kV | kilovoltage |
| kVp | Peak kilovoltage |
| K-edge | Characteristic absorption |
| Kerma | Kinetic energy released in matter |
| LE | Low energy |
| MAR | Metal artifact reduction |
| MA | Massachusetts |
| mAs | milliampere seconds |
| MC | Microcalcifications |
| mg | milligram |
| mGy | milligray |
| MIP | Maximum-intensity projection |
| ml | milliliter |
| MLO | Mediolateral oblique |
| Mo | Molybdenum |

| | |
|---|---|
| MQSA | Mammography Quality Standards Act |
| MR | Magnetic resonance |
| mm | millimeter |
| mSv | millisievert |
| MSER | maximally stable extremal regions |
| MTF | Modulation transfer function |
| NC | North Carolina |
| NIH | National Institutes of Health |
| NNPS | Normalized noise power spectrum |
| NSD | Non-scan direction |
| PET | Positron emission tomography |
| PMMA | Polymethylmethacrylate |
| PSD | Primary sampling device |
| Rh | Rhodium |
| ROC | Receiver operating characteristic |
| ROI | Region-of-interest |
| RTT | Real Time Tomography, LLC |
| SD | Scan direction and Standard deviation |
| sDBT | stationary digital breast tomosynthesis |
| sDCT | stationary digital chest tomosynthesis |
| sDT | stationary digital tomosynthesis |
| sIOT | stationary intraoral tomosynthesis |
| SdNR | Signal-difference-to-noise ratio |

| | |
|---|---|
| SNR | Signal-to-noise ratio |
| SPR | Scatter-to-primary ratio |
| TACT | Tuned-aperture computed tomography |
| TE | Thermionic emission |
| TS | Temporal subtraction |
| UNC | University of North Carolina |
| US | Ultrasound |
| USA | United States of America |
| VRF | Vertical root fracture |
| W | Tungsten |
| WI | Wisconsin |
| (x-y) and z | (planar) and depth directions |

# CHAPTER 1: INTRODUCTION

## 1.1 Problem addressed in this work

Given its ability to identify pathology earlier and more accurately, three-dimensional (3D) imaging has revolutionized medicine. Digital breast tomosynthesis (DBT), now recognized clinically as 3D mammography, is a relatively recent example [Sechopoulos 2013a]. Since early detection is the key to surviving breast cancer [IARC Working Group 2016, Tabar 2015], effective screening and diagnostic imaging approaches are critical. As a result of studies demonstrating an improved diagnostic accuracy when standard two-dimensional (2D) and 3D mammography are combined, the use of DBT has been steadily increasing since its approval by the Food and Drug Administration (FDA) in 2011 [Gao 2017]. As with all commercially-available 3D x-ray devices, DBT works by moving a standard x-ray source through space to collect a series of projection views at oblique angles relative to the target [Sechopoulos 2013a]. The information in these projection views is then combined mathematically using computer algorithms to generate a 3D image [Sechopoulos 2013b]. However, the need to move the x-ray source limits the temporal and spatial resolution of the imaging device and thus the quality of the images presented to the reader [Zheng 2019]. *Stationary* DBT (sDBT) is an experimental approach to breast imaging in which the single moving x-ray source has been replaced by a fixed array of rapidly-responsive and easily-coordinated carbon nanotube (CNT)-enabled sources [Qian 2012]. Hence, sDBT is less prone to the technical limitations of conventional, moving-source DBT and thereby has the potential to present readers with images of greater diagnostic value. However, the novel geometry and performance characteristics of the sDBT system

introduce unique challenges with scatter, noise, and artifact. This dissertation work focused on understanding and addressing these challenges with a goal of exploring sDBT as a tool to improve breast imaging.

## 1.2 Purpose of this work

Given its unique approach to collecting x-ray images, sDBT offers the possibility of generating images with a higher clinical value than the currently-available 3D mammography devices. It was therefore hypothesized that sDBT would provide a valuable breast imaging tool, leading to the stated purpose and title of this dissertation work - advancing the clinical potential of sDBT.

## 1.3 Research questions asked in this work

In order to accomplish its goal of advancing the clinical potential of sDBT, three broad Aims were set forth for this work. Aim 1 involved understanding the challenges of scatter, noise, and artifact related to the unique geometry and operating characteristics of the sDBT system. Aim 2 assessed the performance of sDBT relative to standard 2D and conventional 3D mammography. Aim 3 sought to incorporate a *synthetic* mammography capability into the sDBT system, thereby completing the evolution of this experimental technology to a viable clinical tool. Throughout the project, a key question was constantly asked and studied: Could image processing approaches be developed to improve the diagnostic value of the images that the sDBT system was generating? In this way, the Aims proved to be complementary, as the findings from each influenced ongoing study of the others.

## 1.4 Methodologies used to address the questions asked in this work

The scope of this project, as reflected in its purpose and three Aims (see 1.2 Purpose of this work and 1.3 Research questions asked in this work), required a broad range of experimental

designs. The methodologies ranged from highly-controlled basic research to human studies and included the imaging of breast-mimicking phantoms, lumpectomy specimens, and patients on IRB-approved study protocols (see Chapter 3: Methodology). In large part, this work involved determining the value of the information contained in images generated by sDBT, typically using standard 2D and 3D breast imaging technologies as references for comparison. Many different and previously-validated approaches were used to measure image quality and diagnostic value. These included (1) direct measures of feature properties in the image, such as contrast and signal intensity, (2) objective calculations of feature visibility using detectability indices, adapted to the unique questions raised by the novel sDBT approach to image acquisition, as well as (3) subjective measures of reader preference. When feasible, the diagnostic accuracy of readers interpreting sDBT images was also determined.

### 1.5 Rationale and significance of this work

Early detection is the key to surviving breast cancer [IARC Working Group 2016, Tabar 2015]. As such, research continues to improve the imaging technologies used to screen for and evaluate breast lesions [Krupinski 2019]. CNT-enabled sDBT is an example of this advancing technology [Qian 2012]. Given the fact that pre-clinical testing has demonstrated the potential for a high spatial and temporal resolution [Calliste 2017], this work sought to explore the clinical potential of sDBT, with a goal of maximizing the value of the information presented to readers in sDBT images through improved image processing. It culminated in the incorporation of a *synthetic* mammography capability into the sDBT system. As a result, this work is significant for several reasons:

1. Since future studies comparing sDBT to standard 2D and conventional 3D mammography will almost certainly require the ability to generate a *synthetic* mammogram, the results of this work

are critical for the ongoing clinical research of this novel technology, which has the potential to improve both the detection and diagnostic evaluation of breast cancer.

2. *Stationary* tomosynthesis is being tested across a broad range of clinical applications. In addition to breast imaging, other promising niches include dental [Inscoe 2018, Puett 2018c], musculoskeletal [Inscoe 2020b], chest [Hartman 2016, Lee 2018, Gunnell 2019], and head [Spronk 2020, Luo 2020] imaging. The work presented in this dissertation focuses on breast imaging. However, the issues of scatter, noise, and artifact were actually studied across this spectrum of imaging tasks, with each anatomic environment introducing unique challenges. For example, artifacts are prominent when tomosynthesis is used to image targets containing highly-attenuating features, perhaps best exemplified by dental imaging, given the presence of bone, teeth, and frequently metal. Similarly, scatter significantly degrades the quality of chest imaging. Experience with *stationary* tomosynthesis over this broad range of application has included both pre-clinical experimentation as well as preliminary patient testing (see 2.3.2 Carbon nanotube-enabled x-ray source arrays and *stationary* tomosynthesis). This experience has contributed to the overall understanding of the performance of this novel technology as well as the development of key image processing tools, which will prove useful as *stationary* tomosynthesis continues to be explored at the clinical level for many different imaging tasks. As an example, see APPENDIX: Developing *synthetic* dental radiography. In other words, the findings from this work reflect a foundation of knowledge, applicable not only to breast imaging but also to *stationary* tomosynthesis in general.

3. This work includes a comprehensive comparison of *stationary* tomosynthesis to standard imaging approaches, including 2D full field digital mammography and commercially-available 3D mammography. As such, the findings provide useful insights to guide future research and

development, in terms of both the technology itself as well as the image processing approaches that display its information to readers. The tendency for imaging technology and processing to evolve together, especially as it relates to the sDBT system, is discussed in detail in Chapter 5: Analysis and Synthesis.

## 1.6 Researcher's role and assumptions during this work

The work presented in this dissertation is built on a foundation of basic research laid down over the past two decades in the Applied Nanotechnology Laboratory under the guidance of Drs. Otto Zhou and Jianping Lu. During this time, a large team of technicians, students, and post-doctoral fellows collaborating with industry, had (1) developed a CNT-enabled cathode capable of supporting x-ray production sufficient for human imaging [Calderon-Colon 2009], (2) conceived, designed, and then built *stationary* digital tomosynthesis devices around arrays of CNT-enabled x-ray sources [Qian 2009, Shan 2015], and (3) optimized the performance of these novel devices in pre-clinical testing [Tucker 2013]. Additionally, core image processing code customized to the unique geometry of *stationary* tomosynthesis was developed to generate the tomosynthesis images [Wu 2015]. It was at this point of transition from development to application that I joined the lab in 2016. My research has been determined by the assumptions and discoveries of those before me, as I have continued to study sDBT under the guidance of this team that invented and developed it.

## 1.7 Organization of this dissertation

This dissertation presents work at the intersection of basic experimentation and the clinical application of a novel imaging technology. Hence, clinical context is highlighted throughout, emphasizing the issues in patient care that have guided the research. In **Chapter 2: Literature Review**, the impact of breast cancer in the early 21$^{st}$ century and the potential for

advances in imaging technology, especially 3D mammography, to improve outcomes with this disease are reviewed. Next, the unique imaging approach of CNT-enabled sDBT is explained. This explanation highlights the potential advantages offered by this experimental technology over the currently-available 3D mammography devices while also identifying problematic issues that affect the quality of the sDBT images displayed to readers. Since the development of processing to improve the diagnostic value of sDBT images was a major focus of this work, in-depth reviews of image quality and the image processing chain that generates the displayed sDBT images are provided. Given the scope of this dissertation, many different study designs were utilized (see 1.4 Methodologies used to address the questions asked in this work), ranging from benchtop experimentation to human trials. The details of this broad research approach are provided in **Chapter 3: Methodology**. **Chapter 4: Findings** organizes the results of this work in terms of its three broad Aims: (1) understand the challenges of scatter, noise, and artifact with sDBT, (2) assess the performance of sDBT relative to currently-available 2D and 3D mammography technologies, and (3) incorporate a *synthetic* mammography capability into sDBT. In **Chapter 5: Analysis and Synthesis**, the implications of the findings from this work are reviewed in the context of 3D mammography in general, emphasizing how technology and image processing evolve together, each influencing the advancement of the other. Using the findings from this work, Chapter 5 suggests directions for the ongoing development of sDBT. **Chapter 6: Concluding with a Look to the Future** summarizes the key concepts addressed throughout this work by looking into the future of sDBT. It considers potential diagnostic applications that would take advantage of the unique design of the sDBT system as well as advanced image processing approaches, for which sDBT may be well-suited. Finally, as noted throughout this dissertation, testing the sDBT system was carried out alongside the testing of

*stationary* tomosynthesis across a range of imaging tasks (see 1.5 Rationale and significance of this work and 2.3.2 Carbon nanotube-enabled x-ray source arrays and *stationary* tomosynthesis). The work presented herein was heavily influenced by this broad experience, and as an example, a brief summary of *stationary* tomosynthesis applied to dental imaging is provided (see **APPENDIX: Developing *synthetic* dental radiography**).

# CHAPTER 2: LITERATURE REVIEW

## 2.1 Introduction to Chapter 2: Literature Review

Chapter 2: Literature Review places the work of this dissertation in both its technical and clinical contexts, providing a conceptual framework to understand the motivations that have guided the research as well as the potential implications of the findings. It begins with a discussion of the impact of breast cancer in the early 21$^{st}$ century and the potential for advances in imaging technology to improve outcomes with this disease. Next, the currently-available breast imaging technologies are reviewed, with an emphasis on 3D mammography, which is the clinical designation for digital breast tomosynthesis (DBT). The technical differences between the novel imaging approach of carbon nanotube (CNT)-enabled *stationary* DBT (sDBT) and conventional, moving-source DBT options are detailed. These differences provide the basis to understand the potential advantages of sDBT as well as the challenges that remain in implementing this unique technology at the clinical level. Many of these challenges can be addressed through improved image processing, and therefore, understanding the factors that decrease image quality as well as processing approaches to minimize them is important. Since image processing is a major focus throughout this work, the key processing steps required to generate sDBT images are reviewed. When linked together, these coding steps are referred to as the image processing chain, which in this work, eventually culminates in the generation of reconstructed 3D image stacks and 2D *synthetic* mammograms. Since improved *synthetic* mammography may be the key step by which 3D mammography replaces standard 2D mammography as the breast imaging tool of choice, the *synthetic* mammogram is discussed in

detail. In summary, this chapter presents the background knowledge upon which this dissertation work was built, thereby providing a foundation for understanding the direction of the research as well as the value of the findings.

## 2.2 Breast cancer and breast imaging technologies

### *2.2.1 Breast cancer incidence and impact in the early 21st century*

Breast cancer is by far the most common non-skin malignancy in women, accounting for more than the next two common cancer types (lung and colorectal) combined [Noone 2018]. On average, women in the United States have a greater than 10% lifetime risk of developing breast cancer [Noone 2018]. In 2019, over 250,000 Americans were diagnosed with invasive breast cancer, and more than 40,000 died from the disease [American Cancer Society 2019]. As with all malignancies, breast cancer is a general term that encompasses a variety of different neoplasia types across a wide spectrum of disease aggressiveness and prognosis, reflecting a complex mix of genetic, environmental, and socioeconomic factors [Jardines 2015]. Research continues to understand these influences and their impact on screening and diagnostic testing as well as treatment [IARC Working Group 2016]. Nevertheless, despite these many unknowns, there is at least a consensus that early detection through imaging is the key to improved outcomes for women with breast cancer [IARC Working Group 2016]. In part related to earlier detection through mammography, the 5-year survival rate for breast cancer has increased from about 69% in the period from 1975 - 1977 to about 88% between 2009 - 2015 [American Cancer Society 2019].

### *2.2.2 The value and limitations of breast cancer screening by mammography*

In the 1960s, general x-ray equipment was used to image breast tissue. However, during the 1970s, advances such as customized screen-film mammography devices and breast

compression were introduced, greatly improving the visualization of breast tissue [Gold 1990]. Dedicated mammography units staffed with radiologists specifically trained in the interpretation of the mammogram proliferated through the 1980s and 1990s, and at the turn of the century, digital mammography was introduced, with the landmark study confirming the value of digital mammography being published in 2005 [Pisano 2005]. Currently, digital mammography remains the breast screening tool of choice. The American College of Radiology (ACR) and Society of Breast Imaging recommend annual mammography for all women beginning at age 40 [Mainiero 2017]. This recommendation is based on data demonstrating a significant reduction in breast cancer mortality with mammographic screening [Otto 2011, Hellquist 2011, Tabar 2011]. In fact, early detection of breast cancer through mammography reduces breast cancer mortality by 40%, since women with screen-detected cancers benefit more from therapy than do women with cancers detected clinically [IARC Working Group 2016]. The standard screening protocol involves obtaining two views, cranial-caudal (CC) and mediolateral-oblique (MLO), delivering an effective radiation dose of 0.44 mSv on average [Hendrick 2010]. To put this dose in perspective, Americans are exposed to approximately 3 mSv of environmental radiation annually [Hendrick 2010]. However, since mammograms collapse the 3D breast anatomy into a 2D image, the performance of standard 2D mammography as a screening tool is surprisingly poor. Concerning features can be obscured, resulting in missed or delayed diagnosis, and overlapping features can mimic pathology. As a result, the sensitivity of standard mammography for breast cancer detection averages around 85% [Lehman 2016], and the cumulative risk of call-back for a false positive finding after 10 years of screening is as high as 60% [Hubbard 2011]. Interpreting mammograms of “dense” tissue is especially problematic [Sprague 2016]. A high density refers to a predominance of fibroglandular tissue compared to fat, and breast cancer occurs more

commonly in the dense breast environment [Kerlikowske 2019]. In response to the relatively high recall rates and room for performance improvement associated with standard 2D mammography, intense interest has been focused on 3D breast imaging for years [Vedantham 2015].

### *2.2.3 The advantages of 3D compared to 2D breast imaging*

3D imaging has revolutionized medicine, allowing for an earlier and more accurate detection of disease throughout the body. Without question, 3D breast imaging approaches, including ultrasound (US), computed tomography (CT), magnetic resonance (MR), and positron emission tomography (PET) [Zhang 2018], have improved the characterization and localization of concerning breast lesions. However, these are *diagnostic* applications of imaging. The issues that define a viable *screening* tool are quite different, being centered around the practicality of widespread use. The American Cancer Society recommends 3D imaging by MR for women considered at high risk for breast cancer, identified by genetic testing or a concerning family history [Saslow 2007]. However, the expense, limited availability, and relatively low specificity preclude MR as a general screening tool [Taskin 2018]. Similarly, limited data and issues with image resolution currently constrain the screening value of breast CT [Lindfors 2010]. Until relatively recently, there has been a clinical need for a cost-effective, 3D breast-screening option. Now most commonly referred to as 3D mammography, DBT has been filling this need in the United States since its approval by the FDA in 2011. This approval followed studies demonstrating an improved diagnostic accuracy during screening when both 2D and 3D mammography are combined [Chong 2019].

### *2.2.4 The clinical value and technical limitations of conventional 3D mammography*

3D mammography has been rapidly adopted by breast radiologists following its approval by the FDA for patient care in 2011. In 2014, approximately 30% of breast imaging clinics offered DBT, growing to 65% by 2016 [Gao 2017]. This increased use is supported by studies showing an improved diagnostic accuracy when DBT is combined with standard 2D mammography, including a higher cancer detection rate and a lower call-back rate for false-positive findings [Chong 2019]. Indeed, it is now consensus opinion that DBT provides a better tool than standard 2D mammography for visualizing soft tissue features of concern, such as architectural distortion, asymmetry, and especially breast masses [Chan 2017]. However, microcalcification appearance and clustering are also important, with small, irregular, and tightly clustered microcalcifications being of most concern for cancer [Nalawade 2009], and questions remain regarding reader performance when assessing microcalcifications in DBT images [Horvat 2019]. As a result, breast screening typically involves two separate imaging studies, including standard 2D mammography as well as DBT. By 2016, DBT was used in more than one-third of the screening examinations when available, the majority of which also included standard 2D mammography [Gao 2017]. However, combining 2D and 3D mammography doubles the radiation dose and prolongs the uncomfortable time of breast compression [Ratanaprasatporn 2017]. Hence, research continues to improve the performance of DBT, with a goal of eliminating the need to obtain a standard 2D mammogram at the same time. Appreciating the directions of this research requires an understanding of how DBT works.

DBT is a form of tomography, which is a general term applied to 3D imaging and refers to the fact that 3D imaging devices typically present 3D information as a series of 2D slices through depth. Conventional tomographic x-ray devices, including DBT, work by moving a

standard x-ray source through space to collect a series of projection views from different angles around the target (Figure 2.1). Computer programs combine the information in these projections mathematically to reconstruct the 3D image displayed to readers. Developed in the 1970s, computed tomography or the "CT scan" is the most widely-recognized and most commonly-ordered 3D x-ray study [Power 2016]. During a CT scan, the x-ray source and detector rotate around the target collecting hundreds to thousands of projections. Complicated and expensive machinery is required to accomplish CT, typically delivering relatively high radiation doses [Smith-Bindman 2009]. CT has been adapted for breast imaging, often referred to as Dedicated Breast CT (DBCT). However, DBCT is currently limited by its relatively low spatial resolution and incomplete coverage of the entire breast [Lindfors 2010].

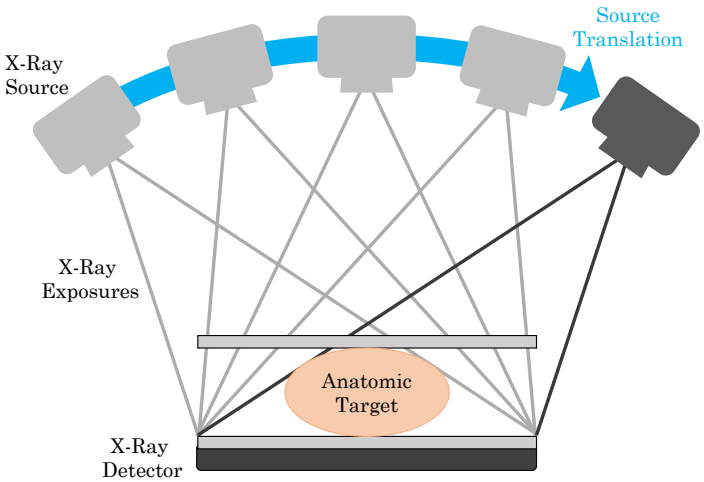


Figure 2. 1. Schematic drawing of the geometry of a conventional digital tomosynthesis system. Note that a single standard x-ray source is translated through space to collect a series of projection views.

Tomosynthesis refers to limited-angle tomography. In other words, fewer projections are collected over a relatively narrow angle span compared to CT. This significantly simplifies the technical demands of the equipment and reduces the radiation dose. First introduced conceptually in the late 1930s, tomosynthesis was the earliest attempt to overcome the primary

limitation of planar imaging, namely the superposition of overlying detail. The result was a series of images on film, referred to as projection views, that could be shifted and superimposed to bring into focus structural details present in the same anatomic plane, as first demonstrated practically by Garrison et. al. [Garrison 1969]. In other words, tomosynthesis is a technique which can capture some 3D information from a limited number of 2D images. The technology underwent a series of ingenious modifications, involving innovations in projection patterns and viewing devices to overlay the projection films [Dobbins 2003]. Interest in tomosynthesis waned through the 1980s, following the introduction of CT, but returned in the 1990s with the incorporation of digital detectors, since the application of computer-based image processing and mathematical reconstruction eased the workload of the reader, improved the diagnostic accuracy of the images, and decreased the required projection number and thus radiation dose of the tomosynthesis scan [Dobbins 2003]. Digital tomosynthesis quickly found niches in which the cost and radiation dose of CT seemed excessive, but planar imaging was often inadequate. Examples included diagnostic evaluations for kidney stones [Liu 2018], chest imaging to look for lung nodules [Ferrari 2018], and breast cancer screening [Sechopoulos 2013a].

In 2011, the FDA approved DBT for patient care. However, work continues to improve DBT, as the performance of each DBT device is limited by the compromises made during its design. Since DBT serves as a breast screening tool, it must deliver a low radiation dose. In fact, DBT delivers a total radiation dose similar to standard 2D mammography, dividing this total dose between the different projection views [Gennaro 2018]. Additionally, the duration of the study must be brief, since breast compression is often uncomfortable and patient movement blurs the image. Testing has shown that the chance of patient motion increases with longer exposure times [Smith 2016]. Herein lies the compromise: optimizing the projection number, angle span,

and information available from each projection within the constraints imposed by the need to move a single x-ray source through space to collect the projection views, maintain a low radiation dose, and complete the study in a short time. Currently, there are seven manufacturers producing DBT devices worldwide, of which four have FDA-approved devices available for use in the United States [The Market Reports 2018, US FDA 2018]. Each design uses a different combination of source motion protocols, projection number and dose per projection, angle span, and source-detector positioning to maximize the diagnostic value of the displayed images [Mackenzie 2017, Vedantham 2015]. In large part, the ongoing design changes seek to minimize the limitations in resolution (see 2.4.2 Contrast and resolution) imposed by the need to move the x-ray source [Zheng 2019].

It was this need for compromise in the design of moving-source DBT that provided the motivation to develop *stationary* DBT, which uses a distributed array of fixed x-ray sources made possible by CNT technology to collect the projection views without source motion (Figure 2.2).

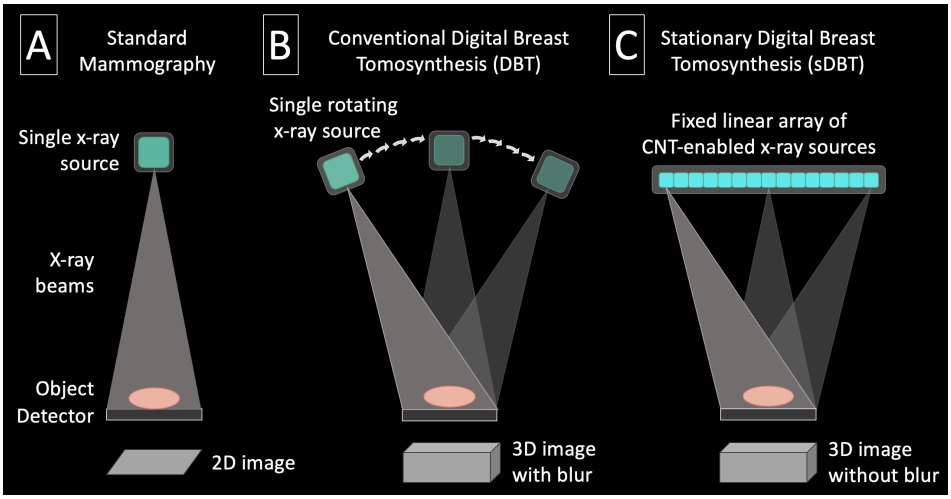


Figure 2. 2. Schematic drawing comparing the system geometries of standard mammography, conventional digital breast tomosynthesis, and carbon nanotube-enabled *stationary* digital breast tomosynthesis (sDBT). Whereas standard mammography (A) results in a single 2D image of the

3D breast anatomy, tomosynthesis can produce a 3D image. However, since conventional DBT systems (B) must move the x-ray source, the 3D image can be compromised by blur. In contrast, sDBT (C) uses a fixed and distributed array of carbon nanotube (CNT)-enabled x-ray sources, allowing for the production of a blur-free 3D image.

## 2.3 Carbon nanotube enabled *stationary* digital breast tomosynthesis (sDBT)

### *2.3.1 Making x-rays*

#### *2.3.1a The standard thermionic x-ray source*

The medical community quickly recognized the potential of x-ray imaging to visualize pathology. Wilhelm Conrad Roentgen reported the penetrating properties of these rays that he discovered in November 1895 [Roentgen 1896]. Within months, devices capable of generating x-rays were being installed in medical facilities across Europe and North America [NDT 2014]. Imaging a wrist at Dartmouth College in Hanover, New Hampshire provided one of the first medical x-rays in America [Michaelides 2009], and the fact that x-ray imaging would change the course of medicine was demonstrated dramatically in Canada soon thereafter. Tolson Cunning was shot in the leg in December, 1895 in Montreal, and an initial surgery failed to locate the bullet [Thali 2002]. After learning about a demonstration of x-ray imaging by Professor John Cox at McGill University, Cunning's surgeon, Dr. R. C. Kirkpatrick, turned to Cox for help. A 45-minute exposure to x-rays showed the bullet to be lodged between the tibia and fibula, guiding a successful second surgery [Thali 2002]. Along with the introduction of anesthesia and antibiotics, x-ray imaging was a defining moment of modern medicine. In recognition of this fact, the Nobel Prize for Physics was commissioned in 1901, with Roentgen being its first recipient [Nobel Media 2020].

Roentgen studied x-rays using a Crookes tube [Nascimento 2014], which is a partially-evacuated glass container containing a cathode and an anode. Applying a voltage between these

two electrodes generates a current of electrons that produce a greenish fluorescence and x-rays (Figure 2.3) on interaction with the glass [Behling 2015].

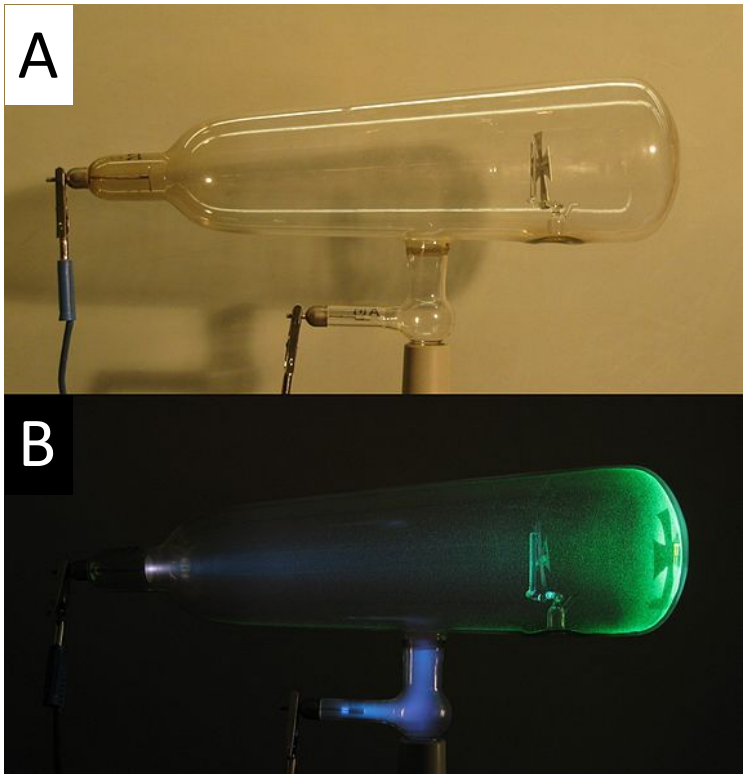


Figure 2. 3. Photographs of a Crookes tube, similar to the device used by Roentgen to characterize the x-ray. The Crookes tube (A) consists of a negatively-charged cathode (metal disk at left) and a positively-charged anode (at the base) encased in glass tube. Applying a voltage between the electrodes results in electron emission from the cathode, resulting in a greenish fluorescence as the electrons interact with the glass (B). Note the shadowed cross, demonstrating that the electron flux travels from the cathode. These pictures have been shared in the public domain by D-Kuru via Wikimedia Commons.

Patented in 1913, the "Coolidge tube" represented a major advance in x-ray source design (Figure 2.4) [Nascimento 2014]. In this tube, a tungsten filament was used as the source of electrons, and Coolidge's discovery that heating the metal cathode greatly increased the number of available electrons has remained the basis of virtually all diagnostic and therapeutic x-ray devices used clinically since then. Indeed, advances in hardware have greatly improved the

safety of x-ray machines. However, the process of generating x-rays for biomedical imaging has changed very little over the past century.

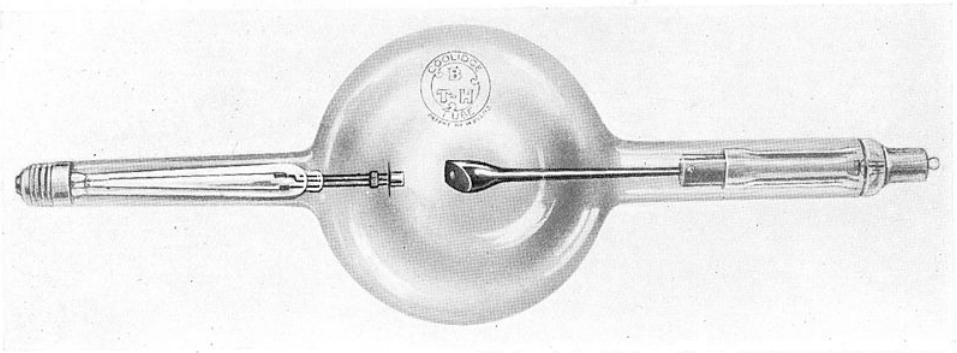

[*By permission of Messrs. The British Thomson-Houston, Ltd.*
A Coolidge X-ray Tube for producing X-rays.

Figure 2. 4. A drawn depiction of the Coolidge tube as it appeared in the early 1900s. Although the basic arrangement is similar to the Crookes tube (Figure 2.3), the use of a heated tungsten cathode dramatically increased the electron flux and thus x-ray production. This approach of heating a cathode to "boil off" electrons, known as thermionic emission, has remained the basis of medical x-ray devices for the past century. This drawing has been shared under the Creative Commons Attribution 4.0 International license.

Heating a metal cathode filament to temperatures greater than 1000ºK excites or energizes electrons over the potential energy barrier-of-escape. This process is known as thermionic emission (TE). Once available, the electrons are accelerated toward a metal anode. The number and energies of these electrons determine the final x-ray profile and are used to define the operational settings of the x-ray tube. The electron flux moving from the cathode to the anode is the tube current (measured in milliamperes), which multiplied by the on-time (measured in seconds), defines the exposure (mAs). It is controlled by filament heating. The kinetic energy of the moving electrons results from the voltage set up between the cathode and anode, with this voltage differential defining the maximum electron energy and thus penetrating potential of the x-rays. For human imaging use, kilovolt energies are required, and the peak voltage (kVp) is the other basic operational tube setting. The accelerated electrons lose energy

when they interact with the anode. Most is released as heat, but approximately 0.03% of the primary electron energy contributes to the diagnostic x-ray beam [Behling 2015]. The energy spectrum of these x-rays is adjusted using metal filters to remove the low energy photons incapable of penetrating the target, since these photons can deposit in tissue, carrying risk, without providing any imaging value. Additionally, the x-ray beam is collimated or shaped to the target, to minimize exposure to surrounding tissues.

The long experience with TE has produced reliable x-ray sources for a tremendous variety of both diagnostic and therapeutic devices. However, given the technological difficulties in coordinating multiple TE sources, as a result of their high operating temperature and power consumption, standard x-ray tubes impose limitations when repetitive imaging must be obtained quickly, as with 3D imaging [Zhou 2010].

*2.3.1b Carbon nanotube cathodes and field emission*

A new x-ray source, based on CNT technology, has emerged over the past two decades. Research in the mid-1990s demonstrated the capacity of CNTs to release electrons by field emission (FE) [Bonard 2001]. FE is a quantum phenomenon quite different from TE, in which the application of an electric field allows electrons to "tunnel" through the potential energy barrier. FE occurs almost instantaneously and at room temperature [Parmee 2015]. CNTs are well-suited as field emitters for an x-ray source. They are durable, and their high aspect ratio (length to width) significantly reduces the work of electron extraction, since the electric field concentrates at the nanotube tips [Parmee 2015]. Although the potential advantage of a compact electron source with fast on-off times for medical imaging was recognized early, nearly a decade of research in the Applied Nanotechnology Laboratory at the University of North Carolina was required to produce a CNT cathode capable of generating the tube currents needed for human use

[Puett 2018a]. Step by step, the techniques to achieve appropriate CNT lengths, density, and distribution and a stable CNT attachment over an area of several square millimeters were developed [Calderon-Colon 2009]. Currently, this fabrication process is producing CNT cathode arrays on a commercial scale (Figure 2.5).

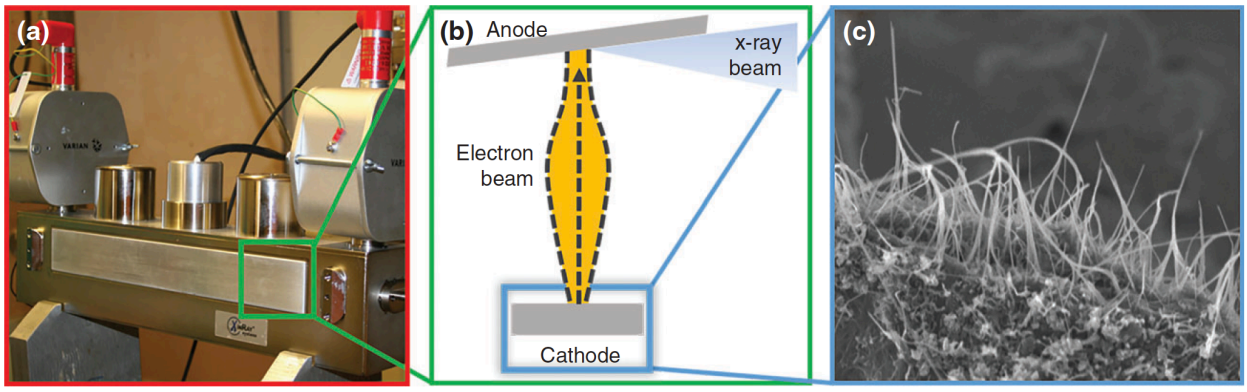


Figure 2. 5. Photographs and a schematic drawing of a carbon nanotube (CNT) cathode, a single CNT-enabled x-ray source, and an x-ray tube containing a fixed array of these CNT-based sources. The aluminum x-ray window, access ports, and ion pumps can be seen in this photograph of a sealed tube (a). The tube contains an array of 31 fixed and separate x-ray sources (b), each of which uses field-emission to release electrons from a CNT-based cathode. Figure adapted from [Puett 2018a].

Multi-walled CNTs measuring 3-8 nanometers in outer diameter are grown via a thermal carbon vapor deposition process. Vacuum annealing followed by mechanical removal of the top surface layer yields a vertically-aligned CNT field that is surprisingly uniform in CNT density and length [Calderon-Colon 2009].

CNT cathodes require a unique operating environment. The CNT-enabled x-ray source is a triode or 3 electrodes operating in a sealed space. The gate electrode and focusing structures sit between the CNT cathode and the metal anode. Unlike the thermionic x-ray source, in which the tube current is controlled by heating the metal cathode filament, the tube current in the CNT-based x-ray source is controlled by adjustments in the voltage between the gate and cathode. A 1-2 kV gate voltage is typically required to extract electrons at a rate adequate to achieve the

tube currents needed for human imaging. Approximately 60% of the available electrons pass through the gate and are accelerated by the anode voltage, which can vary from around 30 kV for mammography to 140 kV for chest imaging. CNTs are quite sensitive to arcing events or "shorts" between electrodes. These currents are carried by ions produced from the heated tube components or environmental contaminants. To minimize the arcing risk, the source tube containing CNT cathodes is sealed and maintained in a strict vacuum of $<10^{-8}$ torr. Sealed tubes containing CNT-based cathodes have proven to be quite durable x-ray sources, demonstrating a stable gate voltage to maintain the tube current over an estimated 2.5 years of clinical use [Sprenger 2011].

### *2.3.2 Carbon nanotube-enabled x-ray source arrays and stationary digital tomosynthesis*

The CNT-enabled x-ray source is ideal for the repetitive imaging steps needed to accomplish 3D imaging. It is fast and operates at room temperature, eliminating the need for much of the supporting equipment required with standard x-ray tubes. Additionally, since simple voltage manipulation is all that is needed to control x-ray production, the function of multiple individual sources can be easily coordinated. As such, fixed arrays of sources can be built with tremendous flexibility in their distribution, thereby offering a solution to the limitations imposed by the need to move thermionic x-ray sources through space to collect projection views. Recognizing the advantages of a fixed, distributed CNT-enabled source array for tomosynthesis led to the concept of *stationary* digital tomosynthesis, and collaboration with industry allowed the construction of sDT devices customized to different imaging tasks (Figure 2.6) [Puett 2018a]. Two sDBT devices were available for study during this dissertation, including the first-generation sDBT device now involved in human trials (Figure 2.6) [Lee 2019] and a second-

generation sDBT device for laboratory experimentation [Calliste 2017]. The sDBT devices differ primarily in their achievable dose rates, peak energies, and angular spans [Calliste 2017].

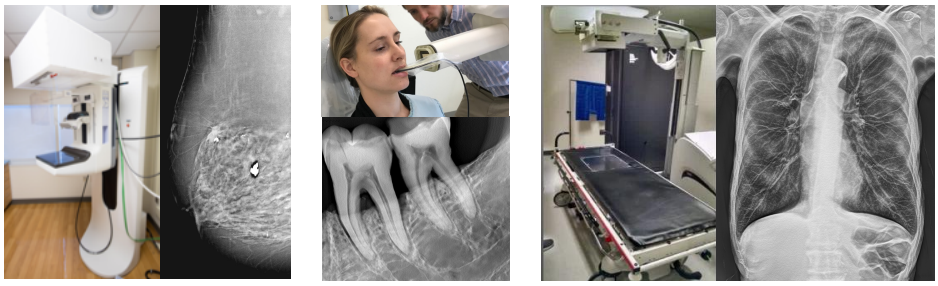

stationary Digital Breast Tomosynthesis (sDBT) | stationary Intraoral Tomosynthesis (sIOT) | stationary Digital Chest Tomosynthesis (sDCT)

Figure 2. 6. Representative examples of experimental carbon nanotube-based *stationary* digital tomosynthesis devices that are currently involved in human studies. The *stationary* digital breast tomosynthesis (sDBT), *stationary* intraoral tomosynthesis (sIOT), and *stationary* digital chest tomosynthesis (sDCT) systems utilize different geometries and supporting equipment, customized to the imaging task. Example images from human study are displayed next to each device. Figure adapted from [Puett 2018a].

In addition to the two sDBT devices, a seven-source linear tube with an angle span of 12° has been developed for dental imaging [Inscoe 2018]. This imaging system was designated *stationary* intraoral tomosynthesis (sIOT), with "intraoral" referring to the location of the detector in the mouth (Figure 2.6). Experience with sIOT had a direct impact on the work carried out with sDBT, which in turn heavily influenced the development of customized image processing approaches for sIOT (see APPENDIX: Developing *synthetic* dental radiography). More specifically, work with sIOT was integral to the development of dense-feature artifact reduction techniques as well as recognition of the potential value of displaying multi-view images (see 3.5.3 Processing images).

The application of *stationary* tomosynthesis to chest imaging introduced unique challenges, especially with scatter. Pre-clinical testing using chest-mimicking phantoms, pig lungs, and cadaveric human lungs as well as early IRB-approved and HIPAA-compliant trials on

patients with cystic fibrosis [Hartman 2016, Lee 2018, Gunnell 2019], lung nodules (Clinical Study Identifier: NCT02075320) [Hartman 2016], and cardiac calcifications (Clinical Study Identifier: NCT03169062) have been carried out using a repurposed tube of CNT-enabled x-ray sources incorporated into a standard chest imaging configuration. These initial studies with *stationary* digital chest tomosynthesis (sDCT) have laid the foundation for an NIH-supported study (grant: 1R21CA216780) to study scatter during sDCT imaging [Inscoe 2020a]. Musculoskeletal imaging to improve the detection of fractures is also a promising area for *stationary* tomosynthesis, and early experience with this approach is now available [Inscoe 2020b]. The most recently developed CNT-enabled system for head imaging contains multiple linear arrays of x-ray sources that are arranged to cover the angular span necessary for complete "CT" imaging [Spronk 2020, Luo 2020]. Although still considered experimental, CNT-enabled devices have demonstrated a reliable performance across this broad range of clinical applications. In fact, the sDBT systems utilized for this dissertation work and the sDCT device have been operational for more than 5 years in pre-clinical testing and now human studies [Tucker 2013, Lee 2019, Shan 2015, Inscoe 2020a]. Additionally, the FDA has recently approved the first CNT-enabled device for human imaging. This single-source portable x-ray machine is now operational in hospitals [Pesce 2017].

## 2.4 Defining and measuring the quality of the digitized image

### *2.4.1 Digital radiography*

Without question, digitization has revolutionized medical imaging, allowing for the easy storage and transfer of image data, and importantly, the opportunity for post-acquisition processing. Digital radiography is made possible by flat-panel x-ray detectors, which consist of a 2D matrix of pixel elements. The advances in detector technology over the past 15 to 20 years

have been dramatic and are quite directly responsible for the renewed viability of tomosynthesis. At a general level, digital detectors convert the energy from an x-ray photon into an electric signal that is passed to a computer. For breast imaging detectors, pixels typically have a footprint of just 70-100 μm, permitting the resolution needed to characterize microcalcifications. As such, the average flat-panel detector measuring around 25 cm per side will contain upwards of 10 million pixels.

Many measures are used to characterize detector performance. However, the detective quantum efficiency (DQE) provides a useful metric, as it quantifies how well the detector collects and then passes on the information from incoming photon signals. In a broad sense, DQE compares the signal-to-noise ratio (SNR) of the incoming signal to the readout signal. More specifically, it measures the detector's influence on image contrast, noise, and resolution, taking account of the strength of the incoming signal (x-ray photon density). The detector pixel size is also an important determinant of system performance, as it defines a theoretical limit of spatial resolution. As noted above, pixel sizes in the range of 70-100 μm are used for breast imaging, since characterizing microcalcifications requires this level of resolution. Finally, the readout rate or time required to transfer the pixel-by-pixel information to the computer is important, especially for imaging modalities such as sDBT. Given the potential for fast scan times, the detector readout rate may prove to be a rate limiting step for image acquisition during sDBT, since each projection view must be read out sequentially.

### *2.4.2 Contrast and resolution*

Medical radiography can be summarized as the process of capturing anatomic detail in a visual image. The overall performance of an x-ray system is best judged by its final product, namely a displayed image of high quality. High quality is a non-specific descriptor, but in a

broad sense, a high-quality image presents information in a way that maximizes the chance that a trained reader will make an accurate diagnosis. Interpreting the anatomic and pathologic detail displayed in an image involves recognizing patterns. The clarity or visibility of the pattern is a direct result of the resolution and contrast of the image. Resolution and contrast define image characteristics that allow a region-of-interest, such as an anatomic detail, to be distinguished from its background. Contrast defines the intensity of a feature relative to its immediate surroundings, while resolution defines the ability to distinguish two independent features as separate. As such, resolution refers to the "distinctness" of the edge that separates a feature from its surroundings and is often described as the "crispness" or "sharpness" of an image. Resolution and contrast are quantifiable and can therefore be used to compare the quality of one image to another.

Contrast results from the relative absorption of x-ray photons as they interact with components of the anatomic target. As such, contrast is dependent on the energy spectrum of the x-ray beam as well as the physical properties of the target itself. The extent of photon absorption is defined mathematically by the attenuation coefficients of the target components. Optimizing contrast during image acquisition primarily involves selecting appropriate tube settings (mAs and kVp). The goal is to minimize or at least correct for those factors that limit contrast, primarily scatter and noise. As discussed below, tomosynthesis presents unique challenges with regard to these issues (see 2.5 Image quality problems inherent to tomosynthesis in general and sDBT in particular).

Unlike contrast, which is an inherent property of the object being imaged, resolution is primarily dependent on the imaging system. In large part, resolution reflects geometry and is a result of the relative sizes and locations of the x-ray source focal spot on the anode, the feature-

of-interest being imaged, and the detector pixel. Figure 2.7 demonstrates these geometric relationships.

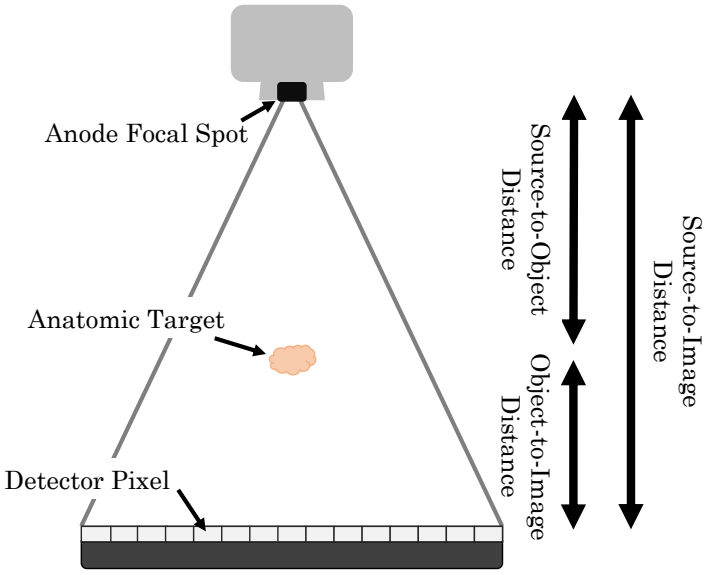


Figure 2. 7. A schematic drawing identifying the key physical parameters and geometric relationships that determine the resolution of an x-ray imaging system. For a stationary source, resolution is primary determined by the sizes and locations of the anode focal spot, the detector pixels, and the anatomic target. However, blur can be introduced in the detector or by movement of the x-ray source or target during the scan, which can degrade resolution.

From an image acquisition standpoint, achieving good resolution involves selecting an appropriate equipment design (focal spot size, separation distances, and detector properties) for the given task, while minimizing factors that compromise resolution, such as motion-related blur.

### *2.4.3 Scatter and noise*

Scatter and noise degrade image quality and are problematic for all x-ray imaging systems. However, unique challenges arise with scatter and noise during digital tomosynthesis [Wu 2009] (see 2.5 Image quality problems inherent to tomosynthesis in general and sDBT in particular). Diagnostic imaging typically utilizes x-ray photons in the energy range of 20 to 150 kVp. In this range, the two predominant interactions between the photon and the atoms of the target are the photoelectric effect and scatter [Bushberg 1998]. The photoelectric effect refers to

the disappearance of the x-ray photon as its energy is absorbed by a target atom. Its energy is imparted to the electron cloud, displacing an electron and leaving the atom in an ionized state. Non-absorbed, or primary, x-ray photons pass through the target and are collected by the detector. Image contrast results from the relative differences in photon absorption across the target. However, x-ray photons can also deflect off target atoms. Most commonly, this interaction is inelastic, meaning that the x-ray photon loses some of its energy and travels off in a different direction. This interaction is known as Compton scattering, named after Arthur Compton, who described it in the early 1920s [Bushberg 1998]. Since the deflected photons follow an unexpected path to the detector, they result in image patterns that do not correspond to the actual structure of the target. The chance that a photon will be scattered depends on its energy, the density of the target, and the distance that the photon travels through the target [Marchiori 2004].

X-ray machines are electronic devices, and given the stochastic behavior of electrons and photons, their operation is associated with noise. Noise is best considered as random fluctuations in a signal, and it is present in both the x-ray emission and digital detector. X-ray noise is known as "quantum," reflecting the inherently probabilistic nature of photon generation and interactions. Detector noise is referred to as "electronic," since it originates predominantly in the electronic circuitry. For x-ray devices operating at higher energies (> 50 kVp) and dose, typical of most general radiography, the quantum noise component predominates, and the system is referred to as quantum limited. However, DBT typically operates at lower energies, and the dose is divided between many sources. As a result, the signal reaching the detector (the photon flux) is relatively low, allowing for a more predominant electronic noise effect. Hence, optimizing the performance of a DBT system in large part involves determining the most appropriate x-ray tube

operation in order to balance noise and total dose. Important factors include the tube current and anode voltage, projection view number and span, the distribution of dose among sources, and timing of source exposures. Intuitively, collecting as many projection views as possible or perhaps concentrating the dose in the most central projection views may be expected to improve image quality. However, because of detector noise, this is typically not the case. For example, sDBT performance testing prior to its clinical implementation included assessments of the signal-to-noise ratio (SNR) in many system configurations and demonstrated that the use of 15 of the available 31 sources with dose divided equally across the entire span was optimum for image quality [Tucker 2013].

### *2.4.4 Feature visibility*

There is no perfect x-ray image, as processing the information for display involves tradeoffs between contrast and resolution. Noise limits contrast, and as such, removing the noise signal is preferable. However, adjusting image information is known as filtering, and all filtering comes at a price. For example, noise is a high-frequency image component, but so are edges. As such, suppressing noise can lower resolution. It is therefore best to consider image quality in a more global sense. A high-quality image is one that provides the most-useful clinical information. In other words, a high-quality image presents information in a way that maximizes the chance that a trained reader will make an accurate diagnosis. This is a task-specific definition. For example, the optimum balance of contrast and resolution to display a breast mass in a mammogram may be quite different from the balance that best displays a microcalcification. As such, defining image quality at the clinical level involves measuring the visibility of specific features. The visibility or conspicuity of an image feature can be quantified through the calculation of detectability indices [Gang 2011] as well as assessments of trained reader

performance and preference [Peppard 2015] during image interpretation. Detectability indices integrate the primary determinants of image quality, including contrast, noise, and resolution, with a task function for a particular feature within the image [Gang 2011]. Determining feature visibility played a key role in the work detailed in this dissertation (see 3.6.1 Measuring image quality and quantifying feature detectability).

## 2.5 Image quality problems inherent to tomosynthesis in general and sDBT in particular

### *2.5.1 Motion blur degrades resolution*

Motion of any type during image acquisition introduces blur and degrades image quality. As such, resolution is inherently problematic with conventional or moving-source DBT. Continuous source motion effectively elongates the focal spot in the direction of motion, thereby decreasing resolution [Zheng 2019]. To overcome this technical limitation, some DBT devices use a step-and-shoot approach [Vedantham 2015]. Stopping the x-ray source at image acquisition solves the problem of source blur but takes longer, increasing the chance that the patient will move [Acciavatti 2012], which again introduces blur. In short, the need to move the x-ray source imposes limitations, forcing compromises in design. However, since CNT-enabled sDBT uses a fixed array of rapidly-responsive and easily coordinated sources, a wide angle of projection views can be collected quickly and without source motion [Tucker 2013]. The resolution of an imaging system can be quantified, providing a key metric to compare different systems [Marshall 2012]. The modulation transfer function (MTF) is a standard measure of resolution [EUREF 2018]. In essence, MTF relates contrast (regional intensity differences) to frequency in an image. Rapidly-changing intensities, such as those encountered at an edge, consist of high-frequency information, while smooth areas with little intensity change represent low-frequency information. As such, the MTF quantifies the relative contrast at a particular spatial frequency

for a given system. Pre-clinical testing has demonstrated that sDBT can offer a higher spatial resolution compared to the moving-source DBT system from which it was constructed [Calliste 2017].

### *2.5.2 Scatter limits contrast*

Scatter is a significant problem during medical imaging. In fact, for many diagnostic studies, especially if the target includes dense features, most photons reaching the detector have been scattered. Scatter is certainly problematic during breast imaging. For example, the scatter-to-primary (SPR) of x-ray photons during standard mammography ranges from 0.1 to 1.1, correlating most strongly with breast thickness and density [Boone 2000]. For this reason, scatter reduction techniques, including the use of anti-scatter grids and creating an air gap between the target and detector, are typically employed as a part the standard mammography protocol. These techniques work by removing or excluding photons following angled paths and therefore more likely to have been deflected. However, since the reconstruction of 3D information by tomosynthesis is based on acquiring angled projection views, anti-scatter grids and air gaps are problematic. As such, the SPR in DBT images can be greater than 1.5, again depending primarily on breast thickness [Sechopoulos 2007]. Additionally, since tomosynthesis involves collecting projection views from different positions relative to the target, photons pass through different tissues and have different path lengths, depending on the projection angle. As a result, the extent of scatter varies across the span of projection views [Sechopoulos 2007]. For these reasons, image processing steps after image acquisition are being explored to correct for scatter in DBT images, and developing scatter-correction algorithms for DBT is an area of active research by many groups (see 3.5.3b Creating scatter maps, 4.2.1 Quantifying scatter in contrasted and non-

contrasted sDBT images, and 4.2.2 The effect of scatter correction through processing on sDBT image quality).

### *2.5.3 Limited sampling introduces artifact*

Artifact in radiography is best considered as a spurious or distorted appearance of a structure in the image. Similar to scatter and noise, there are problems with artifact unique to digital tomosynthesis. Artifact can be introduced during both image acquisition and post-acquisition processing and includes blur related to x-ray source and patient motion, detector lag and ghosting, and reconstruction effects. As noted above, CNT-enabled *stationary* tomosynthesis is specifically designed to minimize blur caused by source and patient motion, taking advantage of its ability to acquire multiple images quickly using a distributed array of fixed x-ray sources. However, reconstruction artifacts remain a problematic issue, as they result from the mathematical attempts to recreate a 3D image space despite working with an incomplete sampling of the target.

Tomosynthesis refers to limited-angle tomography. In other words, a relatively small number of 2D projections are collected over a relatively small angle-span. Computer algorithms known as "reconstruction" use the information present in these projection images to generate the 3D image displayed to readers for interpretation (see 2.6 The image processing chain that generates sDBT images and the value of the *synthetic* mammogram). However, given the incomplete information available from the limited sampling of the target space, reconstruction is inherently problematic and associated with artifact. There are many different types of reconstruction artifact, related primarily to the physical properties of the object being imaged as well as the type of reconstruction algorithm used to generate the 3D image [Geiser 2018, Kim 2016]. Both in-plane shadowing and out-of-plane rippling can be prominent in the reconstructed

images [Geiser 2018]. Artifacts associated with highly-attenuating features, especially metallic hardware, can be prominent in tomosynthesis images. In DBT, artifact is present around breast calcifications and metal, the latter including clips from previous procedures and the needles and wires used to indicate lesions of concern (Figure 2.8) [Puett 2019a].

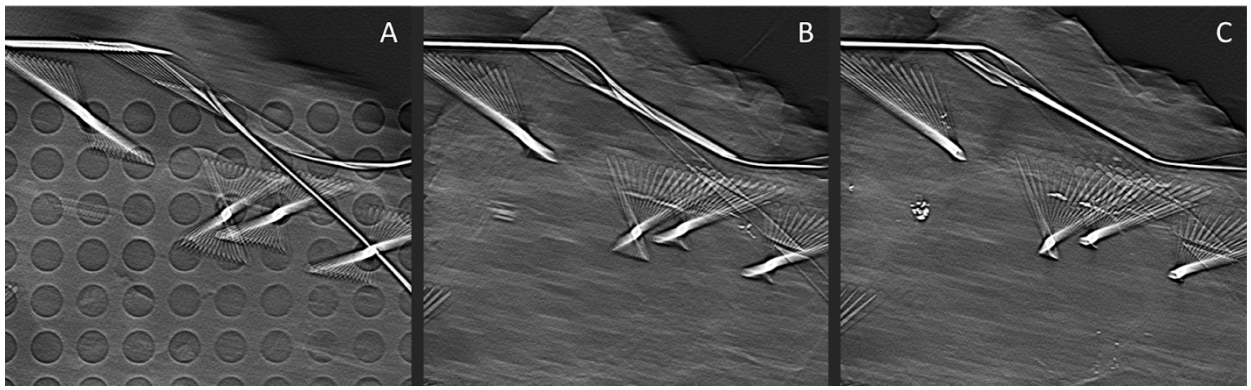


Figure 2. 8. Examples of the "slinky" appearance of metal artifact in *stationary* digital breast tomosynthesis (sDBT) images of a lumpectomy specimen containing metal needles and wires used to guide biopsy. These image slices were selected from different depths [(A) 2.8 cm, (B) 3.7 cm, and (C) 4.3 cm] in the reconstructed 3D image stack through which the reader scrolls to identify pathology and appreciate depth relationships. Figure adapted from [Puett 2019a].

As with the issues of scatter and noise, the development of image processing approaches to minimize artifact in tomosynthesis images is an area of active research (see 3.5.3c Reducing artifact and 4.2.3 Artifact reduction in reconstructed and *synthetic* sDBT images).

## 2.6 The image processing chain that generates sDBT images and the value of the *synthetic* mammogram

The ability to manipulate the information displayed in an image using computer algorithms is a significant advantage of digital radiography compared to film. Indeed, digital image processing is directly responsible for the renewed clinical viability of tomosynthesis. As with all x-ray-based 3D medical imaging approaches, the final images displayed to the reader for interpretation following a DBT study are the product of extensive computer processing. Typically, DBT information is displayed as a stack of image slices through which the reader

scrolls, allowing appreciation of the changing appearance of image features through depth. However, it is now accepted that displaying not only the 3D image stack but also *synthetic* 2D slab images and even a complete *synthetic* 2D mammogram has clinical value. *Synthetic* slabs and *synthetic* mammograms integrate or synthesize the information in the 3D image stack back into single 2D images. Although it may seem counter-productive to generate 2D images after going through the many technical and processing steps to produce a 3D image stack, there are a host of benefits. First, *synthetic* mammograms allow a direct comparison to previous standard mammograms. Second, *synthetic* mammograms provide a global view of the breast anatomy, which can guide attention to key areas when reviewing the stack of reconstructed image slices. Since this stack can include many dozens to more than 100 image slices, depending on the thickness of the compressed breast, there is a risk of reader fatigue. As such, an initial global assessment is helpful. Third, generating the *synthetic* mammogram provides an opportunity to identify and emphasize specific feature characteristics through processing, potentially improving the ability to identify pathology. Finally, since individual microcalcifications may appear in different slices through the reconstructed 3D image stack, it is easier to appreciate the spatial association or clustering of microcalcifications in 2D *synthetic* images, which is clinically important, since microcalcification clustering provides an important diagnostic clue regarding the potential for a breast lesion to be malignant [Sickles 2013]. In fact, the ability to generate a diagnostically-useful *synthetic* mammogram is an area of quite active research, since it should eliminate the need to collect standard mammograms at the same time as the DBT study. The sequence of computer algorithms that generate the 3D and then 2D images for DBT is known as the image processing chain, and it typically involves 4 general steps: projection image

correction, reconstruction, feature enhancement, and forward projection (Figure 2.9) [Puett 2019b].

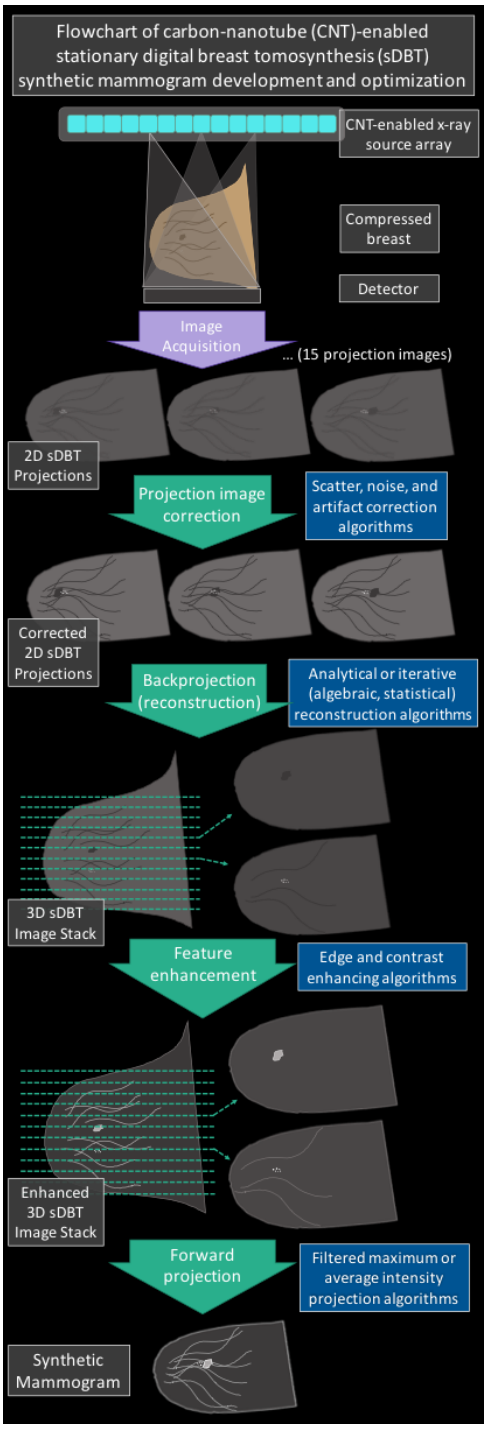


Figure 2. 9. Schematic drawing of the key processing steps and flow of information through an image processing chain to produce a *synthetic* mammogram for stationary digital breast tomosynthesis (sDBT). The *synthetic* mammogram is a mathematical construct generated by an

image processing chain with 4 key computational steps (green arrows): correction of the projection images, back projection (reconstruction), feature enhancement, and forward projection. Each step manipulates pixel values as information is moved between 2D and 3D image spaces, culminating in the integration of clinically-important features into the *synthetic* mammogram. There are multiple different computer algorithms (blue boxes) that must be integrated to accomplish each step.

*Projection image correction* is the first post-acquisition processing step. Projection images contain 2D information generated by the series of projection views taken at oblique angles relative to the target. The goal of *projection image correction* is to assign gray-scale values to pixels in the projection image that reflect the actual attenuation of the object as well as correct for non-uniformities in the x-ray exposure and detector. The only information available to the system to determine attenuation is the number of x-ray photons measured by the detector pixel when it is active. This x-ray flux at the detector is referred to as the Intensity or Signal. Beer's law defines the mathematical relationship between intensity and attenuation [Duncan 2014]. It relates attenuation to the negative natural log of the ratio of the x-ray intensity reaching the detector to the incident x-ray intensity. This ratio is determined at the time of the examination by comparing the pixel intensity values in projections taken with the target in-place ($Signal_{raw}$) to pixel values obtained using an equivalent exposure but no target ($Signal_{blank}$). The first computational step is therefore to calculate the ratio of raw to blank pixel values. Additionally, by subtracting averaged pixel values from multiple dark images obtained without fired x-rays ($Signal_{dark}$), the final assigned pixel value, referred to as "normalized" ($Signal_{normalized}$), is corrected for detector non-uniformities, such as non-functioning pixels (Eq. 2.1).

$$Signal_{normalized} = (Signal_{raw} - Signal_{dark}) / (Signal_{blank} - Signal_{dark}) \quad (2.1)$$

In addition to normalizing the pixel values in the projection images, processing to address scatter, noise, and artifact is most efficiently applied at the level of the projection view and thus is often included in the step of projection view correction.

*Reconstruction* refers to the processing step of generating a 3D image from the information (normalized pixel intensity values) available in the series of corrected 2D projection images [Sechopoulos 2013b]. The goal of *reconstruction* is to assign grayscale values to the discretized image space that reflect the actual attenuation in the same region of the target. However, in this case, it is a 3D image space, and since it has volume, the discretized region of space is referred to as a voxel. There are many different reconstruction algorithms. However, in general, these can be considered in two broad groups: direct backprojection and iterative reconstruction, the latter including both algebraic and statistical approaches [Sechopoulos 2013b, Xu 2015]. Choosing a reconstruction approach involves compromise, balancing the complexity of the algorithm and its computational expense against the utility of the information presented to the reader. For example, direct backprojection for DBT can be accomplished within seconds using an off-the-shelf computer, while the more-complicated algebraic and statistical iterative approaches may require much longer, even on a dedicated computer that has parallel, multi-processing capability, depending on the complexity of the models used to represent the system mathematically. The complexity of the reconstruction algorithm is largely determined by the sizes of the projection data and the reconstructed image space as well as the system matrix model. The system matrix defines the relationship between the voxels in the reconstructed image space and the pixels in each projection image based on the geometry of the imaging system. Therefore, it can be used to back-project the 2D images into a 3D image space as well as forward-project the 3D image into the 2D image space. More detailed models of the system can better represent x-ray behavior (path estimates and noise models) and yield more accurate images, but applying these models is computationally expensive. Additionally, since it is impossible to generate a perfectly accurate 3D image space without complete sampling (see 2.5.3

Limited sampling introduces artifact), filtering is typically used to limit artifacts and improve image quality. However, filters always involve trade-offs in how they affect contrast, resolution, noise, and artifact, and therefore, filter selection and optimization is task-dependent. The work detailed in this dissertation, which sought to optimize task-specific image processing for this novel technology, explored different reconstruction approaches, including direct filtered backprojection [Kuo 2011] as well as an iterative algorithm [Wu 2015] (see 3.5.3d Reconstructing 3D images from 2D projections).

Regardless of the approach, the result of *reconstruction* is a stack of image slices, which step through the target in thin increments. For sDBT, the image slices were typically reconstructed in thin increments of 0.5 or 1 mm in order to maximize the clarity of small features, such as microcalcifications. Each slice brings into focus only those features present at the same anatomic depth, and the reader scrolls through the stack to identify pathology and appreciate how an image feature changes through depth. As such, it overcomes the primary limitation of 2D imaging, namely the superposition of image features, which can both obscure important findings and mimic pathology (see 2.2 Breast cancer and currently-available breast imaging technologies).

However, as noted above, it has now become standard to include the option of generating *synthetic* 2D slab images or a complete *synthetic* mammogram when displaying DBT information. *Synthetic* mammography integrates the information in the 3D image stack into a single 2D image using *forward projection* algorithms. It is at the step of *forward projection* that *feature enhancement* algorithms can be applied most efficiently. As is the case with reconstruction, there are a host of *forward projection* and feature-enhancement approaches, spanning a wide range of computational complexity from direct algebraic calculation to deep

learning [Homann 2015, Wei 2019, Rodriguez-Ruiz 2018]. A goal of this project has been to develop a complete image processing chain for sDBT that culminates in a clinically-useful *synthetic* mammogram (see 3.5.3e Forward projecting the 3D image space into *synthetic* 2D mammograms and 4.4 Incorporating *synthetic* mammography into sDBT).

## 2.7 Summary for Chapter 2: Literature Review

Made possible by advances in both technology as well as computer-based processing, 3D imaging has revolutionized medicine. To date, x-ray devices remain the predominant tools for medical imaging, although interestingly, until quite recently, the process of generating x-rays for medical imaging devices has changed little over the past century. Developed in the Applied Nanotechnology Laboratory at the University of North Carolina, CNT cathode technology now offers a viable approach to generate x-rays for human imaging. This novel approach allows the source cathode to operate at room temperature and uses simple voltage manipulation to control x-ray production. As a result, multiple distributed and fixed x-ray sources can be aligned in arrays and their x-ray production coordinated, thereby offering a flexible design capable of collecting many projection views quickly. This technology is ideal for the repetitive imaging steps required to perform 3D imaging. Recognizing the potential of the CNT-based x-ray source to improve 3D imaging, the decision was made to apply it to tomosynthesis, a form of limited-angle tomography. The work summarized in this dissertation explored the clinical potential of sDBT. In large part, it involved developing the computer algorithms to generate sDBT images containing information of high clinical value, potentially providing a tool to improve the detection of breast cancer.

# CHAPTER 3: METHODOLOGY

## 3.1 Introduction to Chapter 3: Methodology

Chapter 3: Methodology details the research protocols used to collect the data presented in this dissertation, providing the basis upon which the value and accuracy of the findings and eventual conclusions can be judged. Since this work sits at the intersection of basic experimentation and clinical application, it included a broad spectrum of study designs and research settings, ranging from highly-controlled laboratory conditions to studies involving human subjects and readers. The chapter begins by reviewing the rationale for the research approach, which in general involved testing the functionality of the novel *stationary* digital breast tomosynthesis (sDBT) technology in the lab in order to improve its performance in the clinic. The research environment is then described, followed by detailed descriptions of the data sources, collection methods, and methods of analysis used to generate and interpret the data. Finally, the chapter concludes with a discussion of the trustworthiness of the data in light of the limitations inherent with the study designs.

## 3.2 Rationale for the research approach

Given its purpose of exploring the clinical potential of a novel imaging system, the research presented in this dissertation often followed a predictable approach, in which basic experiments were designed to isolate and study a problematic issue or new application in order to improve the performance of the technology in the clinic. Most often, performance was measured in terms of the quality and/or diagnostic value of the generated images. Although customized to this unique technology, the study designs used in this dissertation were based on well-established

protocols for (1) measuring the performance of the sDBT device as it acquired images [EUREF 2018] as well as (2) the utility of the information presented in the resulting images [Gilbert 2015]. Typically, the goal of testing was to develop task-specific image processing algorithms, building on a foundation of code previously written by our research group [Wu 2015]. In other words, the development and then application of new code was typically the link that tied the findings from basic experimentation to the assessments of clinical utility through human study. Interestingly, findings during human study often demonstrated unanticipated concerns that needed to be addressed through coding, leading to the design of additional basic experiments. As such, research in the lab and experience in the clinic provided complementary data sources that have guided this dissertation work.

### 3.3 Research setting and context

The research detailed in this dissertation spanned the spectrum from basic experimentation in the lab to human study in the clinic. As such, its success reflects the highly-collaborative environment of the medical imaging research community at the University of North Carolina (UNC) at Chapel Hill and its School of Medicine. The work was guided by a team of scientists and translational radiologists interacting through the Applied Nanotechnology Laboratory, housed in the Department of Physics, with strong ties to the Joint UNC/NC State Department of Biomedical Engineering, the Biomedical Research Imaging Center (BRIC), and the Breast Imaging Clinic in the Lineberger Cancer Center at the North Carolina Cancer Hospital. This multi-disciplinary setting provided a vast resource base offering (1) intellectual expertise in x-ray device construction and operation, nanotechnology, image processing, statistical analysis, and the clinical assessment of image value, (2) the advanced equipment needed to build and test carbon nanotube (CNT)-enabled imaging devices at the pre-clinical

level, and (3) the tremendous support needed to carry out human studies involving experimental technologies. This support included study coordinators, technicians specially-trained to operate the unique imaging devices, radiation safety experts, and clinician-scientists to design the trials and oversee their safe implementation.

The work presented in this dissertation is best viewed in the context of the rapidly-advancing technology of 3D medical imaging in general. The sheer number of computed tomography (CT) scans ordered in the United States is a testament to the critical role that 3D imaging plays in modern medicine, given its ability to identify pathology early and accurately. Based on estimates made by Consumer Reports, more than 80 million CT scans were performed in 2015 [Consumer Reports 2015]. However, given the extraordinarily complex machinery required to accomplish CT, the CT scanner is expensive to build, purchase, and maintain, and as a result, CT scanning is costly. In 2019, it is estimated that the annual service cost for a CT scanner ranges from $35,000 - $100,000 [Kinnas 2019]. Additionally, even though the newest CT scanners and imaging protocols offer lower dose options for some tasks, most CT studies are associated with relatively high radiation doses, ranging from 16 mSv for a coronary CT angiogram to 1.4 mSv for a “low-dose” chest scan to screen for lung nodules [McCollough 2015, Larke 2011]. To put this dose in perspective, Americans are exposed to approximately 3 mSv of environmental radiation annually [Hendrick 2010]. In fact, it is now estimated that medical imaging accounts for the predominant source of radiation exposure in Americans [Jones 2012]. Although quantifying the risk of this exposure and its potential contribution to cancer is controversial, minimizing medical radiation exposure as much as possible is recognized as an important public health step [Hendrick 2010].

Tomosynthesis provides an opportunity to gather some 3D information at a lower cost and lower radiation dose. Although there are many possible applications for digital tomosynthesis, at this time, digital breast tomosynthesis (DBT) with its clinical designation of 3D mammography predominates, with a rapidly growing use over the past 9 years. By 2016, about 80% of breast imaging practices used 3D mammography [Gao 2017]. However, despite its potential, 3D mammography has yet to completely replace standard 2D mammography as the breast screening tool-of-choice. Additionally, its value as a diagnostic tool relative to other imaging modalities, such as ultrasound (US) and magnetic resonance (MR), remains controversial [Berg 2016]. As such, improving DBT technologies as well as the computer-processing approaches that generate the images for reader interpretation are areas of very active research by both academic groups and industry. This body of experience has yielded accepted pre-clinical models and human study protocols to assess DBT performance. For example, well-characterized breast-mimicking phantoms are available for pre-clinical testing (see 3.4.1 Breast-mimicking phantoms), and appropriate questionnaires and statistical analysis techniques have been developed to quantify reader performance and preference when viewing DBT images (see 3.6.2 Assessing reader performance and preference). The methodologies used in this dissertation work were based on these established experimental approaches.

## 3.4 Research samples and data sources

### *3.4.1 Breast-mimicking phantoms*

Breast phantoms that mimic the radiographic properties of human tissue have been developed, providing an imaging target for which ground truth knowledge of the features is available. As such, phantoms provide an ideal target for (1) optimizing image acquisition protocols, (2) testing different post-acquisition image processing steps, and (3) comparing one

imaging system to another. Breast-mimicking phantoms containing a wide variety of pathologies, such as masses and calcifications of different sizes, are available across a range of clinically-appropriate thicknesses and densities. Three phantoms were imaged during these experiments, including the American College of Radiology mammography accreditation phantom (ACR phantom), the CIRS Model 020 BR3D Breast Imaging Phantom (CIRS Imaging phantom) [CIRS Tissue Simulation & Phantom Technology, Norfolk, VA], and the CIRS Model 013 Stereotactic Needle Biopsy Training Phantom (CIRS Biopsy phantom) [CIRS Tissue Simulation & Phantom Technology, Norfolk, VA]. The ACR phantom replicates the clinical characteristics of a 4.5 cm compressed breast thickness containing feature mimics in a smooth background reproducing an average glandular and adipose tissue density (Figure 3.1A). The microcalcification and mass features were utilized in this work. Five clusters of aluminum oxide specks mimic microcalcifications, with specks ranging in size from 0.16 mm to 0.54 mm. Five lens-shaped mimics reproduce mass lesions of varied size and density. The semi-circular CIRS Imaging phantom replicates a compressed breast shape (Figure 3.1B). The CIRS Imaging phantom simulated a breast environment with 50% fatty and 50 % glandular tissue in a swirled pattern [CIRS 2020a], most closely resembling a Breast Imaging Reporting and Data System (BIRADS) class C density. It was available in 1-cm slabs, which could be stacked to simulate compressed breasts of different thicknesses. One slab also contained circular mass and microcalcification mimics, ranging in size and density. For the experiments with sDBT, three, four, and five cm thick stacks were usually studied, as this is the typical range for compressed human breast thicknesses during mammography. The CIRS Imaging phantom recreates the clinical situation in which background tissues at different depths obscure features-of-concern when the 3D breast anatomy is collapsed into a 2D image. The CIRS Biopsy phantom

reproduces a 4.5 cm-thick compressed breast that contains dense masses and microcalcification mimics embedded in gel with a consistency and shape similar to breast tissue [CIRS 2020b] (Figure 3.1C).


Figure 3. 1. Photographs of the three breast-mimicking phantoms used in this dissertation work. Each phantom, including the American College of Radiology mammography accreditation phantom (A), the CIRS Model 020 BR3D Breast Imaging Phantom (B), and the CIRS Model 013 Stereotactic Needle Biopsy Training Phantom (C), contained unique combinations of pathology and background.

For some experiments, the phantoms were customized. For example, in order to simulate contrast-enhanced 3D breast imaging, a 1-cm thick acrylic plate was inserted between background slabs of the CIRS Imaging phantom at different depths [Puett 2018b]. The customized acrylic plate contained drilled wells into which iodinated solutions were added. The 2.5 mm deep wells had diameters of 0.5, 1.0, 1.5, and 2.0 cm and held iodinated contrast (iohexol) diluted with water to concentrations of 0, 1.0, 2.5, 5.0, 10, and 15 mg/ml, simulating the tissue concentrations achievable during human contrasted mammography. Contrast concentrations in imaging studies are often reported as area densities to allow correlation with signal intensities over a defined region in the image. The area densities used in these experiments ranged from 0 to 3.75 mg/cm$^2$, reproducing those noted in clinical trials of contrast-enhanced mammography [Jong 2003]. For another set of experiments, in order to determine how well the processing algorithms could isolate pathology by reducing the obscuring effects of overlapping tissues present at other depths, the CIRS Biopsy phantom was stacked above a single background

slab of the CIRS Imaging phantom. This artificial combination created the situation in which the mass features were separated in depth from the swirled background features.

### *3.4.2 Lumpectomy specimens*

Although breast-mimicking phantoms provide a standardized target, imaging resected breast specimens offers a good opportunity to assess the clinical value of the information displayed in images, since pathology is available to provide diagnostic and ground truth information. This work included a comparison of images of lumpectomy specimens collected by sDBT and standard breast imaging techniques [Tucker 2014a, Puett 2019a]. Twenty-three women with Breast Imaging and Reporting Data System (BIRADS) 4 or 5 lesions ("suspicious abnormality" or "highly suspicious for malignancy") were recruited following study approval by the University of North Carolina at Chapel Hill Institutional Review Board (IRB). The concerning breast lesions had been discovered and evaluated by standard screening and diagnostic imaging, and the patients were awaiting lumpectomy following a needle localization procedure. Following removal, the specimens were handled according to the standard North Carolina Cancer Hospital protocol, which included gently compressing them in a customized container over a perforated grid prior to magnified (1.8x) 2D digital mammography in order to define lesion margins (Figure 3.2). The grid is identified by a number-letter combination, providing a background in the x-ray image to localize the identified pathology. Following this standard imaging step, the contained specimens were also imaged by sDBT and conventional moving-source DBT, after which they were transferred to the Department of Pathology.

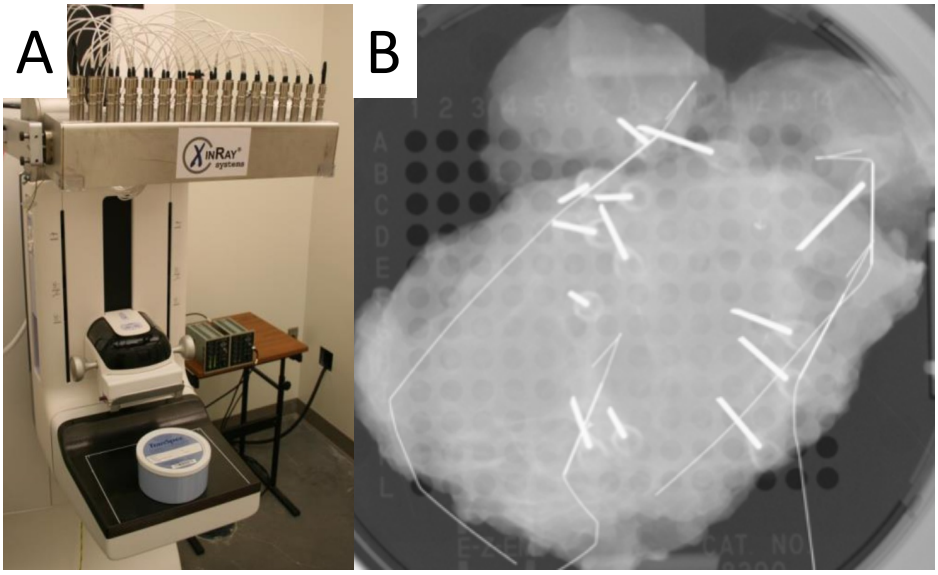


Figure 3. 2. Photograph of the *stationary* digital breast tomosynthesis (sDBT) system used to image lumpectomy specimens along with an example projection image. The lumpectomy specimens were transported and imaged in standard specimen containers (A), the floor of which contained a grid of identified holes to localize pathology. The radiographic appearance of the lumpectomy specimen in the container can be appreciated in this central projection image acquired by sDBT (B). The information in the projection image is used to reconstruct the 3D image stack. Note the absence of metal artifact at the projection level, compared to the prominent artifact present in the reconstructed image slice of a similar specimen (Figure 2.8). Figure adapted from [Tucker 2014a] and [Puett 2019a].

### *3.4.3 Patient selection for human study*

Although imaging resected breast specimens provides experience with human tissue, testing the clinical utility of an imaging device requires assessing its performance through human study. An IRB-approved and HIPAA-compliant prospective study (ClinicalTrials.gov NCT01773850) provided the initial quantitative assessment of sDBT performance at the clinical level, comparing sDBT to standard 2D mammography [Lee 2019]. This study recruited 55 women between May 2014 and February 2016 to get standard two-view [craniocaudal (CC) and mediolateral oblique (MLO)] imaging by sDBT following the discovery of a "suspicious abnormality" (BIRADS 4) by standard screening digital mammography at our Breast Imaging Clinic. Of this group, 4 underwent biopsy before the sDBT was obtained and were excluded. The

sDBT images were unavailable in another 8 because of an issue coordinating the detector and source array. Therefore, images from 43 women were available for analysis. The average age of the participants completing the study was 56.7 +/- 12.7 years (35 to 83), of whom 64% were considered to have dense breast tissue (BIRADS density categories C or D) [Lee 2019]. Of the 43 subjects included in the final analysis, 12 cases of malignancy (28% of the study population) were identified by pathology on specimens obtained by ultrasound-guided core needle biopsy, stereotactic biopsy, or a surgical excision following needle localization. The final pathologic diagnoses included six infiltrating ductal carcinomas, five intraductal carcinomas, and one invasive lobular carcinoma.

#### *3.4.4 Reader selection*

There are objective measures of image quality, such as the detectability index, which integrate measures of contrast, resolution, and noise into a composite value. These tools are useful for quantifying task-specific and regional image information and were used extensively in this dissertation work to develop and test image processing algorithms. However, image quality at the clinical level is best determined by the visibility of diagnostically-important features in the images presented to readers. As such, understanding the clinical potential of a new imaging technology requires studies that assess reader performance (diagnostic accuracy) and preference when interpreting images generated by the experimental technology relative to the accepted standard. As such, readers, like patients, needed to be recruited for participation in some of the studies included in this dissertation [Lee 2019, Puett 2019a]. Previous work has shown that reader experience is important, demonstrating differences in the performance of readers with and without at least 10 years of breast reading experience [Wallis 2012]. As such, readers with fellowship training in breast imaging and who had at least a decade of experience with

mammography were recruited. Among this group, there was a broad range of experience with DBT, ranging from no experience to 5 years, allowing some appreciation of the effect of DBT training and experience on reader performance [Lee 2019].

## 3.5 Data collection methods

### *3.5.1 Acquiring images*

*3.5.1a Differences in the breast imaging systems*

During the course of this dissertation work, images were acquired with several different breast imaging modalities, including 2D full-field digital mammography and conventional, moving source DBT. These systems provided commercially-available and state-of-the-art references against which sDBT was compared. When imaging patients and patient samples (lumpectomy specimens) at the North Carolina Cancer Hospital, standard screening 2D mammograms and magnified 2D mammograms were obtained by a Senographe Essential (General Electric, GE Healthcare, Milwaukee, WI, USA) device that used Mo and Rh anode and filter combinations under the control of a proprietary automatic optimization of parameters (AOP) mode to deliver x-ray beams from nominal focal spots measuring 0.3 IEC for patient screening and 0.1 IEC for magnified imaging. The mammograms were processed through Premium View (GE Healthcare, Milwaukee, WI USA). Some phantom-based experimentation was also carried out at the Duke University Medical Center, with imaging under the supervision of a medical physicist. 2D imaging in the Duke system utilized a commercially-available Selenia Dimensions 2D and 3D mammography system (Hologic, Inc., Marlborough, MA, USA). Conventional, or moving-source, DBT images were also collected using the Selenia Dimensions 2D and 3D mammography system, since this system provided the framework upon which the CNT-enabled sDBT system was constructed (see 3.5.1b Operating the sDBT system for clinical

imaging). The Selenia Dimensions system was operated using the Auto-Filter setting and run in the Combo HD mode, which automatically selected the dose and anode/filter combination. Additionally, when operated in the Combo HD mode, the Selenia Dimensions system generated a standard "processed" 2D mammogram as well as a *synthetic* mammogram termed C-View (software version 2.1.1.1) (see 2.6 The image processing chain that generates sDBT images and the value of the synthetic mammogram). This software version produced the C-View image using a proprietary forward projection of the reconstructed 3D image space, which itself was generated by a filtered back-projection approach [Smith 2016] (see 3.5.3d Reconstructing 3D images from 2D projections and 3.5.3e Forward projecting the 3D image space into *synthetic* 2D mammograms). In contrast, the sDBT system used a fixed anode/filter combination, with the exposure being manually selected to match the total entrance dose suggested for a conventional DBT scan of the same object, and reconstruction was accomplished using a customized algebraic iterative technique [Wu 2015, Puett 2020a] (see 3.5.3d Reconstructing 3D images from 2D projections).

Since commercially-available 2D and 3D mammography systems provided references against which sDBT was compared, it was important to recognize differences in their technological specifications in order to interpret the results of experiments designed to compare their performance. The resolution of an imaging system is related to its geometry, more specifically, the sizes and relative locations of the anode focal spot of the x-ray source and the detector pixel (see 2.4.2 Contrast and resolution). Some conventional DBT devices, including the parent DBT device from which the sDBT systems were built, move the source without interruption to collect the series of projection views (see 2.2.4 The clinical value and technical limitations of conventional 3D mammography). These continuous-motion systems have an

asymmetric focal spot that is elongated in the travel direction of the source due to motion blur. The actual size depends on the travel speed and dose rate, which determines how long the x-ray "on-time" must be to deliver the required dose. Since the sDBT sources are fixed, their focal spots are isotropic and have been measured to be 0.9 mm at the full-width-at-half-maximum (FWHM) [Tucker 2014b], with the potential to reach 0.6 mm FWHM, if electronic focusing of the CNT cathode-generated electron beam is employed [Qian 2012]. However, in order to achieve an adequate dose rate to maintain an acceptably-short study duration given the heating constraints with a stationary anode, electronic focusing was not used in the experiments reported in this dissertation work. The sDBT detectors remained original to the DBT system. They used a direct conversion amorphous-Selenium (a-Se) photoconductor system, which could be operated in a binned mode with a pixel size of 140 μm or a 70 μm "full-resolution" mode.

As an example of the differences in the performance characteristics of some of the imaging devices used in these experiments, Table 3.1 compares the key operating parameters for the commercial 2D and 3D systems and sDBT when imaging breast-mimicking phantoms [Puett 2019a, Puett 2020a], identifying their differences in geometry, focal spot size, beam filtration, and detector pixel size, since these parameters have direct impact on the quality of the images they produce.

| | Phantom Imaging | | | Specimen Imaging | |
|---|---|---|---|---|---|
| **Parameter** | **FFDM** | **DBT** | **sDBT** | **DBT** | **sDBT** |
| Static Focal Spot Size [SD/NSD] (mm) | 0.43/0.52 | 0.46/0.53 | 0.9/0.9 (FWHM) | 0.46/0.53 | 0.9/0.9 (FWHM) |
| Focal Spot Motion [SD] (mm) | - | 0.99* | - | 1.65* | - |
| Anode Material | W | W | W | W | W |
| Filter Material (Thickness in mm) | Rh (0.05) | Al (0.7) | Al (1) | Al (0.7) | Al (1) |
| Angular Span (degrees) | - | 15 | 28 | 15 | 28 |
| Number of projection views | 1 | 15 | 15 | 15 | 15 |
| Source-to-Image Distance (mm) | 700 | 700 | 700 | 700 | 700 |
| Detector Pixel Size (μm) | 70 | 140 | 70 | 140 | 70/140** |
| Reconstructed Voxel Size (μm) | - | 100 | 70 | 39*** | 39*** |
| Peak Energy (kV) | 28 | 30 | 35 | 26 | 26 |

Table 3. 1. A comparison of the operating parameters of full field digital mammography, conventional digital breast tomosynthesis (DBT), and stationary digital breast tomosynthesis (sDBT), identifying similarities and differences that have a direct impact on the image quality measurements used in this dissertation work. The operating parameters are displayed for both phantom imaging [Puett 2020a] as well as lumpectomy specimen imaging [Puett 2019a]. *Focal spot motion was calculated using the approach described in [Marshall 2012]. The extent of this motion depended on the x-ray exposure time per projection. Of note, reflecting the differences in their shapes, the focal spot was modeled as a rectangle for the moving-source DBT system and as a Gaussian for sDBT, with the reported value being the full width at half maximum (FWHM). **By default, sDBT uses the detector in "full resolution" mode, employing a detector pixel size of 70 μm. However, for specimen imaging, the projection images were also binned to 140 μm in post-processing to match the detector pixel size of the conventional DBT system [Puett 2019a]. ***Microcalcification sizes in specimen images collected by conventional DBT and sDBT were compared to magnified (1.8x) mammography, and therefore the reconstructed voxels for tomosynthesis imaging were generated at 1.8x magnification of the "full resolution" detector. SD = scan direction, NSD = non-scan direction, FWHM = full-width-at-half-maximum.

Measurements of resolution and noise were used to quantify differences in the performance of the standard 2D FFDM, conventional moving-source DBT, and carbon nanotube-enabled sDBT devices. To provide the most direct comparison, resolution and noise were measured in "raw" images (see 2.6 The image processing chain that generates sDBT images and the value of the *synthetic* mammogram), including the raw FFDM image and the raw central projection images of conventional DBT and sDBT when the x-ray source was located

directly above the detector (0° projection angle). Resolution was quantified as the modulation transfer function (MTF). The MTF was calculated from the changing signal intensity off of a thin tungsten edge positioned ~ 6 cm from the edge of the detector and 4.5 cm above the detector table. The metal edge was placed at a slight angle relative to the detector pixel matrix. Noise was quantified as the radial average of the 2D normalized noise power spectrum (NNPS) by measuring the NPS in half-overlapping areas measuring 128x128-pixels when a 4.5-cm-thick polymethylmethacrylate (PMMA) slab was imaged. A second-order polynomial was used for detrending, and the measurements were normalized by the mean signal over a large area of the image.

The MTF and NNPS measured in the raw FFDM image and central projection images acquired by DBT and sDBT are displayed in Figure 3.3. Note the similar MTF curves for sDBT and DBT, as measured at a height of 4.5 cm above the detector table and using each system's default operational settings. As expected given its smaller focal spot size (Table 3.1), FFDM produced a raw image with a higher resolution compared to the raw projection images of DBT and sDBT (Figure 3.3A). Also, noise was higher in the projection images acquired by DBT and sDBT compared to FFDM (Figure 3.3B). Again, this finding was expected, since only a fraction of the total study dose is delivered during the acquistion of each projection image during tomosynthesis. These differences in resolution and noise can be anticipated to influence image characteristics and feature display in the FFDM, conventional DBT, and sDBT images.

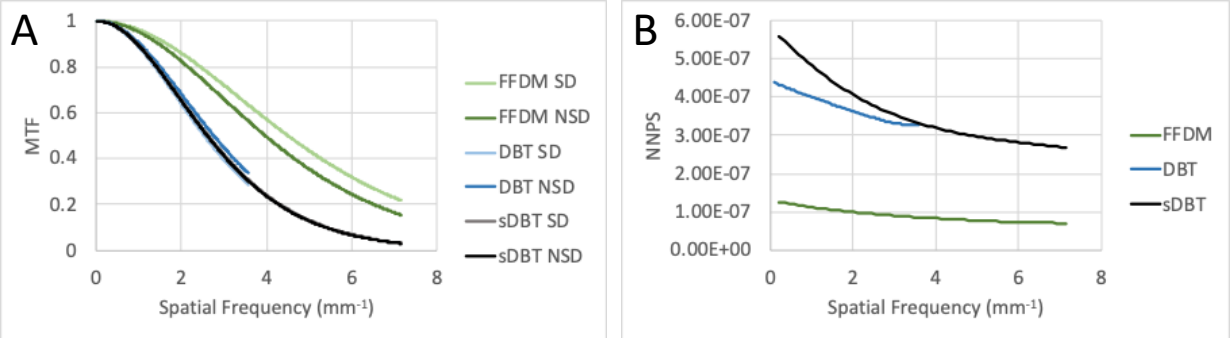


Figure 3. 3. Graphic display of resolution and noise in the three different breast imaging modalities compared in this dissertation work, including standard mammography, conventional digital breast tomosynthesis, and *stationary* digital breast tomosynthesis (sDBT). Resolution was measured as the modulation transfer function (MTF) in the raw 2D full field digital mammography (FFDM) image and raw central projection images from conventional digital breast tomosynthesis (DBT) and carbon nanotube-enabled sDBT at a height of 4.5 cm above the detector table and using each system's default operational settings. MTF was measured in both the scan direction (SD) and non-scan direction (NSD). The 1D normalized noise power spectrum (NNPS) was calculated as the radial average of the 2D NNPS. Figure adapted from [Puett et al. 2020a].

*3.5.1b Operating the sDBT system for clinical imaging*

The first-generation sDBT device was used for patient imaging. It was constructed from a Selenia Dimensions DBT system (Hologic, Inc., Marlborough, MA, USA) by replacing the single, moving thermionic x-ray source with an array of 31 fixed CNT-enabled sources (Figure 3.2A) [Tucker 2013]. Much of the remainder of Hologic system was unchanged, including the gantry that rotated the source array between the standard craniocaudal (CC) and mediolateral oblique (MLO) view orientations, the breast compression plates, and the detector. An electronic control system (ECS) operated the individual sources and coordinated source firing with detector activity. During a DBT study, the total radiation dose delivered to the target is divided among the multiple projections. Each projection image is therefore collected at a relatively low dose, and as a result, testing is needed to optimize the number and distribution of the projection views to maximize the image quality at each view. Pre-clinical testing of this sDBT system demonstrated an optimized configuration of 15 sources fired with equal doses across an angle-span of 28°

[Tucker 2013]. Ensuring a safe operation during human study was critical, with doses determined by the thickness of the compressed breast. Over the course of human testing, the sDBT system used exposures up to 90 mAs over a range of 29 to 39 kVp, based on breast thickness, with 1 mm Al filtration. These exposures were set to match those of the Hologic DBT system from which the sDBT device was constructed, and a radiation safety inspection assured dose compliance with the Mammography Quality Standards Act (MQSA) when the sDBT device began clinical testing in 2014. To ensure a stable source performance over time, dose information was again collected on the sDBT system in 2018 [Lee 2019]. The surface entrance dose was measured directly as the incident air kerma (mGy) using a Radcal Accu-Pro (9096) dosimeter and 10x6-6M mammography ion chamber (Radcal, Monrovia, CA USA) positioned at different heights above the detector. The surface entrance dose was measured as a function of the compressed breast thickness. This testing demonstrated that the sDBT system delivered entrance doses comparable to standard mammography (Figure 3.4) [Lee 2019].

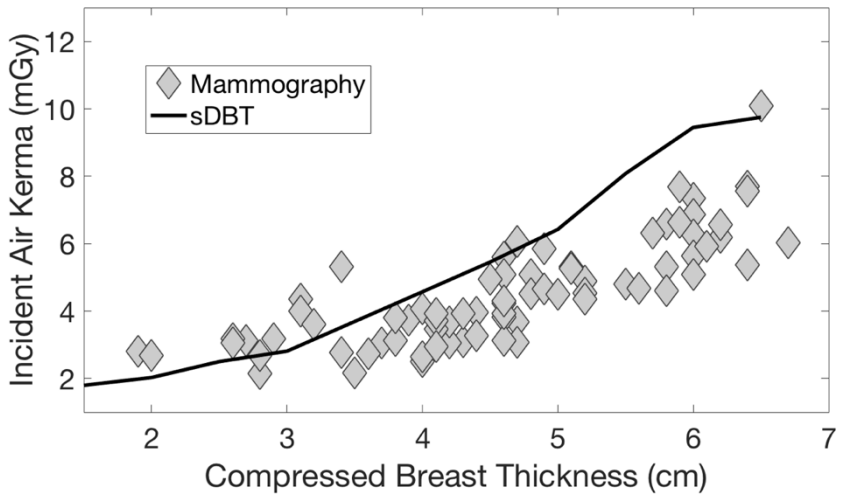


Figure 3. 4. Graphic display comparing doses of standard mammography and *stationary* digital breast tomosynthesis (sDBT) during human study. The entrance dose was measured as a function of breast thickness for the Senographe Essential mammography system (grey diamonds) and sDBT (black line). Doses are reported as the incident air kerma in mGy and were measured using

a mammography ion chamber dosimeter for sDBT. For each mammogram, doses were obtained from the DICOM header. Figure adapted from [Lee 2019].

Obtaining a full patient study in as short a time as possible is important, as breast compression can be uncomfortable and patient motion will blur the image. When operated without electronic focusing, CC and MLO imaging by sDBT could be accomplished in less than 5 seconds [Lee 2019].

*3.5.1c Configuring the sDBT system for contrast-enhanced imaging*

To date, most clinical experience with 3D contrast-enhanced (CE) breast imaging has been with gadolinium-enhanced MR [Argus 2010]. However, given the high cost and limited availability of MR compared with radiation-based imaging, research continues into the development of CE-DBT. For radiation-based techniques, such as DBT, iodine is the contrast agent of choice. However, CE mammography has shown only a minimal lesion enhancement above background (BKG) following standard intravenous iodine dosing and has demonstrated that the differences distinguishing benign from malignant enhancement patterns in breast lesions are subtle [Jong 2003]. As a result, two imaging steps with subtraction are needed for CE mammography and CE-DBT. Subtraction removes the BKG signal and thereby improves contrast in the enhanced tissue. These experiments with sDBT simulated both temporal subtraction (TS) and dual-energy subtraction (DES) protocols. TS involves imaging before and after the administration of contrast using a photon energy above the characteristic absorption (K-edge) for iodine, whereas DES compares images collected with photon energies above and below the K-edge [Hill 2016]. Although this critical subtraction step during CE imaging has been studied with conventional, moving-source DBT previously [Ikejimba 2014, Chen 2013], this work was the first to incorporate scatter correction with a stationary system for CE-DBT imaging. Figure 3.5 displays representative images of TS and DES as they appear through the

image processing chain, allowing an appreciation of the differences in the two image acquisition protocols and the key subtraction step in both.

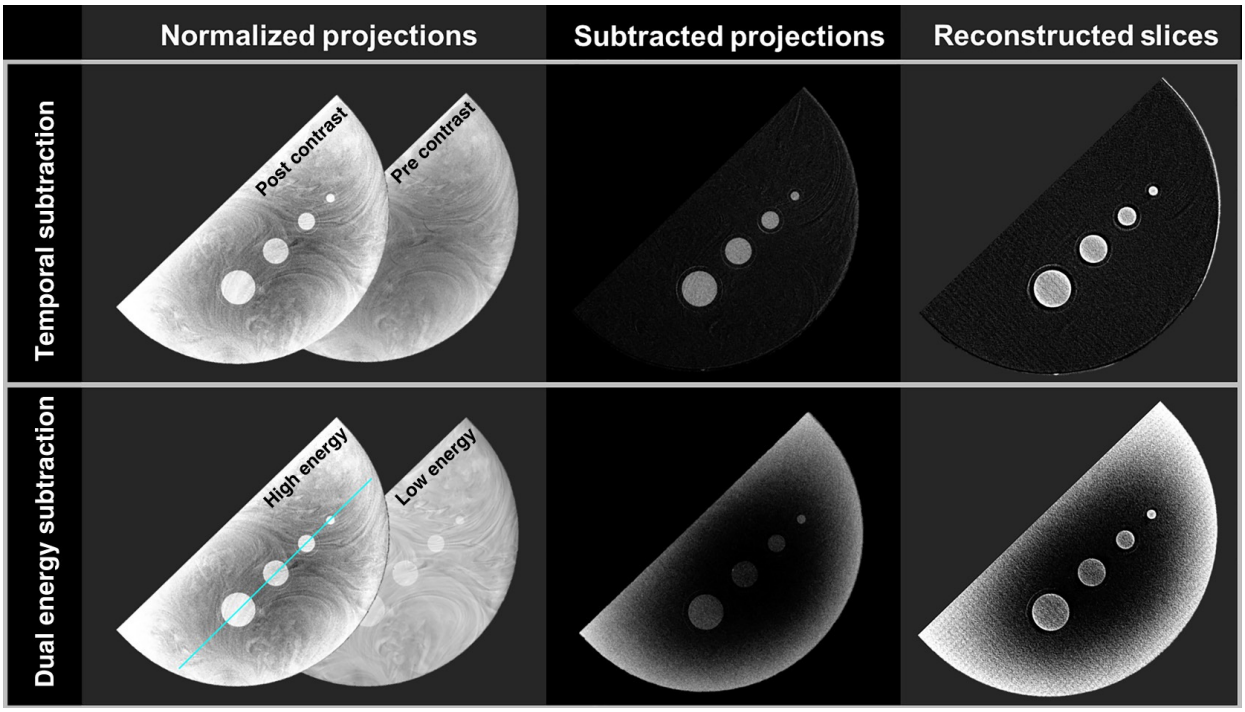


Figure 3. 5. Representative images through the post-acquisition processing steps during a study of contrast-enhanced stationary digital breast tomosynthesis (sDBT). Both temporal subtraction (TS) and dual energy subtraction (DES) protocols were used to collect projection views of a 5-cm thick phantom, customized with wells containing iodine at a concentration replicating those achieved during patient imaging. Note the "cupping" artifact, which refers to the intensity differences between the periphery and central regions of the image, present in the high energy normalized projections and persisting in processed DES images without scatter correction. The blue line through the high-energy DES normalized projection image identifies the path of the line profile analyzed in Figure 4.4. Figure adapted from [Puett 2018b].

In order to replicate tube settings used in the clinic, the sDBT source array delivered a total exposure of 88 mAs at 49 kVp for TS and high-energy (HE) DES imaging and 30 kVp to collect the low-energy (LE) DES images. A 0.25-mm copper filter was added to the standard 0.5 mm aluminum filter during HE imaging to remove photons with energies below the iodine K-edge (33.2 keV). The contrasted breast environment was simulated using customized breast-mimicking phantoms (see 3.4.1 Breast-mimicking phantoms).

### *3.5.2 Measuring scatter*

One of the goals of this work was to model scatter with the sDBT system in order to develop correction algorithms that could be applied during post-acquisition processing to improve image quality. This required measuring scatter across a range of breast thicknesses and attenuation features, with a specific concern over scatter during contrasted imaging, since scatter is most problematic off highly-attenuating features during x-ray imaging. In these studies, scatter was measured indirectly using a beam-pass primary sampling device (PSD) to isolate the primary component of the total signal [Inscoe 2013, Puett 2018b]. The protocol involved collecting a second series of projection images immediately after the initial scan with the PSD positioned on the compression plate between the phantom and x-ray source. The PSD was a 2-mm thick stainless-steel sheet with 2-mm diameter holes separated by a center-to-center distance of 10.6 mm, resulting in an average of 118 holes located over the phantom. The size and separation of the holes was determined mathematically to allow measurement of the non-deflected x-ray signal reaching the detector when the PSD was positioned just above the target. By comparing the total area of the PSD holes with the area of the breast phantom, it was determined that collecting the second series of projections with the PSD in place added an average of 3% of the radiation dose delivered during imaging without the PSD. Simple subtraction of the primary signal from the total signal, measured without the PSD in place, allowed calculation of the scatter signal. Although simple in concept, this measure was difficult in practice, requiring the development of software that could accurately locate the primary signals in the PSD image, measure their strength over a broad intensity range, and then use this information to develop a scatter map of the entire target (see 3.5.3b Creating scatter maps) [Puett 2018b].

### *3.5.3 Processing images*

*3.5.3a The image processing chain for sDBT in context*

In large part, the work in this dissertation involved experimentation to analyze problematic issues with CNT-enabled *stationary* tomosynthesis, such as scatter and artifact, and then use the findings to develop image processing approaches to minimize their effects on the final images displayed for interpretation. Although the focus of this work involved breast imaging, experimentation with sDBT was actually carried out alongside the pre-clinical development and early clinical application of *stationary* tomosynthesis across a wide range of imaging tasks being explored in the Applied Nanotechnology Laboratory. These included dental [Inscoe 2018, Puett 2020b], musculoskeletal [Inscoe 2020b], chest [Lee 2018, Gunnell 2019], and head [Spronk 2020, Luo 2020] imaging. The image processing approaches developed for sDBT were influenced by this broad experience, since each anatomic environment introduced unique challenges for processing (see 2.3.2 Carbon nanotube (CNT)-enabled x-ray source arrays and *stationary* digital tomosynthesis (sDT) and APPENDIX: Developing *synthetic* dental radiography)**.** For example, correcting for scatter is critically-important when the target environment contains features with widely-varying attenuation properties. In chest imaging, the low attenuation airspace regions are adjacent to the highly-attenuating bony thoracic cage and the soft tissues of the mediastinum and diaphragm. Similarly, in head imaging, the soft tissues of the brain are encased by the dense skull. In these environments, the scatter signal often predominates the primary signal in clinically-important regions-of-interest [Ullman 2004].

Artifact reduction provides another example of the unique challenges posed by different target environments. Reducing artifact around dense features in the breast is important, since shadowing and rippling artifact off large calcifications or the metal needles and wires used to

guide biopsy obscure information in the image. However, metal artifact reduction (MAR) techniques are essential for dental tomosynthesis, as dental pathology is often hidden in the artifact-laden image regions adjacent to metal. Examples include recurrent caries adjacent to restorations and sites of bone resorption at the bone-metal interface of dental implants. In short, the lessons learned from working with *stationary* tomosynthesis across a range of imaging tasks provided much of the background experience used to develop the sDBT algorithms.

An overarching goal of this work has been to develop a complete image processing chain for sDBT, culminating in the production of a clinically-useful *synthetic* mammogram (see 2.6 The image processing chain that generates sDBT images and the value of the *synthetic* mammogram). This goal would advance the evolution of sDBT toward a viable clinical device, providing a crucial step for the continued human study of this promising new technology. Given the significant clinical benefits of *synthetic* mammography, including the fact that it may prove to be the key advance by which DBT replaces standard mammography as the screening and diagnostic breast imaging tool of choice, improving the image processing steps needed to generate the *synthetic* mammogram is an area of very active research by both academic research groups and industry. The *synthetic* mammogram is the product of many computational steps, referred to collectively as an image processing chain, with each chain link or processing step accomplishing a specific task (Figure 3.6).

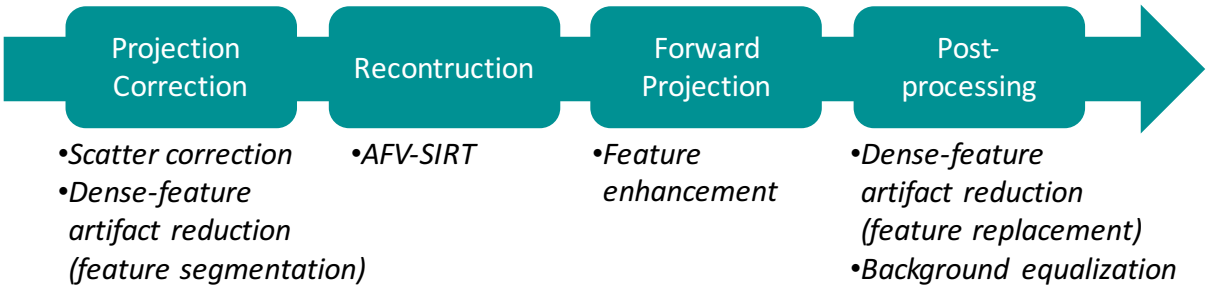


Figure 3. 6. Overview of an image processing chain applicable to *stationary* digital breast tomosynthesis (sDBT). The image processing chain moves information from the series of 2D projection views collected at the time of the study, through a "reconstructed" 3D image space, and finally back into a "synthesized" 2D image. For much of this dissertation work, reconstruction was accomplished by algebraic iteration, using a customized approach described as an adapted fan volume modification of the simultaneous iterative reconstruction technique (AFV-SIRT). Specific image processing options (italics) are listed below the step at which they are typically applied. Figure adapted from [Puett 2019b].

Each step in the image processing chain must be optimized. Optimization involves tradeoffs in the information that needs to be displayed in the image to accomplish the clinical task and the complexity of the algorithm, which determines its computational time and computer hardware requirements. In large part, processing time reflects the processing power of the hardware available for the task. For most of this dissertation work, processing was accomplished using an off-the-shelf laptop computer (four-core MacBook Pro with a 2.7 GHz Intel Core i5 processor). With this device, once a reconstructed image stack was available, forward projection (see 3.5.3e Forward projecting the 3D image space into *synthetic* 2D images) required about 40 seconds, while artifact reduction (see 3.5.3c Reducing artifact) added an additional 4 seconds and background equalization (see 3.5.3f. Equalizing background in the *synthetic* mammogram) around 30 seconds, although processing times varied based on the size of the breast. However, given the limited sampling that characterizes tomosynthesis, robust reconstruction approaches yield better results. Therefore, when testing the full image processing chain at the clinical level by reader study, an algebraic iterative approach developed specifically for the sDBT system was

used [Wu 2015] (see 3.5.3d Reconstructing 3D images from 2D projections). As a result of its detailed modeling of the system geometry, reconstructing the 3D image stack from the 15 projection images collected on a 5.5 cm-thick breast required 30 minutes using a dedicated computer for this specific task (3.5 GHz 6-core i7-5930K CPU).

*3.5.3b Creating scatter maps*

Correcting for scatter is the mathematical step of adjusting pixel values to remove the scatter component from the total signal. In these experiments, scatter was measured indirectly using beam-pass collimation to isolate the primary signal [Puett 2018b] (see 3.5.2 Measuring scatter). The projection images collected with the PSD contained circular regions of Signal against a low Signal BKG. In these experiments, Signal was defined simply as the average of the pixel intensity values within a defined region-of-interest (ROI) in the image. The PSD-collimated projection images were binarized by thresholding, and the circular regions were isolated based on their known size. These regions consisted of a central plateau of primary photons and a ring of penumbra. The central pixel was identified for each region, and the average signal within a 3-pixel radius around the central pixel was defined as $\text{Signal}_{\text{primary}}$. $\text{Signal}_{\text{scatter}}$ was calculated as the difference between $\text{Signal}_{\text{primary}}$ and $\text{Signal}_{\text{total}}$, which was the Signal in the same region of the corresponding projection image obtained without the PSD [Eq. (3.1)]:

$$\text{Signal}_{\text{scatter}} = \text{Signal}_{\text{total}} - \text{Signal}_{\text{primary}} \quad (3.1)$$

Interpolation was used to assign information regarding scatter to pixels located between these sampled regions. The result was a scatter "map" unique to each projection image. However, different algorithms have been proposed in the literature to generate the scatter map, based on

applying direct scatter values [Sechopoulos 2012, Lu 2015] or values incorporating the scatter-to-primary ratio (SPR) [Yang 2012]. This work compared three approaches for generating pixel-specific scatter maps, referred to as $ScatterMap_{direct}$, $ScatterMap_{SPR}$, and ScatterMap filtered-SPR ($ScatterMap_{fSPR}$) [Wu 2017]. Each approach differed in its application of information collected by beam-pass collimation (see 3.5.2 Measuring scatter).

$ScatterMap_{direct}$ was simply a biharmonic spline interpolation [Eq. (3.2)] of $Signal_{scatter}$ [Eq. (3.1)] determined at the PSD-sampled sites.

$$ScatterMap_{direct} = Interpolation(Signal_{scatter}) \quad (3.2)$$

Developing $ScatterMap_{SPR}$ was a three-step process. First, SPR was calculated at the PSD-sampled sites. Second, biharmonic spline interpolation assigned SPR values to pixels between the PSD-sampled sites [Eq. (3.3)]. The final step [Eq. (3.4)] calculated a pixel-specific scatter value from $SPR_{interp}$ to generate $ScatterMap_{SPR}$:

$$SPR_{interp} = Interpolation(SPR_{sampled}) \quad (3.3)$$

$$ScatterMap_{SPR} = Signal_{total} * (SPR_{interp} / (1 + SPR_{interp})) \quad (3.4)$$

The mathematical steps to develop $ScatterMap_{fSPR}$ can be considered a blend of the calculations used to generate the direct and SPR maps described above. First, an $SPR_{direct}$ value was calculated for every pixel using $ScatterMap_{direct}$ and $Signal_{total}$ [Eq. (3.5)].

$$SPR_{direct} = Scatter_{direct} / (Signal_{total} - Scatter_{direct}) \quad (3.5)$$

As such, $SPR_{direct}$ differed from $SPR_{interp}$ in terms of the information that was interpolated from the PSD-sampled sites to pixels between the sampled sites. Next, a scatter value was assigned to each pixel using a mathematical step similar to Eq. (3.4). However, developing $ScatterMap_{fSPR}$ included the application of a 2-D Gaussian filter (*f*) to $SPR_{direct}$ [Eq. (3.6)].

$$ScatterMap_{fSPR} = Signal_{total} * (fSPR_{direct} / (1 + fSPR_{direct})) \quad (3.6)$$

A scatter map refers to the collection of all pixel-specific scatter values. Correcting the normalized projection image signal ($Signal_{corrected}$) for scatter was accomplished by simple subtraction [Eq. (3.7)].

$$Signal_{corrected} = Signal_{total} - ScaterMap_{direct\ or\ SPR\ or\ fSPR} \quad (3.7)$$

*3.5.3c Reducing artifact*

Shadowing and rippling artifact off of highly-attenuating or dense features can be significant in tomosynthesis images (see 2.5.3 Limited sampling introduces artifact), including slices of the reconstructed 3D image stack and *synthetic* 2D images. These artifacts are not only distracting when images are viewed for interpretation, but they can also hide pathology. Hence, image processing to correct dense feature artifact is often needed during breast tomosynthesis imaging to minimize artifact associated with large calcifications as well as metal wires and clips, which may be placed to guide biopsy or be present from previous surgery.

The artifact reduction approach for sDBT was integrated into the image processing chain at the levels of the projection image and *synthetic* mammogram (Figure 3.7).

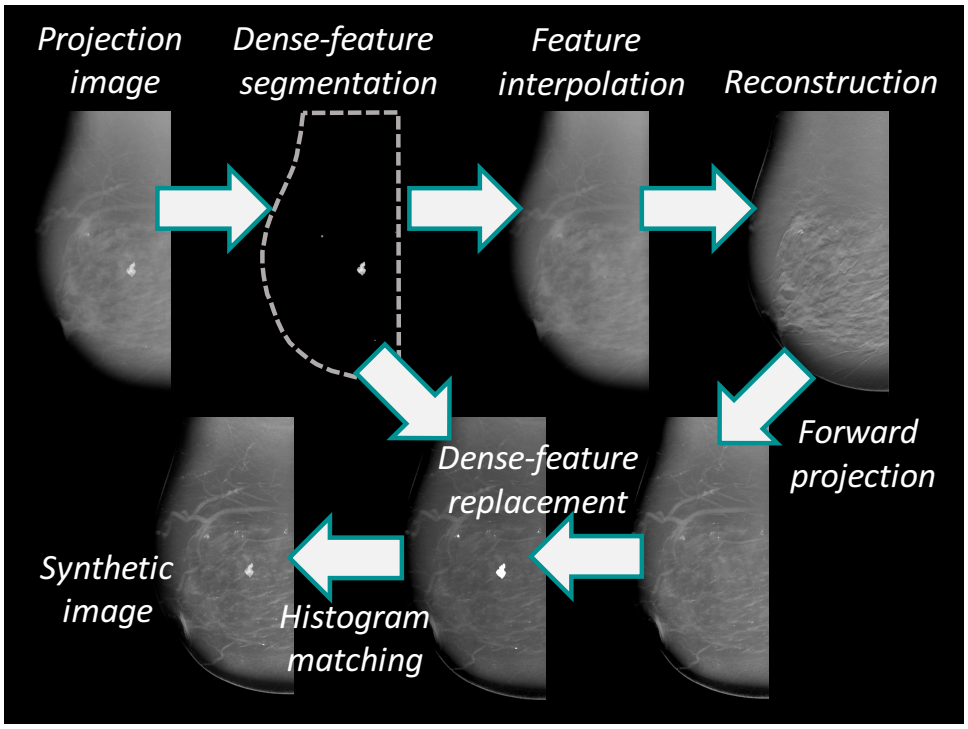


Figure 3. 7. Key image processing steps for dense-feature artifact reduction applied to *stationary* digital breast tomosynthesis (sDBT), including examples showing the evolution of the image as it progresses through the processing chain. Segmentation and interpolation-based in-painting of the dense feature at the level of the projection view was followed by a histogram matching step to replace the dense features from the central projection view back into the *synthetic* mammogram. Figure adapted from [Puett 2019b].

It began with a threshold-based segmentation of the dense features in the projection images. New pixel values in the region of the segmented dense features were assigned by interpolation-based in-painting, after which the modified projection images entered the reconstruction and forward projection steps to produce a *synthetic* mammogram without the dense feature or its associated artifact. Since these dense features can have diagnostic value, they were replaced in the *synthetic* mammogram prior to display. In order to avoid the computationally-expensive registration step, the mask from the central projection image was used for dense-feature replacement, followed by a histogram matching step to adjust its pixel values to be compatible with the *synthetic* image as a whole. This approach allowed for the same mask to be applied to all of the *synthetic* mammograms, regardless of the various forward

projection steps used to generate them (see 3.5.3e Forward projecting the 3D image space into *synthetic* 2D mammograms). Additionally, given the relatively high levels of noise in the projection images of breast tissue, a morphological opening algorithm was used during segmentation to prevent features smaller than 4 square pixels from being segmented. Finally, since many of the dense features in breast tissue have poorly defined edges, such as the irregular margins of calcifications, the mask was dilated by 3 pixels to ensure segmentation of the feature in its entirety. This small amount of over-segmentation was unlikely to interfere with the visualization of important features, as this information was placed back into the *synthetic* image prior to display.

*3.5.3d Reconstructing 3D images from 2D projections*

Reconstruction refers to the processing steps that generate the 3D stack of image slices from the information available in the multiple 2D projection views collected at the time of the study (see 2.6 The image processing chain that generates sDBT images and the value of the *synthetic* mammogram and 3.5.3a The image processing chain for sDBT in context). During the course of this dissertation work, a flexible reconstruction algorithm was developed to test different reconstruction approaches, including direct filtered backprojection and algebraic iterative reconstruction, that could be applied to different system geometries. It provided a tool for simulating the application of CNT-enabled *stationary* tomosynthesis to many different imaging tasks, accommodating the wide variety of different source arrays currently being studied. However, when experimentation was carried out with the sDBT systems at the clinical level, highly customized reconstruction algorithms, which had previously been developed specifically for the sDBT system, were employed. These included a filtered backprojection approach developed by Real Time Tomography (Piccolo 4.0.5, Real Time Tomography LLC,

Villanova, PA) [Lee 2019] and an adapted fan-volume modification of the simultaneous iterative reconstruction technique (AFV-SIRT) developed by a previous graduate student in the Applied Nanotechnology Laboratory [Wu 2015]. The latter approach with modifications was used in the optimized image processing chain to generate *synthetic* mammograms for sDBT [Puett 2019b, Puett 2020a].

*3.5.3e Forward projecting the 3D image space into synthetic 2D mammograms*

Forward projection refers to the processing steps that integrate the information in the reconstructed 3D image space into *synthetic* 2D images (see 2.6 The image processing chain that generates sDBT images and the value of the *synthetic* mammogram and 3.5.3a The image processing chain for sDBT in context). A specific Aim of this dissertation work was to develop a *synthetic* image capability for sDBT, and in the course of doing so, two processing approaches were explored and published. Based on a method developed previously [Diekmann 2009], an early approach incorporated tunable parameters into the forward projection step [Puett 2019b], thereby providing a mechanism to explore the effects of changes in the forward projection calculations on the display of clinically-important features, such as soft tissue masses and microcalcifications. This tunable forward projection algorithm ordered the intensities of the discretized 3D image space through depth and applied polynomial functions of varied order ($x^N$, where N = polynomial order) to weight these intensities before integrating through depth to assign an intensity value to the corresponding pixel in the *synthetic* image (Figure 3.8).

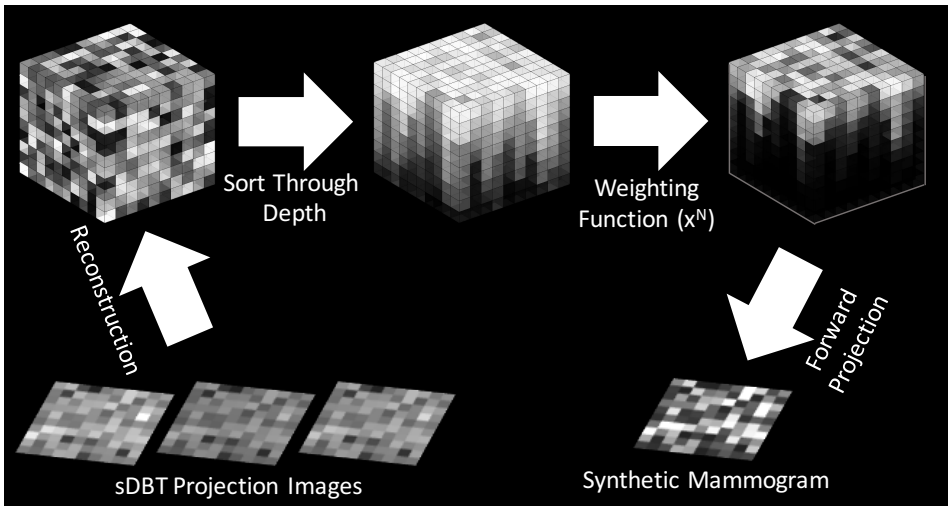


Figure 3. 8. Pictorial representation of the weighted approach to forward projection, which was used in the image processing chain to generate *synthetic* mammograms from the information contained in the projection images collected by *stationary* digital breast tomosynthesis (sDBT). The weighting function consists of polynomials of varied order ($x^N$) that exist between the extremes of zero-order, yielding an average-intensity forward projection, and infinite-order, yielding a maximum-intensity projection. Figure adapted from [Puett 2019b].

The range of weighted functions existed between the extremes of an average-intensity projection (zero-order) and maximum-intensity projection (infinite-order). Experimentation was performed using breast mimicking phantoms as well as patient images containing suspicious breast lesions. Findings through phantom-based experimentation using this tunable approach toward forward projection guided the development of computationally more efficient and clinically more useful algorithms [Puett 2020a].

The optimized forward projection approach developed through phantom-based experimentation for advancement to testing at the clinical level incorporated feature enhancement achieved through a combination of processing steps. Figure 3.9 provides an overview of the key processing steps that follow reconstruction, including feature identification, feature weighting, and weighted forward-projection, which taken together sought to enhance the display of the microcalcifications and masses in the final *synthetic* images.

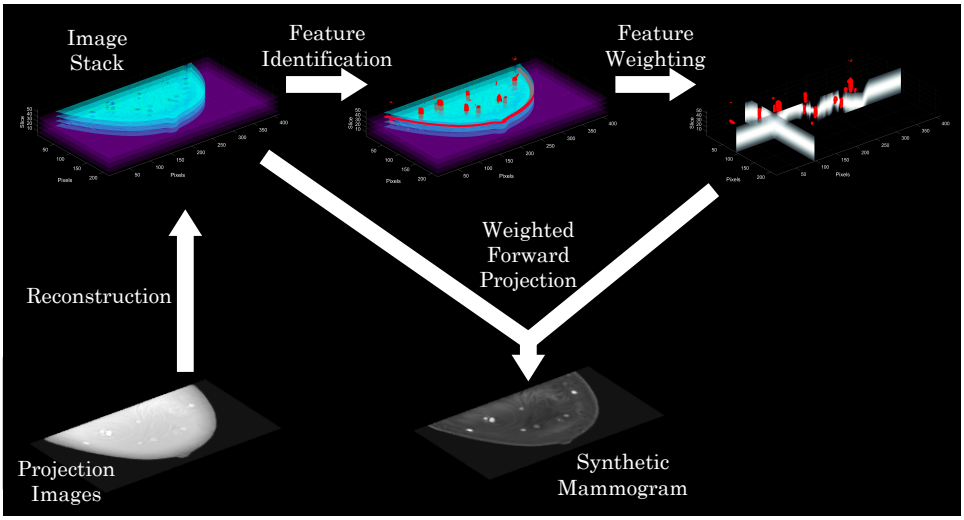


Figure 3. 9. Schematic diagram of the flow of information through the feature identification, weighting, and weighted-recombination steps used to generate *synthetic* mammograms for stationary digital breast tomosynthesis (sDBT). These processing steps sought to separate features-of-interest, such as microcalcifications and masses, from the obscuring effects of background features at different depths and them emphasize them to produce pathology-enhanced *synthetic* images. Figure adapted from [Puett 2020a].

The process of identifying features-of-interest in the sDBT 3D image space began with a Laplacian decomposition of each slice in the reconstructed image stack (Figure 3.10) [Puett 2020a]. As has been demonstrated for both standard and *synthetic* mammography, decomposing the image into its high, mid, and low-frequency components yields modified images emphasizing different feature-elements of clinical importance [Wei 2005, Wei 2019]. Microcalcifications and mass edges are high-frequency components, while the body of masses tend to be mid-frequency components. Through decomposition, the initial reconstructed image stack was separated into three separate sub-stacks, each containing slices filtered by frequency.

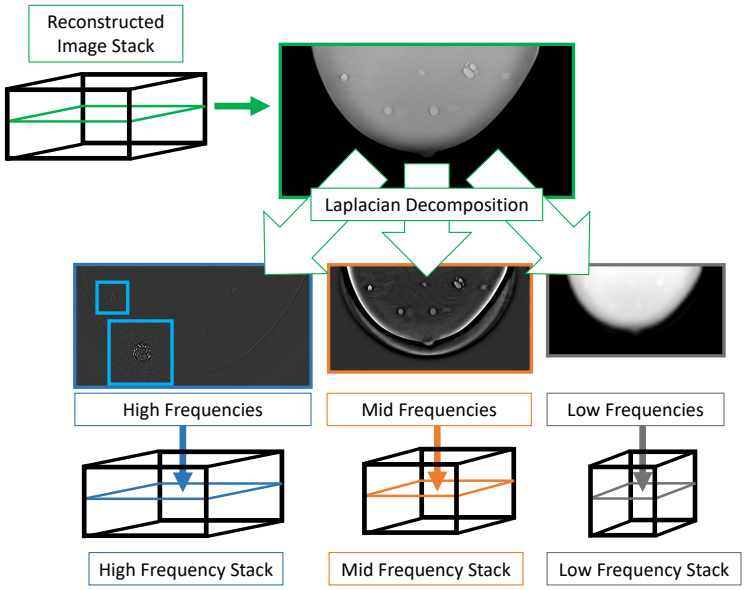


Figure 3. 10. Pictorial representation of the use of Laplacian decomposition as a processing step during feature-identification. Laplacian decomposition of each slice in the reconstructed 3D image stack produced three frequency-sorted sub-stacks. Since microcalcifications and mass edges tended to be captured in the high-frequency images, the bodies of masses in the mid-frequency images, and background tissues in the low-frequency images, this processing step provided an initial separation of diagnostically-important features.

Following decomposition, microcalcification and mass features were identified and then weighting functions were generated for each specific feature-of-interest (Figure 3.11). Feature detection was a key step in the image processing chain. Many different feature-detection algorithms have been developed, each involving trade-offs in computational efficiency and utility. In this study, microcalcifications were identified and weighted by sorting the high-frequency sub-stack by intensity through depth (Figure 3.11A). Combining information from the slices containing the brightest features was equivalent to performing a maximum-intensity forward projection through the stack. The microcalcification weighting-function developed for sDBT emphasized the two brightest-intensity slices and the two darkest-intensity slices. Including the darkest two slices in the weighting function helped to remove the bright streak artifacts associated with the edges of metal and large calcifications.

Mass identification and weighting were done in the mid-frequency sub-stack (Figure 3.11B). Initial phantom-based work generating sDBT synthetic images used a blob-enhancement filter to identify mass-like features against a uniform background [Puett 2020a]. However, because of the complex backgrounds and varied feature characteristics presented by the CIRS Imaging phantom and clinical images evaluated in this study, the blob-enhancement filter did not perform well, leading to the approach of identifying masses in the mid-frequency sub-stack as maximally stable extremal regions (MSER) using the MSER algorithm in MATLAB (The MathWorks, Inc., Natick, MA) [Puett 2020a], which is an approach that has been utilized by others to detect masses in standard mammograms [Hassan 2019]. Following detection, a smooth weighting function with a depth thickness of 1 cm was generated through the mass features in order to emphasize the mass while de-emphasizing background features at other depths. The mass-weighting function was then resized to match the size of the high-frequency sub-stack in order to register the body of the mass with its boundary, since mass edges are high-frequency image components and were therefore best represented in the high-frequency sub-stack. The weighting function was optimized to emphasize the features-of-interest and de-emphasize overlapping structures present at different depths.

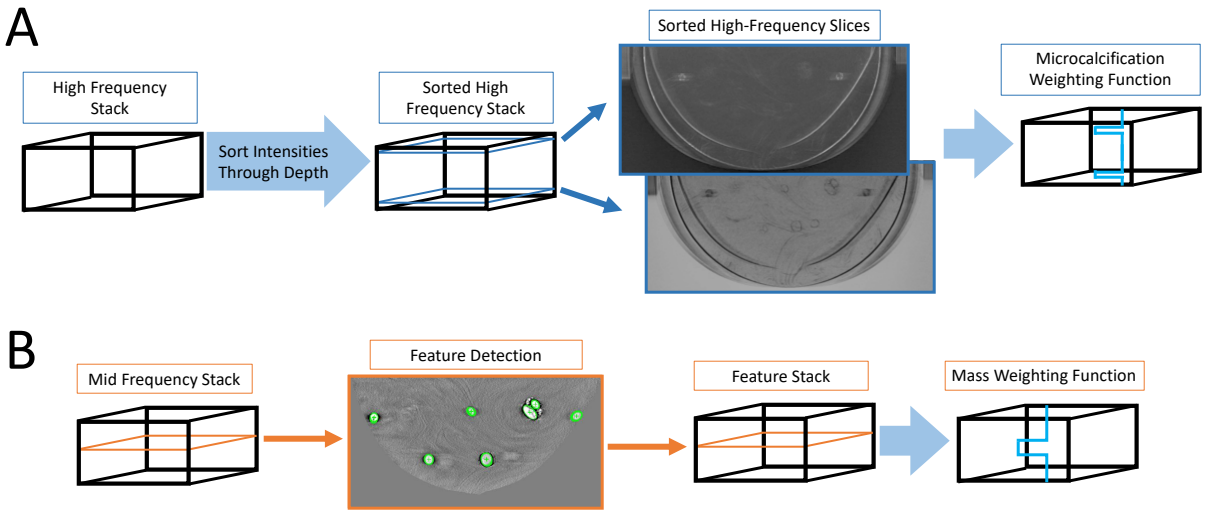


Figure 3. 11. Schematic representation of the feature identification and weighting steps used to emphasize pathology in the *synthetic* mammograms generated for *stationary* digital breast tomosynthesis (sDBT), including example images demonstrating the information being enhanced by the processing. Sorting the high-frequency sub-stack by intensity through depth identified microcalcifications (A). The example images show the sorted slices in the reconstructed image stack containing the most intense (brightest) and least intense (darkest) features. An optimized weighting function combined the information in these images, thereby emphasizing the calcification while minimizing streak artifacts. Masses (B) were identified in the mid-frequency sub-stack as maximally stable extremal regions or by the application of a blob filter. A weighting function emphasized the mass while de-emphasizing background features at different depths.

Forward projection of the weighted and unweighted, frequency-sorted sub-stacks yielded a set of 2D images, which were then blended using a weighted recombination step to generate a standard *synthetic* mammogram as well as two pathology-enhanced *synthetic* images, one dedicated to the display of microcalcifications and the other to the display of mass lesions (Figure 3.12).

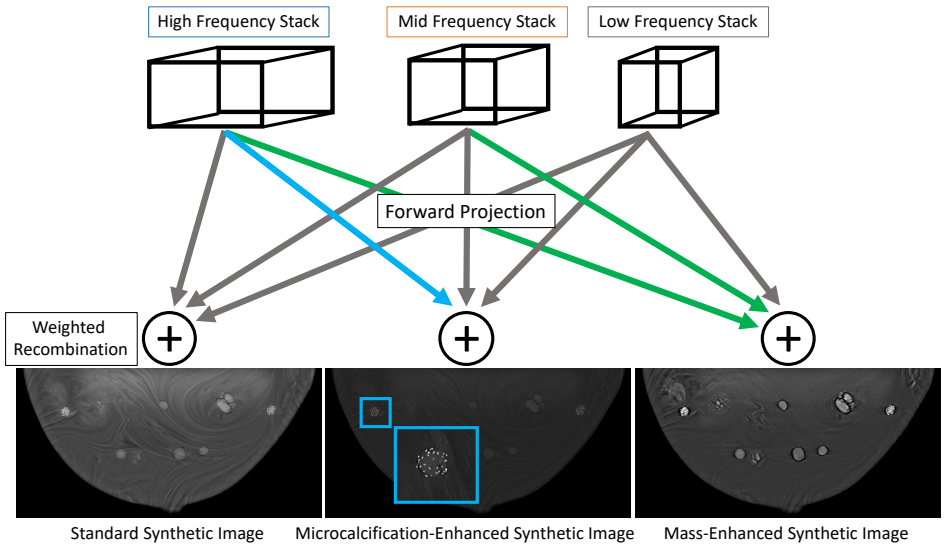


Figure 3. 12. Schematic representation of the final weighted recombination step used to generate pathology-enhanced *synthetic* mammograms for *stationary* digital breast tomosynthesis (sDBT), including examples of *synthetic* images of breast-mimicking phantoms. Forward projection of both the weighted and unweighted frequency-sorted sub-stacks produced a set of 2D images. Weighted recombination blended these images into a standard *synthetic* mammogram as well as two pathology-enhanced *synthetic* images, one dedicated to the display of microcalcifications and the other to the display of masses. The blue arrow shows the path of microcalcification-weighted information, and the green arrows show the path of mass-weighted information.

To summarize, in a general sense, the image processing steps developed through this work to generate the *synthetic* mammogram sought to combine the benefits of the 3D image stack, which separates features-of-interest through depth, with the efficiency of the 2D mammogram. To do so, the processing identified mass and microcalcification features in the image slices of the reconstructed image stack and then emphasized these features-of-interest over background features present at different depths when displayed in the final *synthetic* image. The key processing steps combined Laplacian decomposition, feature weighting through depth, and weighted re-combinations of slices emphasizing different image characteristics to produce a unique set of *synthetic* images, including a standard *synthetic* image as well as *synthetic* images dedicated to the display of specific pathologies. The decision to generate separate pathology-enhanced images was based on the recognition of the significant differences in the imaging

characteristics of masses and microcalcifications and the very different processing steps needed to optimize their display. Additionally, this decision was informed by experience developing image processing approaches for *synthetic* dental radiography (see APPENDIX: Developing *synthetic* dental radiography) and the realization of the potential value of offering a set of *synthetic* images, each displaying unique information.

*3.5.3f. Equalizing background in the synthetic mammogram*

During patient imaging, the outer non-compressed breast tissue is typically thinner than the more central compressed tissues. As a result, the background image signal in the peripheral regions of the breast decreases toward the skin line, leading to decreased feature visibility in these regions and loss of the clinically-important skin line. Processing is needed to provide a stable background between the central and peripheral breast image regions and establish a continuous skin line. The background equalization approach (Figure 3.13) developed for this study worked with a factor-4 down-sampled version of the *synthetic* mammogram to improve computational efficiency. The peripheral breast region was first segmented using k-means clustering [Lloyd 1982]. Next, the background signal in the peripheral region was estimated by fitting a smoothing spline to each row and then each column in the down-sampled image. The background-fit image was then up-sampled to the original size of the *synthetic* mammogram and used to normalize the background signal.

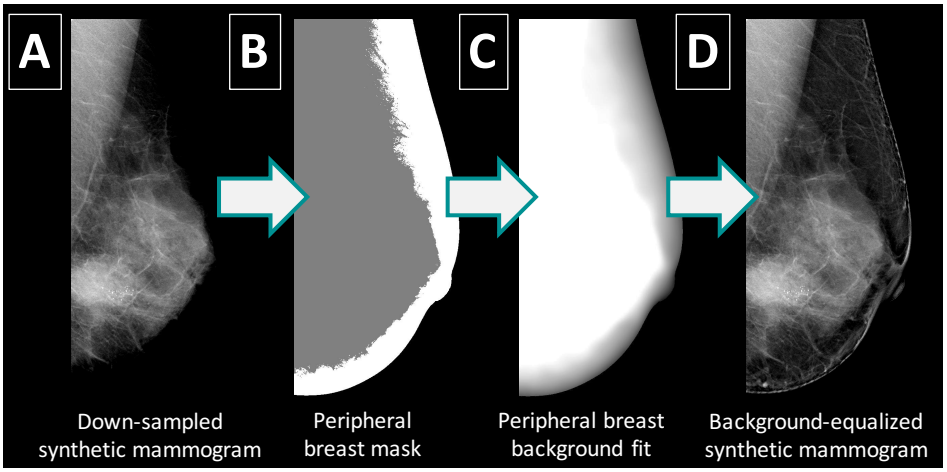


Figure 3. 13. Schematic overview of the background-equalization algorithm applied to a *synthetic* mammogram generated by *stationary* digital breast tomosynthesis (sDBT), including representative examples of the changing appearance of an actual breast image in response to these processing steps. First, the *synthetic* image was down-sampled by a factor of 4 to improve the computational efficiency (A). Next, the peripheral breast region was segmented using a k-means clustering approach (B). A smoothing spline was fit to the changing background signal in this peripheral region (C). The background-fit image was then up-sampled to the original size of the *synthetic* mammogram and used to normalize the background signal (D). Figure adapted from [Puett 2019b].

### *3.5.4 Displaying images*

The equipment used to display breast images has a significant impact on the visibility of features, as a high resolution is needed to visualize small structures such as microcalcifications. The work in this dissertation was made possible by the state-of-the-art hardware and software supporting the digital imaging systems used by the UNC Department of Radiology and the imaging research facilities. These included software with Digital Imaging and Communications in Medicine (DICOM) sharing capability as well as access to 5-megapixel display monitors with reader ability to manipulate the image display.

## 3.6 Data analysis methods

### *3.6.1 Measuring image quality and feature detectability*

*3.6.1a Quantifying signal and noise*

Assessing the quality of the images generated by the sDBT system played a key role throughout the work presented in this dissertation. There are many objective measures of the information displayed in an image based on the intensities or grayscale values present in the image itself. The average intensity over a defined region is typically known as the Signal, while the variability in the intensity over a defined region with stable features reflects Noise. Ratios involving Signal and Noise, such as Contrast [$(Signal_{feature} - Signal_{BKG})/Signal_{BKG}$] and the Signal-difference-to-Noise ratio (SdNR) [$Signal_{feature} - Signal_{BKG}/Noise$], also referred to as the contrast-to-noise ratio (CNR), provide insight regarding the ability to see an image feature against its background. As such, these measures are useful and were calculated in many of the experiments in this dissertation. For example, comparison of the display of the microcalcification and mass mimics in the 2D images of breast-mimicking phantoms produced by FFDM and the *synthetic* images generated by the DBT and sDBT systems involved measuring the feature's contrast, signal-difference-to-noise ratio (SdNR), and full-width-at-half-maximum (FWHM). FWHM can be used to define the edges of a feature based on its relative intensity. As such, it provides a useful tool to compare feature sizes in images with different intensity levels. However, FWHM can also be used as a reflection of blur when imaging small features, and as such, it can provide insight into the resolution of an imaging system. Measuring microcalcification size is a good example (see 3.6.1c Measuring microcalcification size). As the size of the microcalcification approaches the resolution the system, it appears blurred in the image. This blurring is a progressive change of increasing relative area but decreasing Signal

intensity, as microcalcifications of smaller and smaller size are displayed. Eventually, the contrast becomes too low to distinguish the microcalcification from its BKG, and therefore, it cannot be detected (see 4.3.1Visualizing microcalcifications in lumpectomy specimens).

Contrast was calculated as the difference between the mean signal intensity of the feature and its BKG, normalized by the mean BKG intensity. In this work, the mean intensity of the feature was calculated in the circular area centered in the feature and extending to one-half the radius of the feature, and the mean BKG intensity was calculated in the concentric ring around the feature at a distance of 1.5 times the feature's radius. Noise was quantified as the standard deviation of the pixel intensities within the background. To measure the FWHM, 1D Gaussian functions were fit through the center of each microcalcification in the x- and y-directions. Ten-fold interpolation of each Gaussian function allowed for a more precise measurement of the FWHM, which was calculated as the average of the FWHM measured in the x- and y-directions.

*3.6.1b Calculating detectability indices*

Much of the work reported in this dissertation required an objective measure of the visibility or detectability of a feature-of-interest in an image, such as a mass or microcalcification. In this way, quantitative comparisons could be made between images produced by different modalities or generated by different processing techniques. A detectability index (d') provided this objective measure. The calculation of d' was based on a published method [Ikejimba 2014], which was adapted to account for the unique processing steps used to generate sDBT-based images, including the *synthetic* mammogram [Puett 2019b]. d' incorporated measures of overall image quality (resolution and noise) and characteristics of the feature-of-interest (size and contrast) to yield a single value reflecting visibility of the feature. For application with the sDBT system, resolution was measured as the MTF calculated from the

changing intensity values off a straight metal edge, and noise was quantified as the averaged noise periodogram measured in featureless breast-mimicking phantoms ranging from 3-5 cm in thickness. The resolution/noise ratio was multiplied by a Gaussian task function ($W$) that accounted for the size of the feature-of-interest, and the task function was normalized such that the total signal power corresponded to the area under the feature profile [Ikejimba 2014]. Finally, this metric was scaled by the feature's contrast to obtain d' [Eq. (3.8)].

$$d' = \left[\int \frac{[resolution(f)]^2}{[noise(f)]} * W(f)^2 * [contrast]^2 df\right]^{1/2} \quad (3.8)$$

Figure 3.14 displays representative examples of the resolution, noise, and task functions used to calculate d' in sDBT-generated *synthetic* mammograms.

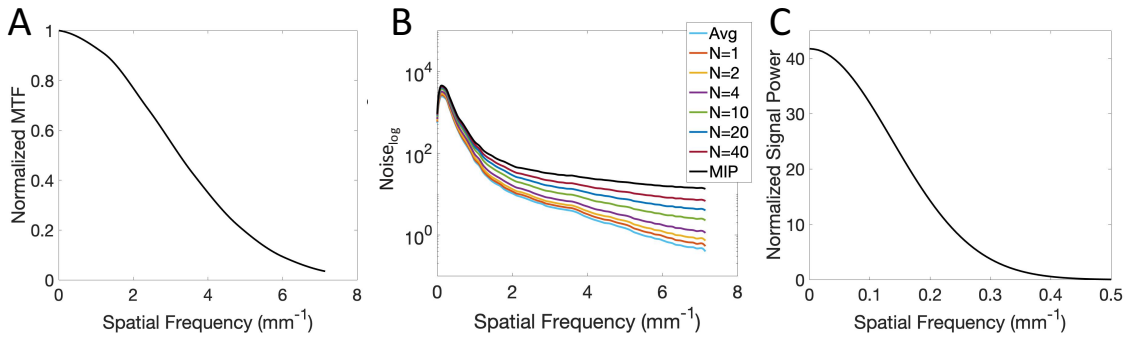


Figure 3. 14. Representative plots of the resolution, noise, and task functions used to calculate a detectability index (d') for use with the *stationary* digital breast tomosynthesis (sDBT) system. Resolution (A) was measured as the modulation transfer function (MTF) in *synthetic* images of a metal edge, while noise (B) was measured as the averaged noise periodogram in featureless breast-mimicking phantoms. The example task function (C) was modeled using a Gaussian-shaped 5-mm mass. Note the relationship of increasing noise with higher-order weighting (N values) during forward projection (B), ranging between an average (Avg) and maximum-intensity projection (MIP), when measured in a 5-cm thick phantom.

*3.6.1c Measuring microcalcification size*

When assessing the visibility of microcalcifications, which provide key diagnostic information in mammography, objective measures of calcification size in both the planar (x-y) and depth (z) dimensions can be helpful and were used in the study imaging lumpectomy

specimens with standard 2D mammography, conventional DBT, and sDBT [Puett 2019a]. Microcalcification size was measured as a planar area in the in-focus image slice reconstructed from both the full resolution and binned sDBT projection images and the moving-source DBT projection images. The microcalcification sizes were reported in relation to the size of the same microcalcification measured in the magnified mammography image. An artifact spread function (ASF) was used to determine the depth thickness of the microcalcification as displayed through the reconstructed image stacks of sDBT and conventional DBT.

Area measurements were based on pixel intensities. First, an ROI was drawn manually around each microcalcification to include the adjacent BKG region but avoid other highly attenuating features. Segmentation of each microcalcification was accomplished by fitting Gaussian functions through the brightest pixel in both the x and y directions. The 50% intensity values of each Gaussian fit were then averaged to yield the threshold for segmentation. Segmenting all pixel values greater than this threshold provided a mask, from which the largest connected component was identified as the microcalcification. As such, the segmented region reflects the full-width at half-maximum (FWHM) of each microcalcification. The area was then calculated by multiplying the number of pixels in the segmented region by the area of each pixel. Since each image represents a 1.8x magnification, the pixel dimensions were divided by 1.8 when calculating the actual microcalcification size.

The ASF quantifies the contrast of an attenuating feature in the reconstructed image slices above and below the in-focus plane [Wu 2004]. It was calculated for each reconstructed image slice as the difference between the average intensity in the same ROI that defined the microcalcification and the average intensity of the surrounding BKG. Plotting the ASF as a function of distance from the in-focus plane quantifies the changing intensity with depth. Each

ASF was normalized by its maximum value (from the in-focus plane). In this study, FWHM of the ASF was used as a quantitative measure to compare display through depth in the sDBT and moving-source DBT image stacks.

### *3.6.2 Assessing reader performance and preference*

Although quantitative measures of image quality based on pixel intensity values within the image itself (see 3.6.1 Measuring image quality and quantifying feature detectability) are useful, quality at the clinical level is best determined by the diagnostic utility of the information displayed in the image. In other words, is the information displayed in a way that a trained reader is likely to make an accurate diagnosis? Assessing the clinical utility of an image therefore requires the participation of trained readers. Typically, studies of this nature ask several readers to complete questionnaires as they interpret images, often recording their preferences when interpreting specific features and confidence in reaching a correct interpretation, as they view images generated by different modalities. If structured appropriately, the answers to these questions, along with some knowledge of ground truth such as pathology, can also be used to measure reader performance (diagnostic accuracy). These multi-reader multi-case studies are now accepted as standard tools for evaluating the clinical value of imaging technologies and were utilized during this dissertation work, usually comparing sDBT images to standard 2D mammograms and/or conventional 3D mammograms for reference [Lee 2019, Puett 2019a]. The data collected in these studies are subjective and are therefore influenced by many factors, such as reader training, experience, and fatigue [Lee 2019, Gilbert 2015]. As such, care must be taken to select appropriate readers and provide a study protocol that is understandable and user-friendly. A variety of reader studies have been performed to assess CNT-enabled *stationary* tomosynthesis when applied to a host of different imaging tasks, including chest, dental, and

orthopedic imaging. These readers typically have minimal experience with tomosynthesis imaging, since these applications are predominantly in pre-clinical testing. However, much more extensive clinical experience is available with breast imaging given the widespread use of DBT, allowing for the design of detailed reader studies assessing not only reader preference but also comparisons of reader performance. As a result, the clinical utility of images generated by sDBT could be compared to standard mammographic techniques. A detailed reader study was conducted to assess the clinical potential of sDBT [Lee 2019]. During this study, readers compared the reconstructed 3D image stack of sDBT to standard 2D mammograms of patients with concerning breast lesions detected by standard screening mammography (see 3.4.3 Patient selection for human study).

Four fellowship-trained breast imaging radiologists participated in the multi-reader multi-case, paired-image study comparing the sDBT-generated 3D image stack to the standard mammogram [Lee 2019]. The readers averaged 15.3 +/- 6.8 years (10 to 25) of experience with mammography and 3.8 +/- 2.5 years (0 to 5) of experience with DBT. Only one reader had zero years of experience with DBT. Each reader was first presented with either the mammogram or sDBT image stack for a particular patient. Readers answered a questionnaire, rating the likelihood of malignancy (0 to 100% in increments of 10%), the density of breast tissue (BIRADS A-D classification) [Sickles 2013], and confidence in their overall impression (1 to 10 scale). Images of the same patient by the other modality were then immediately presented, and readers used a 7-point scale (-3 to +3) to rate a preference compared to the initially-presented modality when assessing diagnostically-important image features using accepted descriptors of mass margin and shape, architectural distortion, asymmetry, and microcalcification morphology/distribution [Sickles 2013]. The order of cases and the modality presented first were

random. After a wash-out period of at least four weeks, the image pairs were presented to the same readers. The patient order was again randomized, but the modality viewed first was reversed. The questionnaire was again completed. This study design reduced the bias associated with viewing a particular imaging modality first, since the reader determined the likelihood of malignancy for each modality before interpreting images from the other modality. Readers were not provided with any clinical information and were unaware of the pathology results.

Reader performance was quantified as the area under the receiver operating characteristic (ROC) curve (AUC). In this study, ROC curves for sDBT and mammography were generated for each reader using the reader's reported likelihood of malignancy during image interpretation. The likelihood of malignancy cutoffs (0 to 100%, in 10% increments) provided thresholds around which sensitivity and specificity were calculated based on the actual presence of malignancy, as determined by pathology. Given the relatively small number of cases, Tukey's pseudovalue estimation with jackknife resampling was used to correct for bias at each threshold (R 3.4.0, R Foundation for Statistical Computing, Vienna, Austria and RStudio 1.1.456, RStudio, Inc., Boston, MA USA). Plotting the true positive rate (sensitivity) as a function of the false positive rate (1-specificity) for each threshold defined a relationship through which the ROC curve was fit using logistic regression analysis (MATLAB R2018a, The MathWorks, Inc., Natick, MA USA).

Inter-reader agreement was quantified using the Fleiss kappa (κ) statistic for mammography and sDBT. This calculation involves selecting a threshold for the readers' reported likelihood of malignancy in order to categorize each interpretation as malignant or benign. Agreement was calculated at thresholds of 0.5 and 0.8. Likelihood of malignancy values greater than the threshold were considered to be a malignant finding, while values less than or

equal to the threshold were considered benign. κ values were interpreted using the guidelines described by Landis and Koch [Landis 1977]. Intra-reader agreement could not be assessed, as readers rated a likelihood of malignancy for each case using each modality only once.

In order to compare the aggregate reader performance with respect to each modality and assess the influence of specific breast characteristics, such as tissue density and compressed thickness, on performance, a multivariate analysis was performed by fitting a linear mixed-effect model (SAS 9.4, SAS Institute, Inc., Cary, NC USA). The fixed-effects were the difference between the two modalities and breast characteristic of interest, and random-effects were used to account for within-patient and within-reader correlations. An F-test compared the mean AUCs between mammography and sDBT.

A similar multivariate analysis was used to assess reader preference when interpreting diagnostically-important image features: mass margin and shape, architectural distortion, asymmetry, and microcalcification morphology/distribution. In this type of analysis, scores significantly greater than zero indicate a preference for sDBT while scores significantly less than zero indicate a preference for mammography. Means are reported with their confidence interval (CI), with p-values less than 0.05 defining statistical significance. Average reader confidence in overall interpretation using mammography and sDBT was compared by Student's t-test with p-values less than 0.05 defining statistical significance.

### 3.7 Trustworthiness of the study designs and findings

In large part, the work presented in this dissertation involved assessing the value of the information available in images produced by sDBT, often using standard 2D mammography and conventional 3D mammography as references for comparison. The study designs were modelled on accepted protocols established in the literature to answer the questions being asked, using the

most rigorous methods to assess image quality, such as detectability indices and reader studies. Assessing the visibility of soft tissue features and microcalcifications yielded consistent findings across the spectrum of testing with breast-mimicking phantoms, lumpectomy specimens, and human subjects throughout this dissertation work. Additionally, the findings of these studies were compared to the large body of literature assessing DBT performance for each task. Consistency in these findings support the reliability of the results and the appropriateness of using them to guide future research and development. Admittedly, the analysis of reader preference and performance is complicated, requiring the use and implementation of advanced statistical testing. To ensure the validity of the findings, guidance was obtained by medical biostatisticians who selected and performed the evaluation after face-to-face discussions regarding the study protocol and data collection techniques.

## 3.8 Limitations of the study designs

### *3.8.1 Limitations imposed by technological differences in imaging systems*

Assessing the clinical potential of sDBT involved comparing its performance to standard 2D and conventional 3D mammography. However, sDBT is a novel technology, and there are a host of significant technical differences between sDBT and the imaging systems to which it was compared (see 2.2.4 The clinical value and technical limitations of conventional 3D mammography and 3.5.1a Differences in the breast imaging systems). Many of these differences directly impact the quality of the images generated by the system, with image quality often being the primary measure for comparison. The devices utilized in this work differed in terms of their geometric configuration, focal spot size, anode material, beam filtration, and selected technique (exposure and kVp) for a given breast thickness (Table 3.1). As a result, there were differences in the dose and beam quality between the FFDM, conventional DBT, and sDBT systems during

image acquisition. Additionally, the FFDM systems employed scatter-rejection grids, and detectors from different manufacturers used different pixel sizes and detection methods. All of these differences have an effect on the overall performance of the system and thus the quality of the images it produces (see 3.5.1a Differences in the breast imaging systems).

### *3.8.2 Limitations inherent to phantom-based experimentation*

Much of the work in this dissertation involved phantom-based experimentation. There are two key limitations inherent to this experimental approach. First, the operation of the standard 2D and 3D mammography systems to which the sDBT system was compared have been optimized for patient, not phantom, imaging. As such, it was unclear if the proprietary techniques for selecting the operational settings during image acquisition or the proprietary image processing algorithms utilized after image acquisition were generating images of the highest possible quality for that device. In contrast, the operational settings and post-acquisition processing approaches for sDBT could be adjusted throughout experimentation to maximize image quality. Second, measurements of quality and feature detectability in the images of breast-mimicking phantoms do not correlate directly with clinical value.

### *3.8.3 Limitations with image processing*

Choices made in the image processing algorithms that produce the computer-generated images displayed to readers affect the visibility of features in the sDBT images. For example, the slices in the sDBT-generated 3D image stack were reconstructed at a thin increment of 0.5 mm to ensure that small features, such as microcalcifications, were displayed sharply. However, presenting a larger stack of thinner slices may contribute to reader fatigue, as there are more images to review. In this study, the sDBT image stacks ranged from 44 to 150 slices, compared to the single mammogram. Also, the tomographic nature of the displayed DBT image stack can

make the assessment of microcalcification clustering more difficult, since individual microcalcifications belonging to a cluster may be separated through multiple slices. Appreciating the spatial association of microcalcifications may therefore be more problematic as the slice thickness decreases. Recognizing the problems inherent with the display of the reconstructed 3D sDBT image stack provided the motivation for incorporation of a *synthetic* mammography capability into sDBT through the development of forward projection algorithms customized to this new imaging technology.

However, there are a host of concerns with increased manipulation of the information in images displayed for interpretation. Some of these concerns are inherent to image processing in general, and others are more specific to the image processing approaches applied to sDBT in this dissertation work. First, image processing can potentially de-emphasize a feature-of-concern, increasing the chance that it will be missed when the image is interpreted, or even introduce potentially-worrisome patterns that were not originally present in the image, which may increase the chance of a false-positive diagnosis. For example, concern has been raised over introducing pseudo-calcifications through feature-enhancement algorithms into the *synthetic* mammogram [Ratanaprasatporn 2017]. Second, the processing developed for this study focused on improving the visibility of masses and microcalcifications. However, architectural distortion and asymmetries are also important soft tissue findings in mammographic imaging. Finally, although the findings from phantom-based experimentation suggest value to presenting a set of *synthetic* mammograms, with each image dedicated to the display of a specific pathology, the true clinical benefit of offering multiple images for interpretation will need to be confirmed, in order to justify the increased processing and storage expense as well as reader time required to work with additional images.

### *3.8.4 Limitations imposed by reader experience*

As with any new imaging technology being applied at the clinical level, the effect of training and experience on reader performance needs to be considered. Much of the work reported in this dissertation included reader participation, and the experience of the readers with DBT varied significantly, from no experience to 5 years. As noted in previous studies published in the literature, experience can have a significant impact on the experimental findings assessing reader preference and performance when interpreting images generated by a new technology [Wallis 2012]. This experience effect was evident in the reader study comparing sDBT to standard 2D mammography, in which the performance of the reader with no DBT experience differed the most from the other readers [Lee 2019] (see 4.3.2a Reader accuracy).

### *3.8.5 Addressing limitations and implications for future research*

Appreciating these limitations in study design led to attempts to minimize their impact on the findings. For example, a host of adjustments were made in recognition of the technological differences in the imaging systems. As much as possible, attempts were made to ensure equivalent radiation dose delivery during image acquisition through adjustments in exposure. When possible, post-acquisition adjustments in the image information were made to account for device differences, including mathematical corrections for differences in magnification factors, detector pixel sizes, and post-processing [Puett 2019a, Puett 2020a].

The limitations inherent with phantom-based experimentation in general and the concerns raised by the image processing approaches chosen specifically for this work emphasize the critical importance of ongoing reader studies to assess the true clinical value of the sDBT system as clinical experience grows. Particular attention needs to be directed at the feature-identification algorithms. For all image processing approaches designed to produce feature-

enhanced *synthetic* images, the accuracy of the feature-detection step is key. The feature-detection approach evolved through the course of this dissertation work, with an MSER-based approach being utilized in the image processing chain for clinical testing (see 3.5.3e Forward projecting the 3D image space into *synthetic* 2D images). Recent experience with conventional DBT has suggested that deep learning algorithms have the potential to improve the accuracy of feature identification [James 2018], although this approach requires algorithm training on a library of images offering a broad range of pathology. The image processing chain being developed for sDBT should accommodate a deep learning feature-detection algorithm, once experience with this technology is adequate to support the required training. This experience will involve continued patient imaging, although the option of developing a virtual model of the sDBT system and a library of virtual sDBT images should also be considered. Virtual testing is currently being explored for other breast imaging systems [Badano 2018].

## 3.9 Summary for Chapter 3: Methodology

This chapter provided the details of the study designs that generated the findings presented in this dissertation. First, the studies were placed in context, pointing out that 3D breast imaging is a very active research arena, driving rapid advances in technology and image processing techniques. The setting in which the research for this dissertation took place was then described, since a project of this scope, bridging basic experimentation with clinical application, would not have been feasible without a highly-collaborative environment of scientists and clinicians dedicated to advancing biomedical imaging. Second, the specifics of the materials and methods used during this dissertation work were provided. Emphasis was placed on the broad range of study designs, which included highly-controlled benchtop experimentation and human study. Finally, issues of the trustworthiness of the findings and limitations in the study designs

were discussed, including the impact that these limitations had on the interpretation of the data as well as their implications for future work with this new imaging technology.

# CHAPTER 4: FINDINGS

## 4.1 Introduction to Chapter 4: Findings

Chapter 4: Findings organizes the results of this work in terms of its three broad Aims: (1) understand the unique challenges of scatter and artifact with *stationary* digital breast tomosynthesis (sDBT), (2) assess the performance of sDBT relative to currently-available 2D and 3D mammography technologies, and (3) incorporate a *synthetic* mammography capability into sDBT (see 1.2 Purpose of this work and 1.3 Research questions asked in this work). The findings presented in this chapter have been published in peer-reviewed journals, as summarized in the figures and text presented herein.

## 4.2 The challenges of scatter and artifact with *stationary* tomosynthesis

### *4.2.1 Quantifying scatter in contrasted and non-contrasted sDBT images*

Studies were done to assess scatter in both contrasted and non-contrasted sDBT projection images. In these studies, scatter was measured indirectly using a beam-pass primary sampling device (PSD) to isolate the primary component of the total signal (see 3.5.2 Measuring scatter) [Puett 2018b]. Simple subtraction of the primary signal from the total signal, measured without the PSD in place, allowed calculation of the scatter signal. Scatter is perhaps best quantified as its relative contribution to the total signal, most commonly presented as the scatter-to-primary ratio (SPR). Similar to findings with conventional 2D [Chen 2015] and 3D mammography [Feng 2014], scatter increased in the sDBT projection images when moving from the periphery of the breast to central breast regions, with SPR climbing from about 0.2 to greater than 0.6 in some cases. Figure 4.1 provides a representative example of the changing SPR

contour when a customized 5 cm CIRS model 020 BR3D breast phantom (see 3.4.1 Breast-mimicking phantoms) is imaged by sDBT.

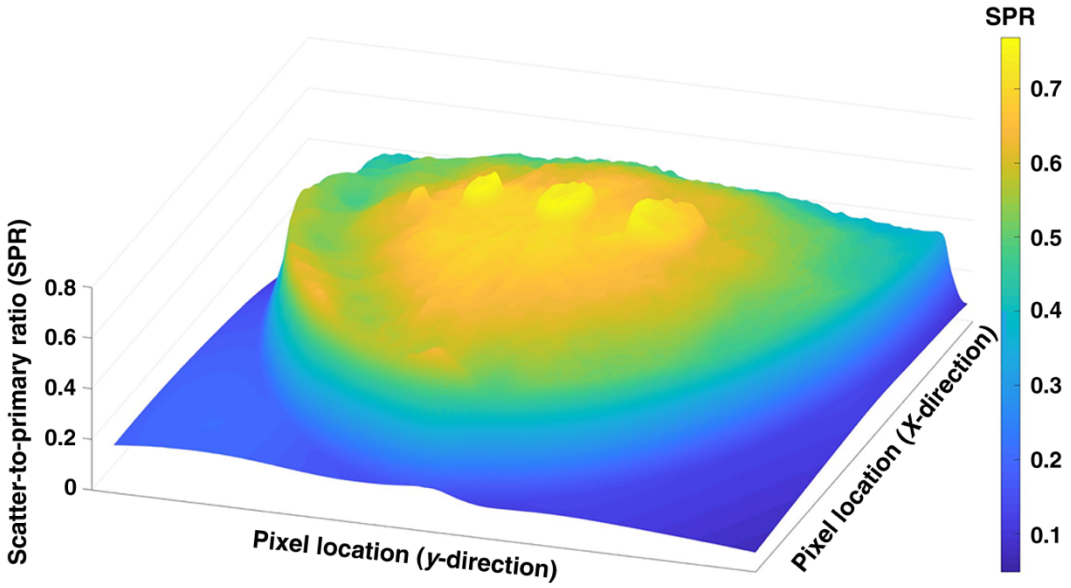


Figure 4. 1. Scatter-to-primary ratio (SPR) values in a representative projection image collected by *stationary* digital breast tomosynthesis (sDBT). In this example, the target was a 5-cm thick breast-mimicking phantom that had been customized with wells containing iodine to simulate contrast-enhanced imaging. Note the higher SPR values in central breast regions compared to peripheral regions and the highest SPR values in the iodine-containing well regions of the image. Figure adapted from [Puett 2018b].

Several factors were found to affect scatter during sDBT in both contrasted and non-contrasted breast regions (Figure 4.2). First, SPR was higher in regions containing iodinated contrast compared to adjacent background (BKG) regions, although SPR values were similar across the range of iodine concentrations (1-15 mg/ml), which reflected concentrations that can be achieved during human imaging. Second, SPR tended to be higher in images collected at a higher photon energy. Finally, scatter was most strongly correlated with compressed breast thickness.

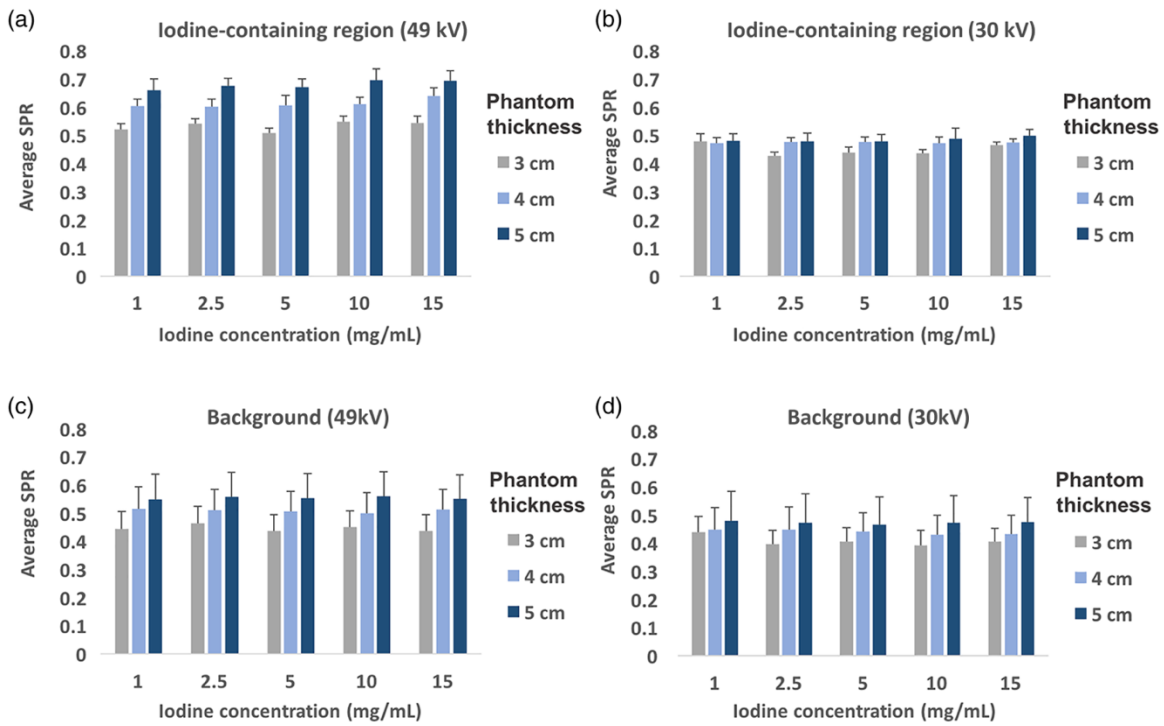


Figure 4. 2. The scatter-to-primary ratio (SPR) as a function of iodine concentration and breast thickness in projection images collected by *stationary* digital breast tomosynthesis (sDBT) directed at breast-mimicking phantoms that had been customized with wells containing iodine to simulate contrast-enhanced imaging. Imaging was done at both high (49 kVp) and low (30 kVp) photon energies during the temporal and dual-energy subtraction protocols. SPR was dependent on phantom thickness ($p < 0.05$ by ANOVA) in both non-contrasted (background) and contrasted (iodine-containing) regions. Also, SPR tended to be higher when images were collected at higher photon energy. Figure adapted from [Puett 2018b].

Scatter poses a unique challenge with tomosynthesis. Since oblique projection views must be collected, the use of standard scatter-reduction techniques during image acquisition, such as scatter-grids and air-gaps, is problematic (see 2.5 Image quality problems inherent to tomosynthesis in general and sDBT in particular). Therefore, correcting for scatter through image processing is important. Experiments for this dissertation compared different scatter correction algorithms, utilizing scatter maps based on sampled scatter values ($\text{ScatterMap}_{\text{direct}}$), calculated SPR values ($\text{ScatterMap}_{\text{SPR}}$), or a filtered (*f*) combination of both ($\text{ScatterMap}_{f\text{SPR}}$) (see 3.5.3b Creating scatter maps). The maps differed in their representations of scatter (Figure 4.3). Only maps including an SPR calculation [Figure 4.3(b) and 4.3(c)] captured the noise

component of the scatter signal. Therefore, unlike ScatterMap$_{SPR}$ and ScatterMap$_{fSPR}$, ScatterMap$_{direct}$ was smooth [Figure 4.3(a)]. Additionally, given the relatively sparse sampling by the PSD and the chance that an iodine-containing well was not adequately sampled, ScatterMap$_{SPR}$ tended to assign lower scatter values to regions of high attenuation [Figure 4.3(b)] compared with ScatterMap$_{fSPR}$, potentially underestimating scatter in areas of the image where there was a rapid change in the primary signal. The *f*SPR algorithm was designed to generate a scatter map that blended the most useful qualities of both ScatterMap$_{direct}$ and ScatterMap$_{SPR}$ [Wu 2017, Puett 2017].

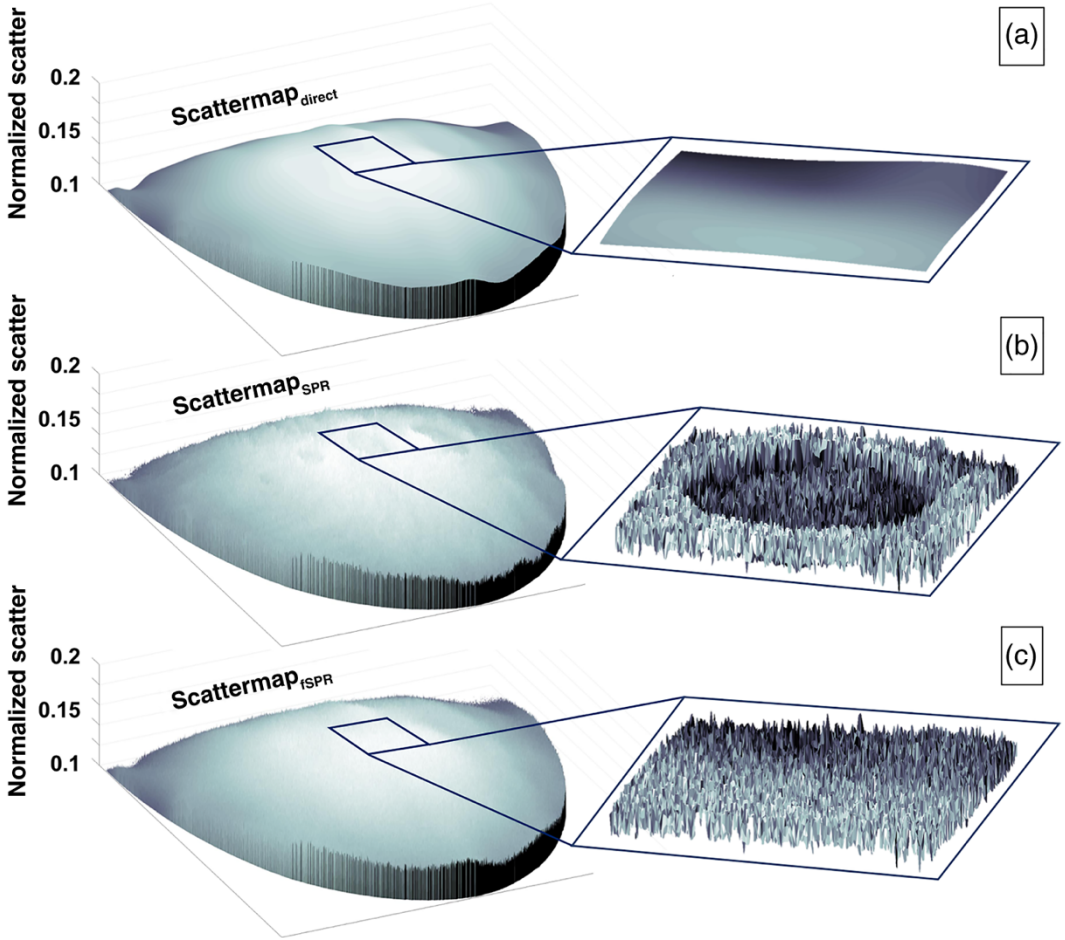


Figure 4. 3. Scatter maps generated from the projection images collected by *stationary* digital breast tomosynthesis (sDBT) directed at breast-mimicking phantoms that had been customized with wells containing iodine to simulate contrast-enhanced imaging. These representative scatter maps were generated using either (a) direct scatter values (ScatterMap$_{direct}$), (b) a scatter-to-

primary ratio (SPR) calculation ($ScatterMap_{SPR}$), or (c) a filtered (*f*) combination of both ($ScatterMap_{fSPR}$) from images of a 5-cm thick phantom with wells containing iodine at a concentration of 15 mg⁄ml collected at 49 kVp. The expanded views highlight differences in the region of the 1.5-cm diameter well. Note the noise component present in the scatter maps containing an SPR component, compared with the smooth direct scatter map. Also, note the lower scatter values assigned to the well region by the SPR map relative to the other maps. Figure adapted from [Puett 2018b].

Figure 4.4 displays the effect of applying the different scatter maps on the projection image. It superimposes two curves, which are line profiles through the contrast-containing well regions of the image. The colored profiles display the changing signal through the center of iodine-containing wells in representative projection images adjusted by the different scatter-correction techniques. The black profiles reflect the same path through the applied scatter map. The application of each map corrected the cupping artifact, which refers to the signal difference in central breast regions compared with the periphery. Additionally, the application of maps developed using an SPR calculation [Figure 4.4(c) and (d)] generated a smoother projection image compared with the application of $ScatterMap_{direct}$ [Figure 4.4(b)].

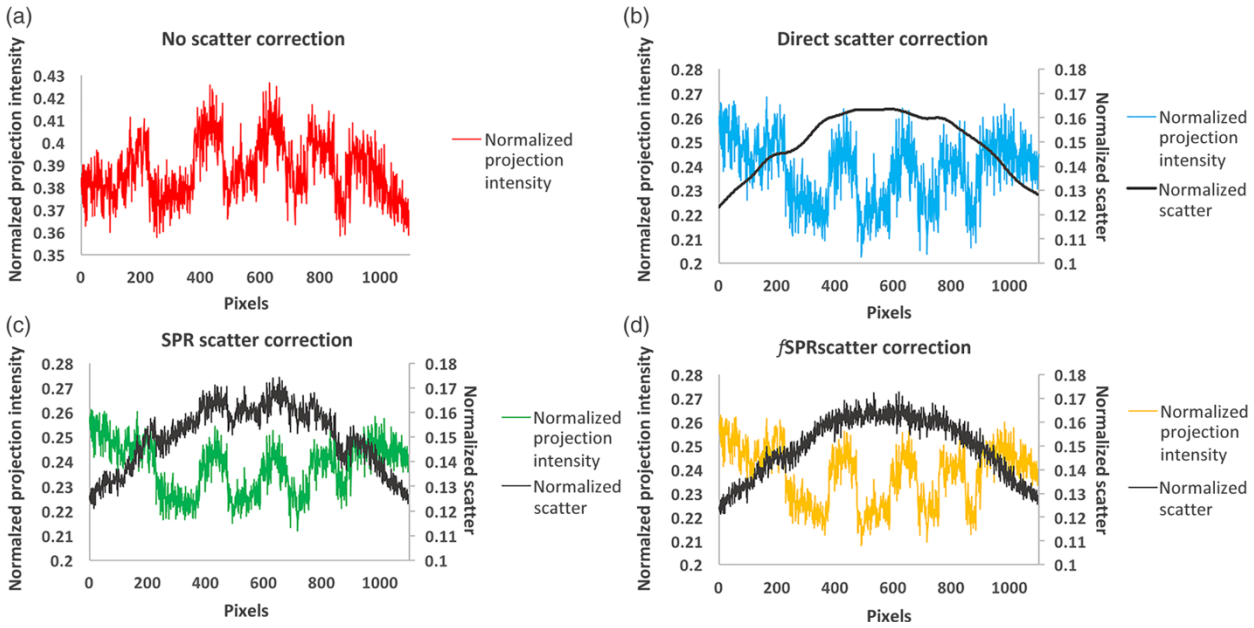


Figure 4. 4. The effect of applying different scatter-correction algorithms on the pixel intensity values in projection images collected by *stationary* digital breast tomosynthesis (sDBT) directed at breast-mimicking phantoms that had been customized with wells containing iodine to simulate

contrast-enhanced imaging. The profiles correspond to the path identified by the blue line in Figure 3.5. The blue, green, and gold profiles demonstrate the result of applying the different scatter maps (black profiles), including (b) direct scatter correction, (c) correction utilizing the scatter-to-primary ratio (SPR), and (d) the application of a filtered SPR (*f*SPR) map. which can be compared to the red profile (a) without scatter correction. This analysis was done on a projection image collected at 49 kVp of a 5-cm thick breast-mimicking phantom with wells containing iodine at a concentration of 15 mg⁄ml. Note the inverted "cup-shape" of the noncorrected projection profile (red) and scatter profiles (black). Since correction utilizing SPR (c and d) captured the noise component of the scatter signal, their application yielded a smoother scatter-corrected image. Figure adapted from [Puett 2018b].

### *4.2.2 The effect of scatter and noise correction through processing on sDBT image quality*

Experimentation for this dissertation investigated the effects of different scatter correction approaches on image quality. The different approaches handled noise processing differently, and as a result, their application produced images with different contrast, noise, and resolution. The direct scatter correction approach maintained good contrast but did not account for the noise component of the scatter. Scatter correction based on SPR did account for noise but compromised contrast. *f*SPR can be considered a blend of the direct and SPR scatter approaches and was designed to maximize the beneficial attributes of each [Wu 2017]. Indeed, in this study, scatter correction using *f*SPR yielded the highest observed values for the contrast-to-noise ratio (CNR) of the iodinated feature (Figure 4.5), when imaged using both temporal subtraction (TS) and dual energy subtraction (DES) protocols, which are the standard image collection protocols for contrasted breast imaging (see 3.5.1c Configuring the sDBT system for contrast-enhanced imaging).

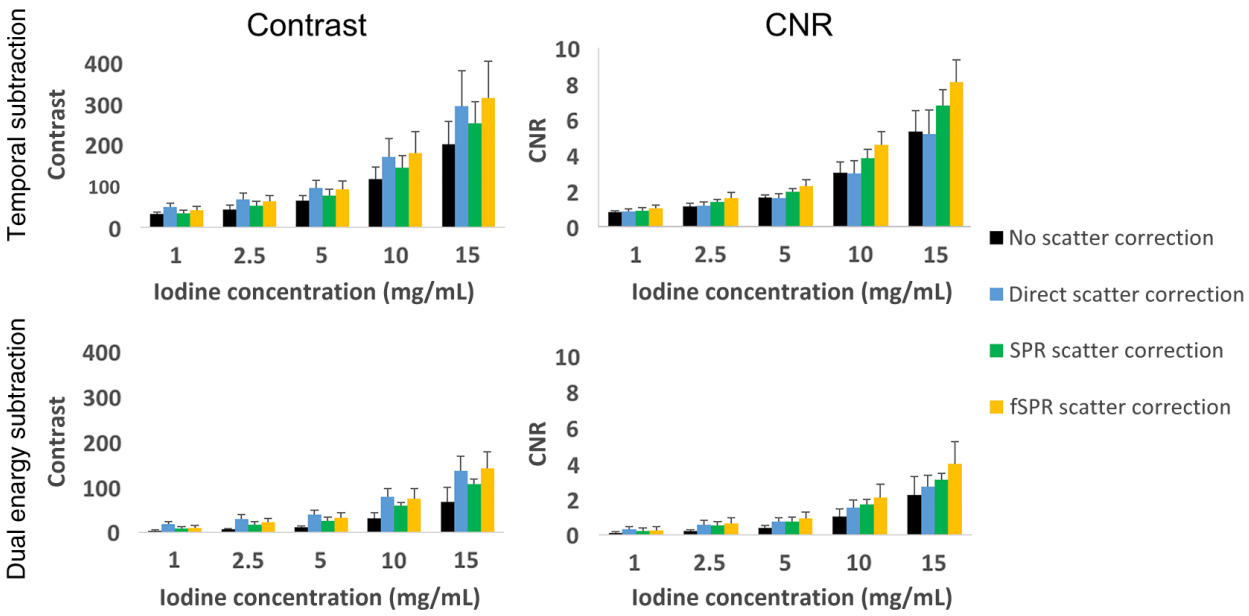


Figure 4. 5. The effect of applying different scatter correction algorithms on contrast and noise in *stationary* digital breast tomosynthesis (sDBT) images of breast-mimicking phantoms that had been customized with wells containing iodine to simulate contrast-enhanced imaging. Contrast and the contrast-to-noise ratio (CNR) were measured as a function of iodine concentration in slices from the reconstructed 3D image stack, which was generated from projection views collected using both temporal subtraction (TS) and dual energy subtraction (DES) protocols. Prior to reconstruction, different scatter correction algorithms were applied to the projection views, including a direct scatter correction (blue), correction utilizing the scatter-to-primary ratio (SPR) (green), or the application of a filtered SPR (*f*SPR) map (gold), resulting in images which could be compared to those produced with no scatter correction (black). Note that scatter correction by any method improved contrast. However, for both TS and DES, only the filtered scatter-to-primary (*f*SPR) correction approach produced a statistically significant increase in CNR ($p < 0.05$ by t-test) compared with no scatter correction for all iodine concentrations. Figure adapted from [Puett 2018b].

This increase in CNR using the *f*SPR approach also yielded images with the highest feature detectability (Figure 4.6), quantified using an index incorporating a task-based measure of image quality (3.6.1b Calculating detectability indices).

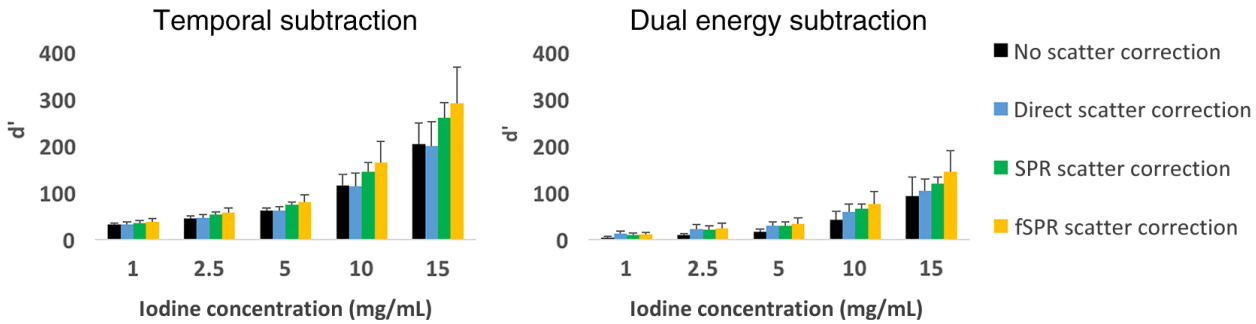


Figure 4. 6. The effect of applying different scatter correction algorithms on the detectability of contrasted sites in *stationary* digital breast tomosynthesis (sDBT) images of breast-mimicking phantoms that had been customized with wells containing iodine to simulate contrast-enhanced imaging. The detectability index (d') was measured as a function of iodine concentration in slices from the reconstructed 3D image stack, which was generated from projection views collected using both temporal subtraction (TS) and dual energy subtraction (DES) protocols. Prior to reconstruction, different scatter correction algorithms were applied to the projection views, including a direct scatter correction (blue), correction utilizing the scatter-to-primary ratio (SPR) (green), or the application of a filtered SPR (*f*SPR) map (gold), resulting in images which could be compared to those produced with no scatter correction (black). There was no loss in feature detectability with the application of any scatter correction approach. However, applying correction utilizing *f*SPR yielded images with the highest d'. Figure adapted from [Puett 2018b].

### *4.2.3 Artifact reduction in reconstructed and synthetic sDBT images*

The metal needles and wires used to localize breast lesions for biopsy can generate significant shadowing and rippling, which has been described as the "slinky" artifact, through the reconstructed image stack (Figure 2.8 and 4.7). However, the application of metal artifact reduction (MAR) (see 3.5.3c Reducing artifact) removed much of this artifact (Figure 4.7).

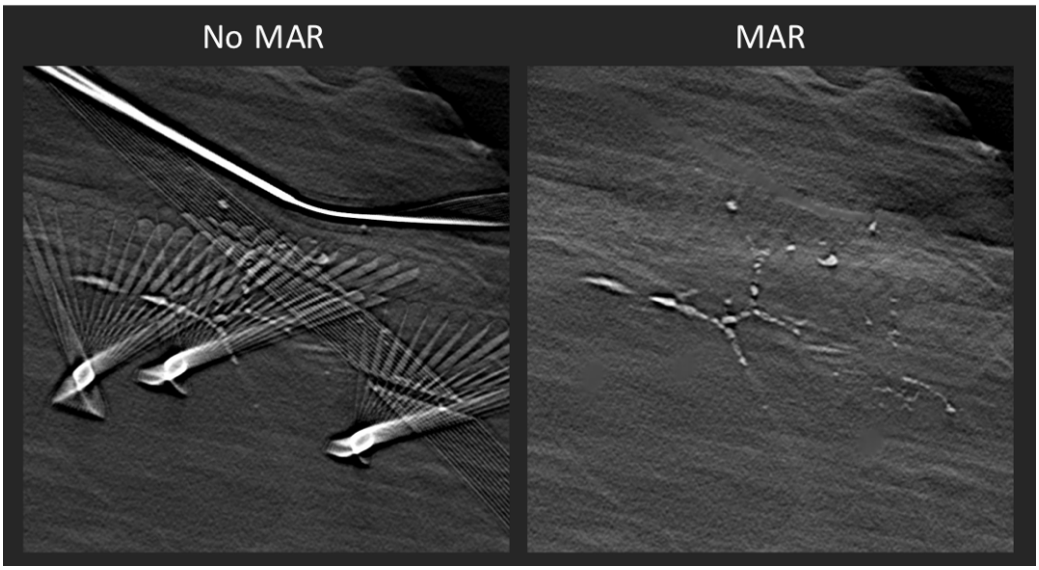


Figure 4. 7. Example images demonstrating the effect of incorporating a metal artifact reduction (MAR) algorithm on the appearance of a reconstructed image slice generated by *stationary* digital breast tomosynthesis (sDBT). The application of MAR (right) removed the "slinky" clutter of metal artifact that is otherwise present in the reconstructed image slice (left). Figure adapted from [Puett 2019a].

As has been reported in *synthetic* mammograms generated by conventional DBT [Geiser 2018], "slinky" artifacts were also present around dense calcifications and metal objects in *synthetic* images generated by sDBT (Figure 4.8). However, a two-step correction approach (see 3.5.3c Reducing artifact) involving segmentation at the projection image level followed by replacement of dense features back into the *synthetic* mammogram with histogram matching reduced these artifacts (Figure 4.8).

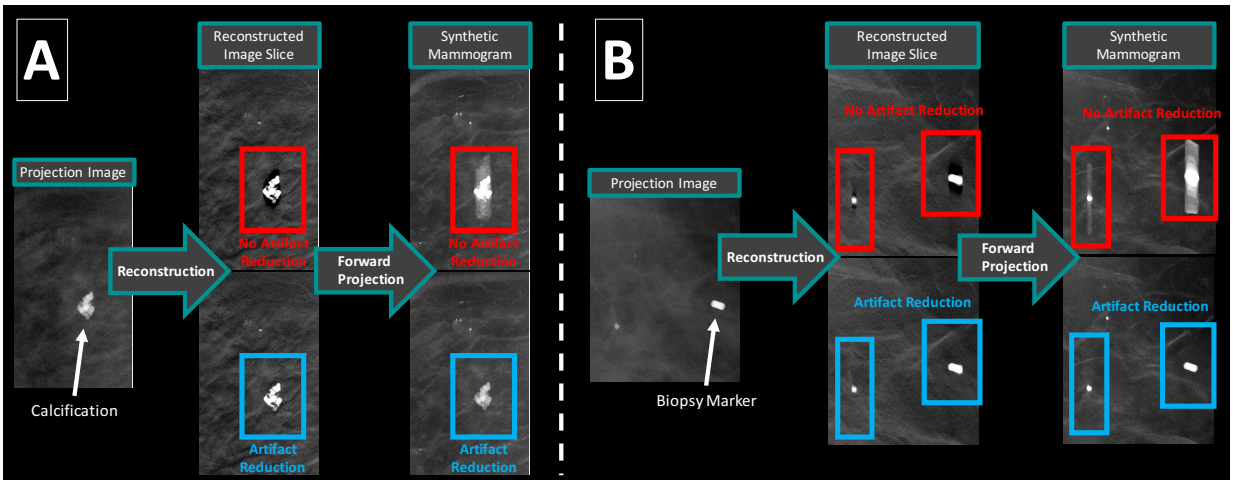


Figure 4. 8. Example images demonstrating the amplification of dense feature artifact in *synthetic* mammograms generated by *stationary* digital breast tomosynthesis (sDBT) as well as the value of artifact reduction through processing. The dense-feature artifacts surrounding a large calcification (A) and a metallic biopsy marker (B) include shadowing in the image slices of the reconstructed 3D image stack and rippling in the synthetic mammogram. However, a multi-step artifact reduction algorithm can minimize the artifact-related distortion in the final reconstructed and *synthetic* images displayed to the reader. Figure adapted from [Puett 2019b].

## 4.3 The performance of sDBT relative to standard 2D and conventional 3D mammography

### *4.3.1 Visualizing microcalcifications in lumpectomy specimens*

Microcalcification visibility was often assessed in this dissertation work for several reasons. First, microcalcification morphology and distribution provide important diagnostic clues in mammography, with smaller (<0.5 mm diameter), irregularly-shaped, and numerous, tightly-clustered calcifications being of most concern for malignancy [Henrot 2014]. Second, debate continues regarding the adequacy of microcalcification display by 3D mammography [Spangler 2011, Tagliafico 2014, Kopans 2011], leading to the common practice of combining 2D and 3D mammography. Third, microcalcification visibility reflects the resolution of a system, and thus, provides a clinically-applicable measure of performance by which the novel approach of sDBT can be compared to standard 2D mammography and conventional DBT. Lumpectomy specimens

provide attractive targets when measuring the performance of breast imaging systems, as pathology is always available for ground truth knowledge. This work included a comparison of microcalcification visibility in images generated by standard 2D mammography, conventional 3D mammography, and sDBT (see 3.6.1c Measuring microcalcification size) (Figure 4.9) [Puett 2019a]. Although characterizing individual microcalcifications is of value, as noted above, appreciating their association in clusters also provides important diagnostic clues. Since individual microcalcifications can be separated in different slices through the reconstructed image stack, clustering may be more difficult to detect when interpreting the 3D image stack produced by a DBT study compared to the standard mammogram [Spangler 2011]. As such, it is now common in clinical practice to present radiologists interpreting DBT scans with *synthetic* slab images (see 2.6 The image processing chain that generates sDBT images and the value of the *synthetic* mammogram). Slab images are generated by integrating the information from multiple slices in the reconstructed image stack into a single image (see 3.5.3e Forward projecting the 3D image space into *synthetic* mammograms), typically 1 cm in thickness. As such, when evaluating the appearance of microcalcification clusters in this study, readers were presented with standard 1 cm-thick slabs for viewing (Figure 4.9).

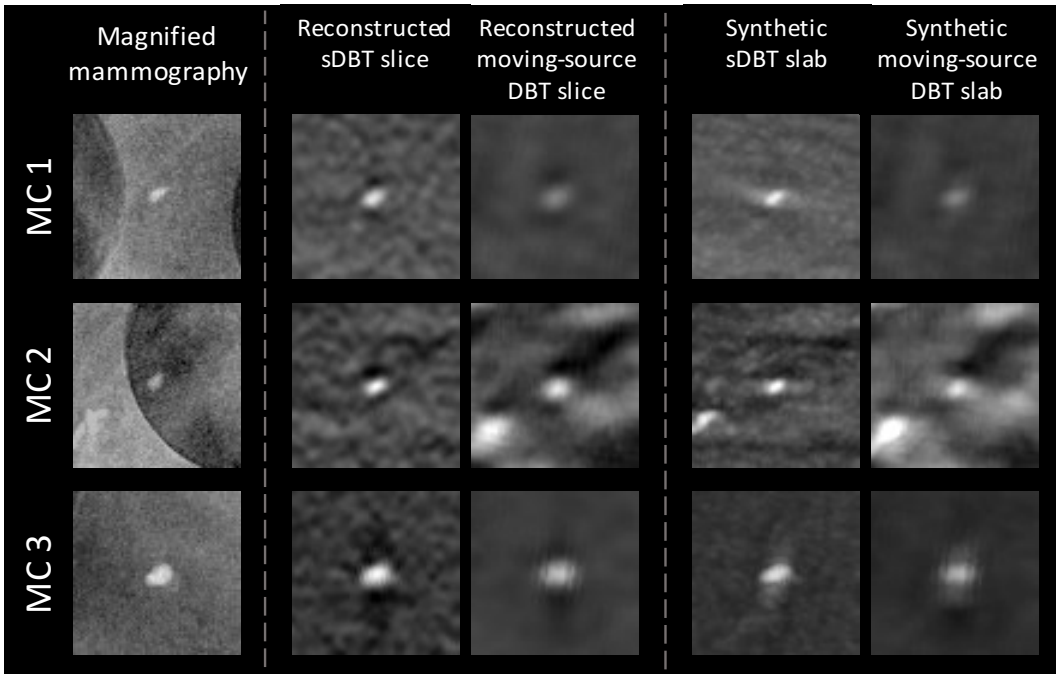


Figure 4. 9. The display of microcalcifications in images of lumpectomy specimens collected by magnified mammography, conventional digital breast tomosynthesis, and *stationary* digital breast tomosynthesis (sDBT). Note that the microcalcifications (MC 1-3) appear less blurred in the magnified mammography images compared to both the reconstructed image slices and *synthetic* slab mages generated by conventional moving-source DBT and sDBT, reflecting the higher spatial resolution of magnified mammography compared to the two DBT systems. However, the calcifications are better displayed by sDBT than conventional DBT. Finally, note the differences in the backgrounds surrounding each microcalcification. Fewer out-of-plane features are present in the reconstructed image slices from sDBT compared to moving-source DBT, reflecting a better depth resolution as a result of the wider angular span available with the sDBT system. Mammography has no depth resolution, and thus the background includes the supporting grid. Each image represents a cropped 5x5 mm area at 1.8x magnification. Figure adapted from [Puett 2019a].

The planar size of individual microcalcifications was similar in images generated by conventional DBT and sDBT when the sDBT projections were "binned" by post-processing, with the binned-detector mode being the default setting for the conventional DBT system used in these experiments (Figure 4.10A). However, the unique design of the sDBT system allowed for the collection of a wider-angle span of projection views and the operation of the detector in full-resolution mode without significantly prolonging the scan time. In this configuration, the planar sizes of individual microcalcifications displayed by sDBT were more similar to magnified

mammography than conventional DBT, a trend which was even more pronounced with decreasing microcalcification size (Figure 4.10B). This trend reflects the different spatial resolutions of each system (see 3.5.1a Differences in the breast-imaging systems). As the microcalcification size approaches the resolution the system, it appears blurred in the image. This blurring is a progressive change of increasing relative area but decreasing contrast, as microcalcifications of smaller and smaller size are displayed. Eventually, the contrast becomes too low to distinguish the microcalcification from its background, and therefore, it cannot be detected. With this in mind, Figure 4.10 demonstrated that sDBT, when operated in a full-resolution detector mode, displayed the smallest visible microcalcifications with less blur compared to conventional DBT, using magnified mammography as a reference.

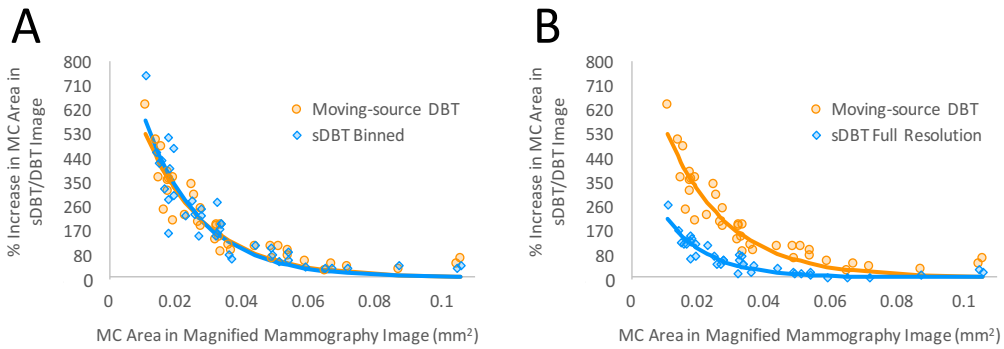


Figure 4. 10. Comparison of the size of individual microcalcifications as displayed in the in-focus reconstructed image slice generated by *stationary* digital breast tomosynthesis (sDBT) and conventional DBT. Size refers to the planar (x-y) area of the microcalcification (MC) as seen in a single image, referenced as a percentage to the size of the same microcalcification displayed by magnified mammography. As microcalcification size decreases and begins pushing the resolution of the system, the feature is blurred. Progressive blurring produces microcalcifications that appear larger but have a lower contrast. The planar sizes of individual microcalcifications were similar in images generated by moving-source DBT (orange circles) and sDBT (blue diamonds) when the sDBT projections were binned by post-processing, with the binned-detector mode being the default setting for the moving-source DBT system used in these experiments (A). However, when the sDBT system was operated in its optimum configuration, including the full-resolution detector mode, the size of every microcalcification was closer to that of magnified mammography than moving-source DBT (B), suggesting that the feature was displayed with less blur. Figure adapted from [Puett 2019a].

The artifact spread function (ASF) provides a quantitative measure of depth resolution (see 3.6.1c Measuring microcalcification size), and as expected, given the wider angular span of the distributed sDBT source array, for every microcalcification analyzed, sDBT yielded a narrower ASF in the reconstructed image stack compared to conventional DBT (Figure 4.11). This difference was statistically-significant ($p<0.001$) when compared at the mean full-width at half-maximum (FWHM) of the ASF for sDBT (2.1 mm) and conventional DBT (4.4 mm).

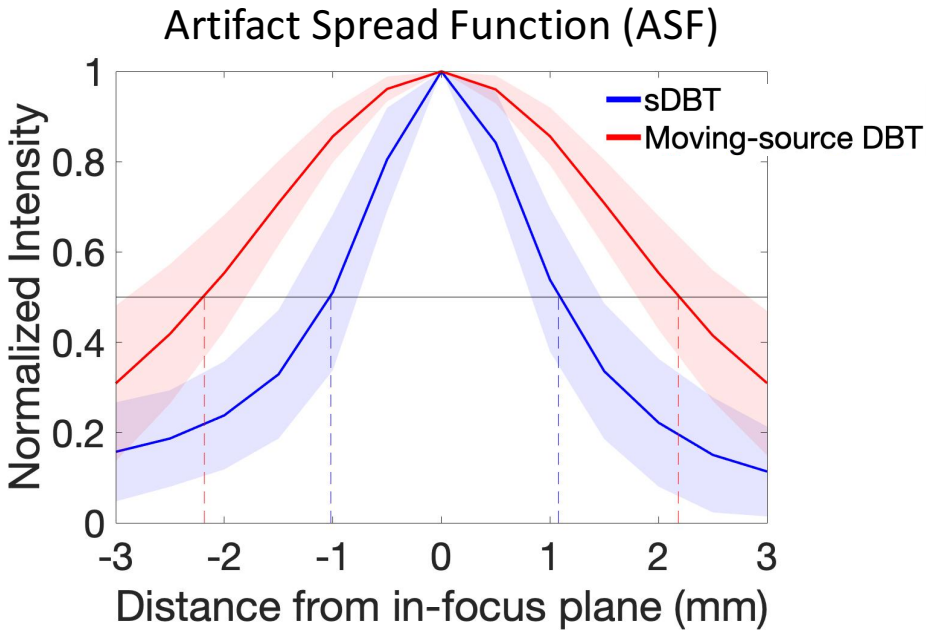


Figure 4. 11. Comparison of the depth resolution of *stationary* digital breast tomosynthesis (sDBT) and conventional DBT as reflected by the artifact spread function of individual microcalcifications in the reconstructed image stacks of lumpectomy specimens. The artifact spread function (ASF) provides a measure of size in the depth ($z$) direction and thus a reflection of depth resolution. The mean ASF (solid line) is narrower with sDBT (blue) compared to conventional DBT (blue). This difference is statistically-significant ($p<0.001$) when compared as the full-width at half-maximum (FWHM) (dashed lines). The shaded regions represent standard deviation about the mean. Figure adapted from [Puett 2019a].

The improved ASF provided by sDBT can also be appreciated in the reconstructed image slices shown in Figure 4.9, as more background structures are present in the reconstructed image slice from conventional DBT compared to sDBT, as a result of its smaller angular span.

In addition to comparing the display of individual microcalcifications in sDBT and conventional DBT, this study also compared the conspicuity of microcalcification clustering, again using magnified mammography as a reference (Figure 4.12).

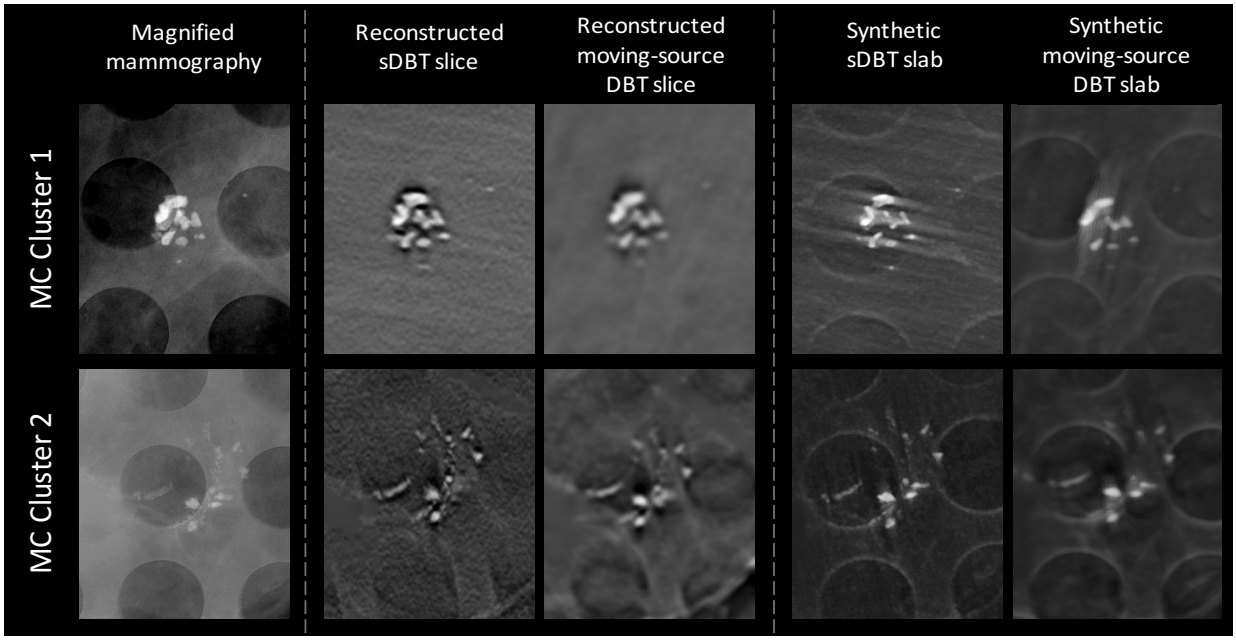


Figure 4. 12. Example images of two microcalcification clusters in lumpectomy specimens as displayed by magnified mammography, conventional digital breast tomosynthesis, and stationary digital breast tomosynthesis (sDBT). Both an in-focus reconstructed image slice and synthetic slab image are shown for the two DBT systems. The synthetic slab images were generated as a maximum intensity projection through 1 cm of the reconstructed image stack. Note that the microcalcifications (MC) appear less blurred in the magnified mammography images, reflecting the higher spatial resolution of this system compared to the two DBT systems. However, MC Cluster 1 and 2 are more clearly displayed in the images generated by sDBT compared to the conventional moving-source DBT system. Each image represents a cropped 21x17 mm area at 1.8x magnification. Figure adapted from [Puett 2019a].

However, unlike the individual microcalcification comparison, which was based on objective measures of microcalcification size, reader preference was used to assess the display of the microcalcification cluster (see 3.6.2 Assessing reader performance and preference). As noted

previously, synthetic slab images may display the spatial association of microcalcification clusters better than the reconstructed image stack (see 2.6 The image processing chain that generates sDBT images and the value of the synthetic mammogram and 3.5.3e Forward projecting the 3D image space into synthetic 2D mammograms), as individual microcalcifications can be separated in different slices through the 3D image stack. Therefore, for this preference study, readers were presented with synthetic slab images generated from information collected by sDBT and conventional DBT to compare to the magnified mammography image (Figure 4.12).

Two radiologists specializing in breast imaging were asked to rate either a strong preference, preference, weak preference, or similar preference when assessing microcalcification morphology, distribution/clustering, and size using a 7-point scale (-3 to +3) when viewing pairs of images: mammography image vs. sDBT slab, mammography image vs. conventional DBT slab, and sDBT slab vs. conventional DBT slab (Figure 4.13). All images were presented to the readers on MQSA-qualified 5-megapixel grayscale display monitors equipped with conventional DICOM viewing software tools. The order of individual images seen first and the order of image pairs was random. After viewing all of the image combinations for each case, the readers then ranked the three images as to their clinical usefulness, again using a 7-point scale. The responses provided data for statistical comparison, using a t-test to compare the paired datasets, with the findings reported as the mean and corresponding standard deviation. In every case, readers preferred the synthetic slab image generated by sDBT and the magnified mammography image over the conventional DBT slab image when characterizing the morphology of individual microcalcifications and identifying small microcalcifications. Also, the synthetic slab image generated by sDBT and the magnified mammography image were preferred over the

conventional DBT slab image when assessing microcalcification clusters in most cases (Figure 4.13A and B). On average, readers also tended to prefer the magnified mammography image over the sDBT slab image. However, this preference was less consistent, with the sDBT slab image equal to or preferred over magnified mammography in 50% of cases (Figure 4.13C).

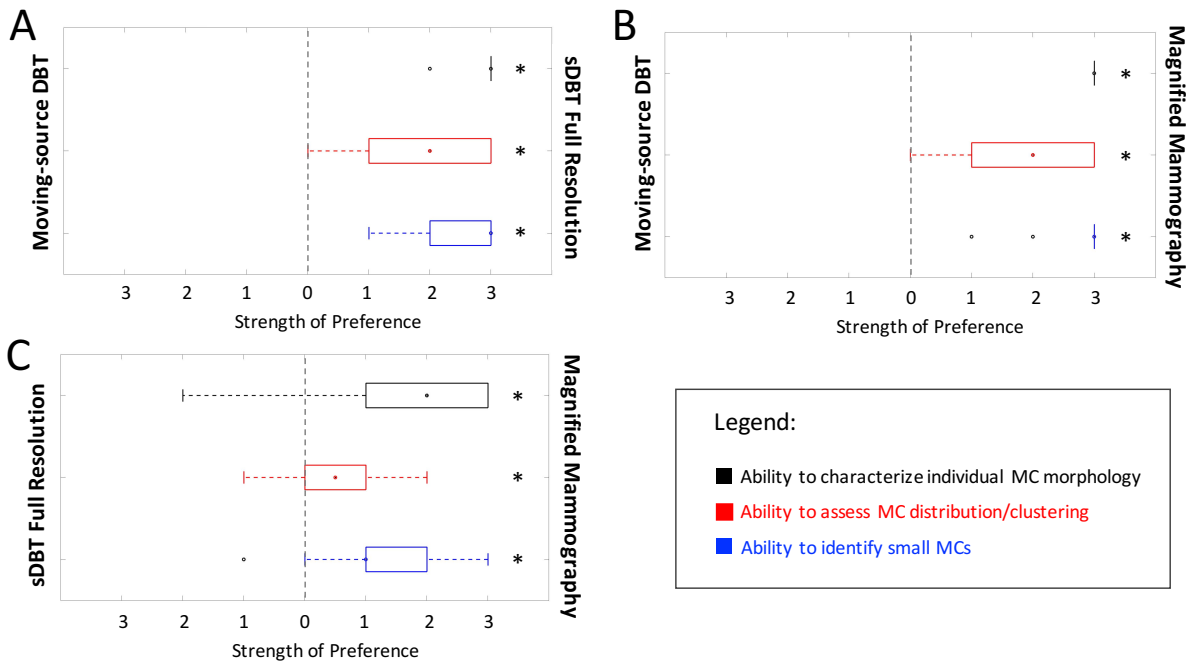


Figure 4. 13. Reader preferences when comparing the display of microcalcifications in the magnified mammography images of lumpectomy specimens and *synthetic* slab images generated by conventional digital breast tomosynthesis and *stationary* digital breast tomosynthesis (sDBT). Readers were asked to rate their preference when characterizing individual microcalcifications (MC) morphology (black), assessing microcalcification distribution/clustering (red), and identifying small microcalcifications (blue) as they viewed paired images: the *synthetic* slab image generated by sDBT vs. the *synthetic* slab image generated by conventional moving-source DBT (A), the magnified mammography image vs. the *synthetic* moving-source DBT slab image (B), and the magnified mammography image vs. the *synthetic* slab image generated by sDBT (C). The target dot represents the median preference score, the box represents the interquartile range, and the black circles represent outliers. * indicates a statistically-significant preference ($p<0.05$). Figure adapted from [Puett 2019a].

In terms of characterizing the overall diagnostic value or "clinical usefulness" of the magnified mammography image, the sDBT *synthetic* slab image, and the conventional DBT *synthetic* slab image, as related to microcalcification visibility, readers strongly preferred sDBT

and magnified mammography over conventional DBT ($p<0.05$), although on average, magnified mammography was preferred over sDBT ($p<0.05$).

### *4.3.2 Experience with sDBT in human studies*

*4.3.2a Reader accuracy*

When assessing the performance of new imaging technologies at the clinical level, detailed reader studies are used to measure diagnostic accuracy, agreement, confidence, and preference (see 3.6.2 Assessing reader performance and preference). This dissertation work included a reader study comparing sDBT to standard 2D mammography in a BIRADS 4 cohort (see 3.4.3 Patient selection for reader study). Performance can be appreciated by analyzing receiver operating characteristic (ROC) curves (Figures 4.14A-C). The area under the ROC curve (AUC) provides a measure of diagnostic accuracy and was calculated for each reader and each modality using a mixed-effect model (Figure 4.14D). In this study, three of the four readers performed better using sDBT. Only Reader 2 performed better using mammography and interestingly had the most experience with mammography at 25 years. Reader 4 had the least experience with sDBT and demonstrated a performance that differed the most from the other readers when interpreting sDBT images (Figure 4.14B), as reflected by the unique ROC curve shape. Overall, the mean AUC for sDBT was significantly ($p<0.0001$) higher than the mean AUC for mammography (Figure 4.14C), demonstrating that on average, readers were more likely to identify malignancy correctly when interpreting the sDBT images compared to standard 2D mammography.

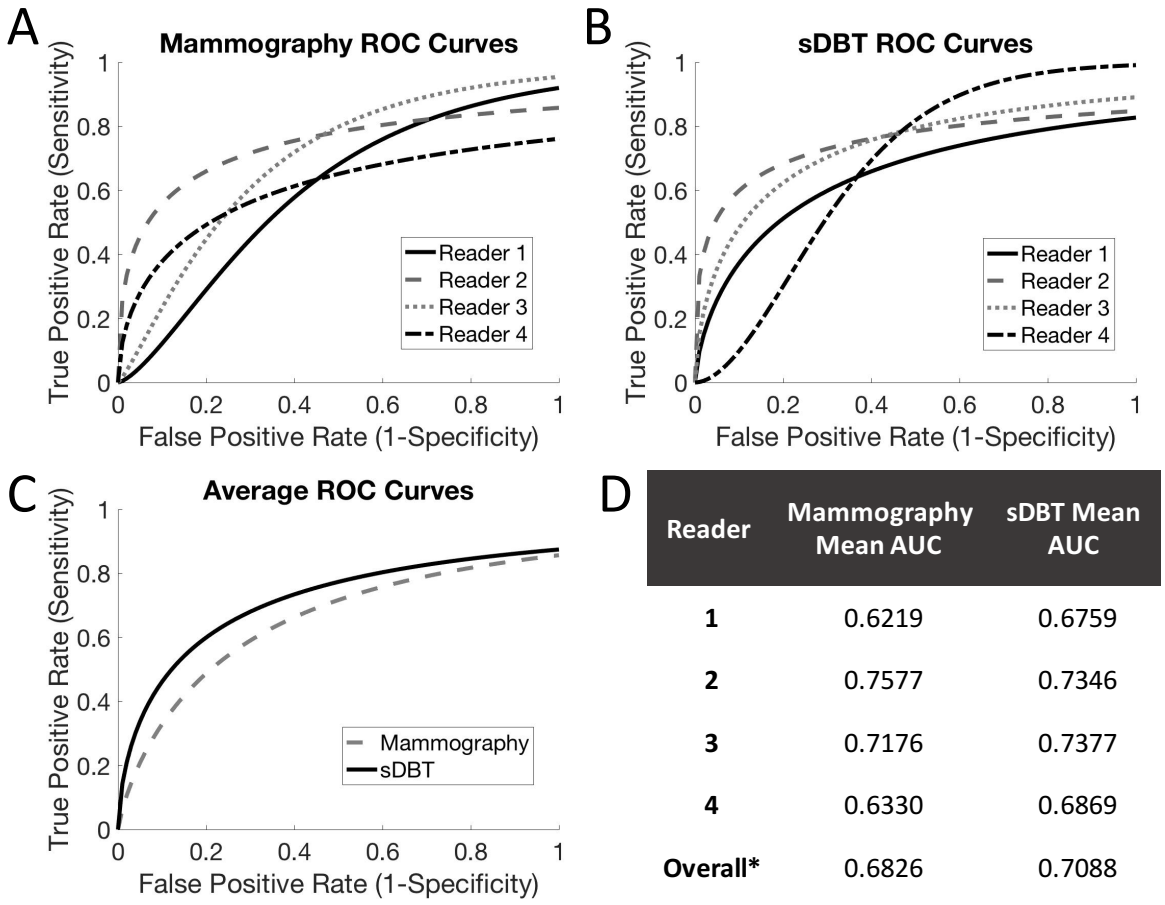


D

| Reader | Mammography Mean AUC | sDBT Mean AUC |
|---|---|---|
| **1** | 0.6219 | 0.6759 |
| **2** | 0.7577 | 0.7346 |
| **3** | 0.7176 | 0.7377 |
| **4** | 0.6330 | 0.6869 |
| **Overall*** | 0.6826 | 0.7088 |

Figure 4. 14. A comparison of reader performance when interpreting standard mammograms and the reconstructed image stack generated by *stationary* digital breast tomosynthesis (sDBT) from patients with concerning breast lesions. Performance was assessed by generating receiver operating characteristic (ROC) curves for each reader when interpreting mammograms (A) and the sDBT images (B). Sensitivity and specificity were calculated from the reported likelihood of malignancy at the time of interpretation and the actual presence of malignancy as determined by biopsy. The area under the ROC curve (AUC) provided a measure of diagnostic accuracy, and the mean AUC for sDBT was significantly higher than the mean AUC for mammography (C). AUCs were also calculated for each reader and each modality using a mixed-effect model (D). * represents $p<0.0001$. Figure adapted from [Lee 2019].

The higher diagnostic accuracy using sDBT held true for each breast density category (BIRADS A-D) [Sickles 2013] and breast thickness range, as reflected by statistically higher ($p<0.05$) mean AUCs for sDBT compared to mammography (Figure 4.15), with the breast thickness ranges selected to ensure an adequate number of samples within each interval for statistical analysis.

A

| BIRADS Breast Density | Mammography Mean AUC | sDBT Mean AUC | p-value |
|---|---|---|---|
| **A** | 0.6831 | 0.7156 | 0.0030 |
| **B** | 0.6811 | 0.7106 | < 0.0001 |
| **C** | 0.6858 | 0.7007 | 0.0120 |
| **D** | 0.6777 | 0.7126 | < 0.0001 |

B

| Compressed Breast Thickness (cm) | Mammography Mean AUC | sDBT Mean AUC | p-value |
|---|---|---|---|
| ≤ **3.4** | 0.6883 | 0.7145 | 0.001 |
| **3.5 – 4.4** | 0.6765 | 0.7064 | < 0.0001 |
| **4.5 – 5.4** | 0.6890 | 0.7129 | < 0.0001 |
| ≥ **5.5** | 0.6801 | 0.7025 | 0.006 |

Figure 4. 15. Average reader performance as a function of breast density and compressed breast thickness when interpreting standard mammograms and the reconstructed image stack generated by *stationary* digital breast tomosynthesis (sDBT) from patients with concerning breast lesions. The area under the receiver operator characteristic curve (AUC) provided a measure of diagnostic accuracy. Readers were more likely to make a correct diagnosis using stationary digital breast tomosynthesis (sDBT) compared to mammography for each breast density (A) category (BIRADS A-D) and breast thickness range (B), as reflected by statistically higher ($p<0.05$) mean AUCs. Figure adapted from [Lee 2019].

*4.3.2b Reader agreement and confidence*

Using a likelihood of malignancy threshold of 0.5, the overall agreement between readers for the presence of malignancy was fair ($\kappa = 0.35$) with mammography and slight ($\kappa = 0.18$) with sDBT. Increasing the likelihood of malignancy threshold to 0.8 resulted in moderate agreement ($\kappa = 0.59$) between readers when using mammography and substantial agreement ($\kappa = 0.67$) between readers when using sDBT.

On average, readers had similar confidence in their interpretation of the mammograms and sDBT images (Figure 4.16A). Although the readers were not given any clinical information and were unaware of the biopsy results, they were significantly more confident ($p<0.05$) in their final impression when interpreting images that actually contained malignant lesions compared to their final impression when interpreting images that were determined to be benign by biopsy (Figure 4.16B). This higher confidence when viewing images of malignant as opposed to benign lesions was similar for both mammography and sDBT.

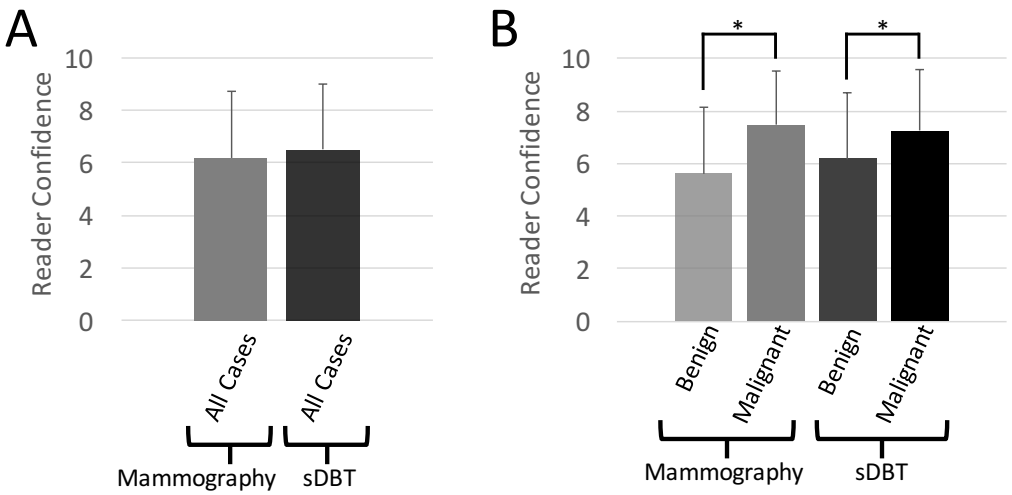


Figure 4. 16. Reader confidence when interpreting standard mammograms and the reconstructed image stack generated by *stationary* digital breast tomosynthesis (sDBT) from patients with concerning breast lesions. Reader confidence in the overall impression when interpreting mammograms (gray) and sDBT images (black) was similar when averaged for all cases (A). However, readers were significantly more confident in their interpretation of images that contained malignant lesions compared to their interpretation of images with benign lesions, with pathology providing diagnostic ground-truth ($p<0.05$, with error bars representing the standard deviation of each group). This finding was similar for both mammography and sDBT (B). Figure adapted from [Lee 2019].

*4.3.2c Reader preference when interpreting image features*

Figure 4.17 summarizes reader preference when using sDBT and mammography to interpret diagnostically-important image features. As reflected by average preference scores greater than zero, readers preferred sDBT over mammography when interpreting soft-tissue features (Figure 4.17), including mass shape and margins, architectural distortion, and asymmetry ($p<0.05$ in all cases). However, mammography was preferred over sDBT when characterizing microcalcifications ($p<0.05$).

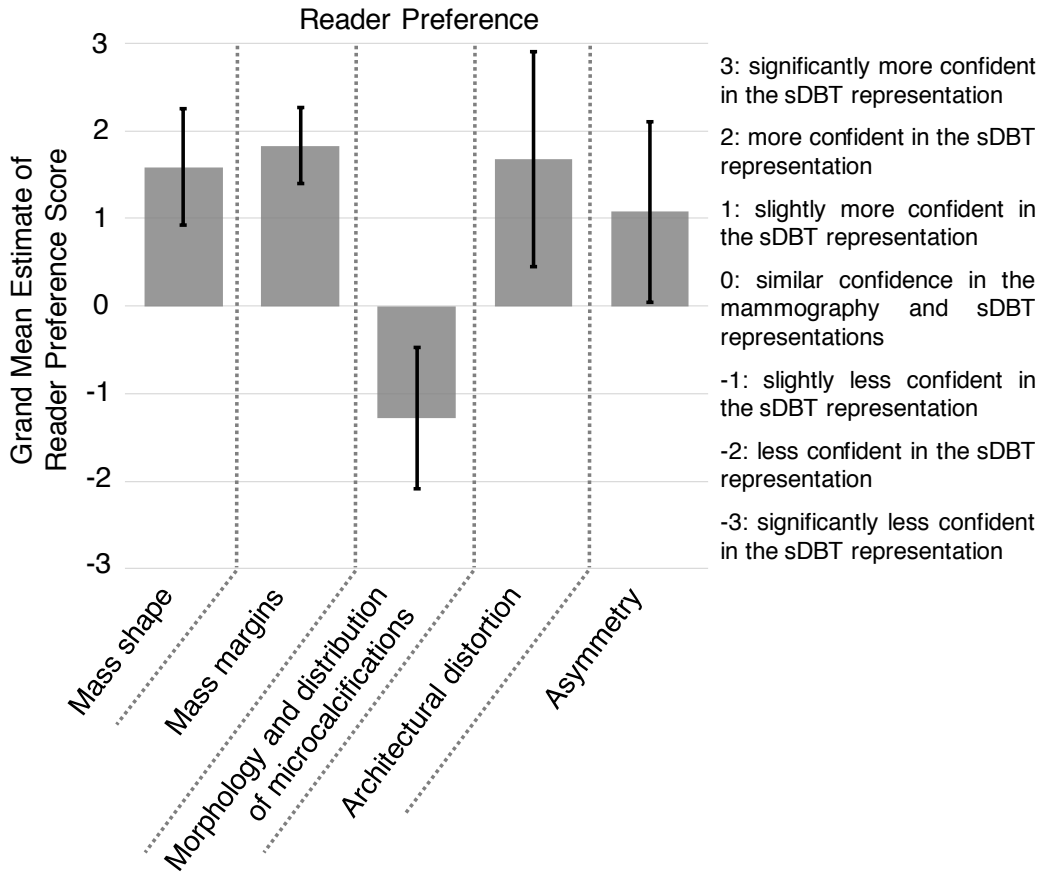


Figure 4. 17. Reader preference when interpreting diagnostically-important image features as displayed in the standard mammograms and the reconstructed image stack generated by *stationary* digital breast tomosynthesis (sDBT) from patients with concerning breast lesions. The bar graphs summarize aggregate reader preference and show that readers preferred the reconstructed sDBT image stack over the mammogram when interpreting soft-tissue features (mass margins and shape, architectural distortion, and asymmetry) but preferred mammography when characterizing microcalcifications ($p<0.05$ in all cases, with error bars representing the 95% confidence interval of each grand mean estimate). Positive scores represent a preference for sDBT, and negative scores represent a preference for mammography. Figure adapted from [Lee 2019].

Example images are helpful in demonstrating differences between the standard mammogram and an sDBT image (Figure 4.18).

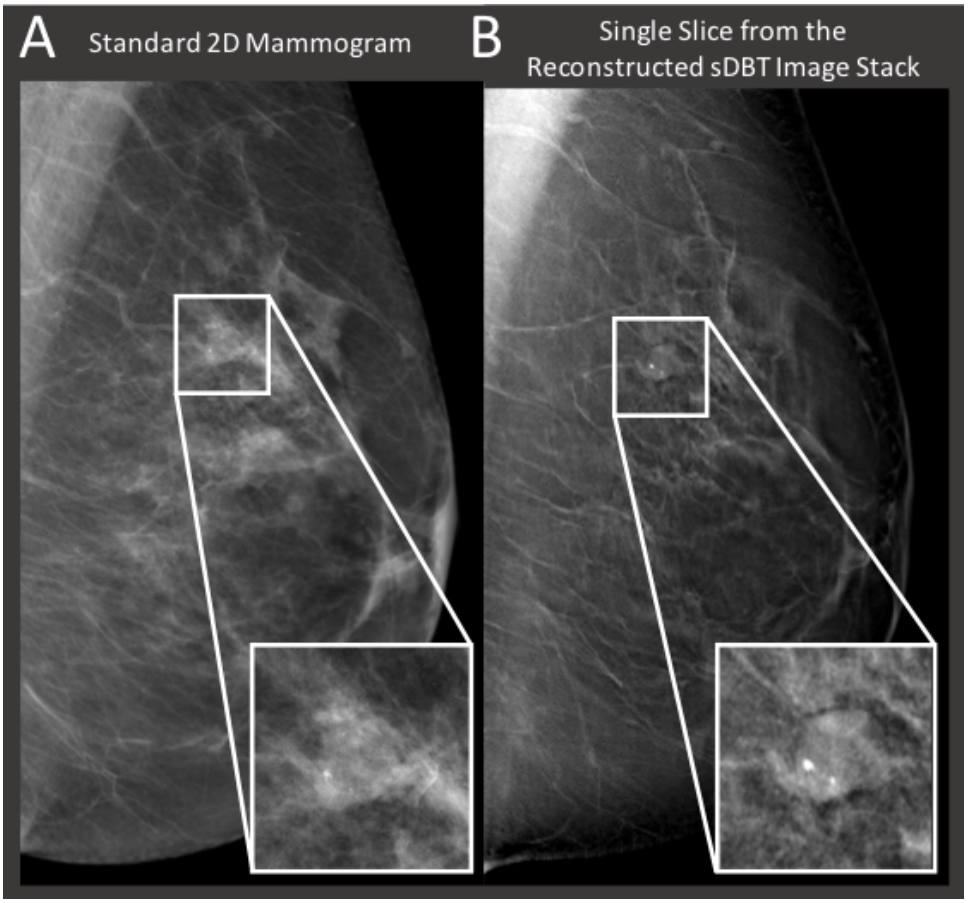


Figure 4. 18. Example images comparing the standard mammogram and to an image slice from the reconstructed *stationary* digital breast tomosynthesis (sDBT) stack. Based on pathology, the site of concern (expanded view) was benign. Readers were more likely to characterize this lesion accurately and were more confident in their assessment when interpreting sDBT (B), given the fact that the margins of the mass were more difficult to characterize on the mammogram (A). For this example, readers scored an average likelihood of malignancy of 50% when interpreting the mammogram and 25% when interpreting the sDBT images. Figure adapted from [Lee 2019].

## 4.4 Incorporating synthetic mammography into sDBT

### *4.4.1 Feature detectability in the synthetic mammogram as a function of intensity weighting during forward projection*

Quantifying detectability (d') (see 3.6.1b Calculating detectability indices) allowed correlation between the visibility of clinically-important image features in the *synthetic* mammogram and the order of the polynomial weighting function used during forward projection (see 3.5.3e Forward projecting the 3D image space into *synthetic* 2D images). The range of

weighted functions exists between the extremes of an average-intensity projection (zero-order) and maximum-intensity projection (infinite-order). As expected, larger calcifications tend to be more visible than smaller calcifications, regardless of weighting or the thickness of the breast (Figure 4.19A). However, for microcalcifications of a given size, increasing the weighting function, at least up to a point, improved their detectability (Figure 4.19B).

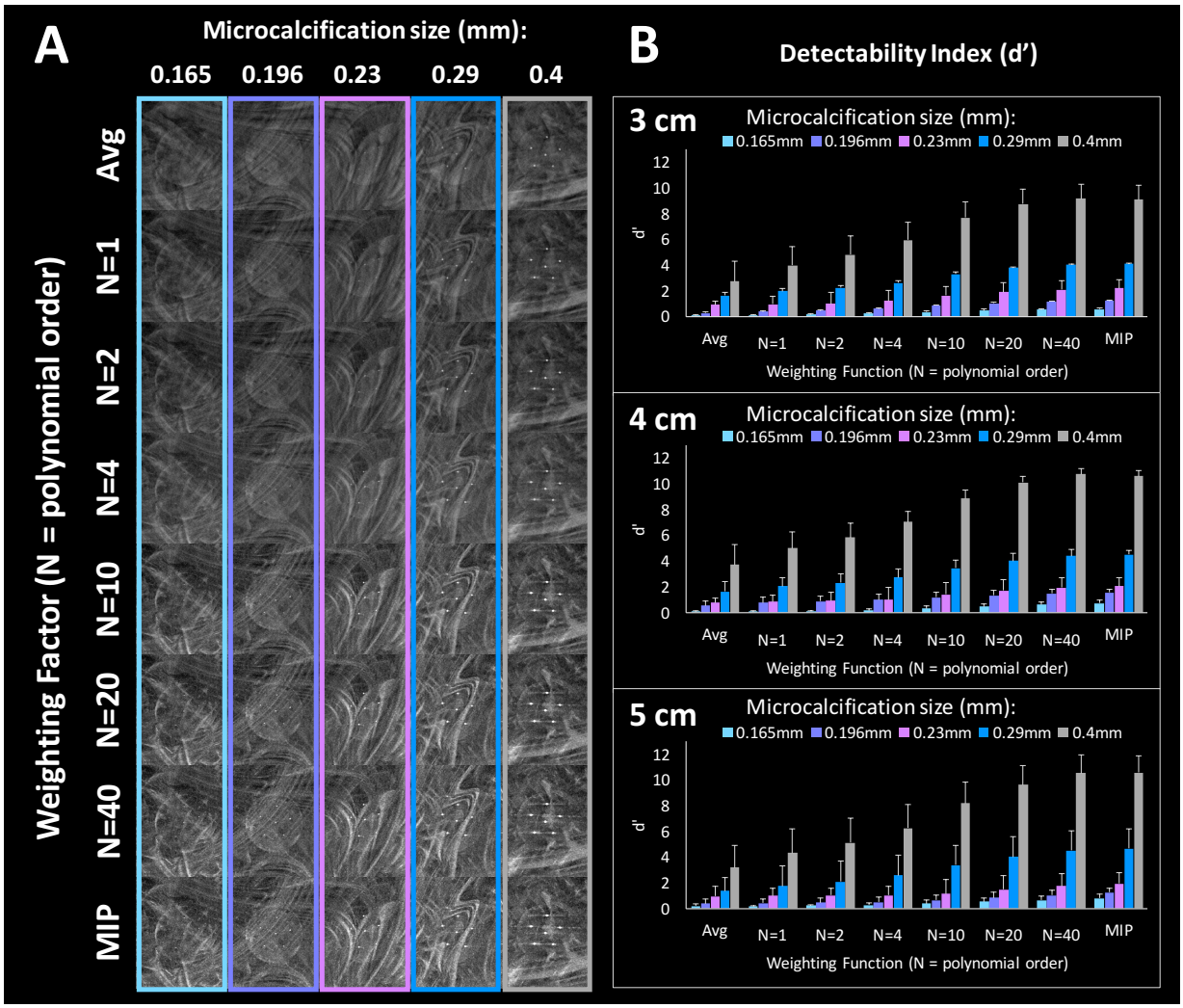


Figure 4. 19. Relationships between microcalcification visibility in *synthetic* images generated by *stationary* digital breast tomosynthesis (sDBT) as a function of the polynomial order used to weight the forward projection. In this case, microcalcification mimics of various sizes (A) were present in breast phantoms ranging between 3-5 cm in thickness, and visibility was quantified by a detectability index (d') (B). There was a positive correlation between the detectability of the microcalcification and the weighting factor order, regardless of the size of the microcalcification or the thickness of the breast. Figure adapted from [Puett 2019b].

The relationship between d' and the weighting factor applied during forward projection was less consistent for masses, compared to microcalcifications, given the fact that masses differ significantly in their inherent properties. Figure 4.20 demonstrates how different the relationship between d' and the weighting factor can be, when calculated for 3 masses of similar size (5 mm) but different density (Figure 4.20B). However, in general, masses do tend to be lower-density features, and as such, their detectability tended to be higher in *synthetic* mammograms generated using lower-order weighting (Figure 4.20).

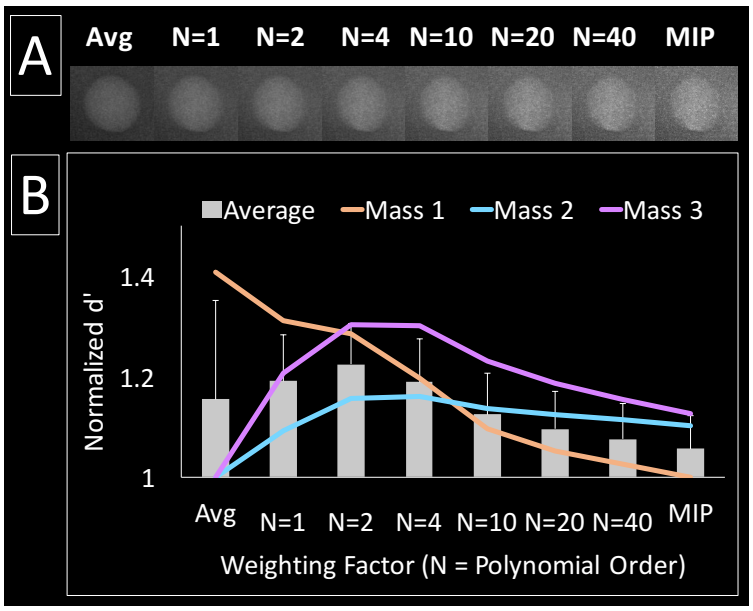


Figure 4. 20. Relationships between the visibility of masses in *synthetic* images generated by *stationary* digital breast tomosynthesis (sDBT) as a function of the polynomial order used to weight the forward projection. In these examples, the mass mimics were present in breast phantoms and differed in density. Visibility was quantified by a detectability index (d'). Note the varied relationship between mass visibility and the order of weighting (B-line graph) but also the fact that visibility tended to be higher when lower order weights were used (A and B-bar graph). Figure adapted from [Puett 2019b].

Differences in the information displayed by low and high-ordered weighting during forward projection could be appreciated at the clinical level when applied to patient images. Figure 4.21 displays sDBT-generated low and high-order weighted *synthetic* mammograms next to the standard mammogram obtained on a patient who had been "called back" for further

evaluation of concerning microcalcifications noted on screening mammography. Comparing line profiles drawn through a single microcalcification demonstrated the signal intensity to be highest when the microcalcification was displayed in the *synthetic* mammogram generated by high-order weighting compared to both the *synthetic* mammogram generated by low-order weighting and to the actual mammogram.

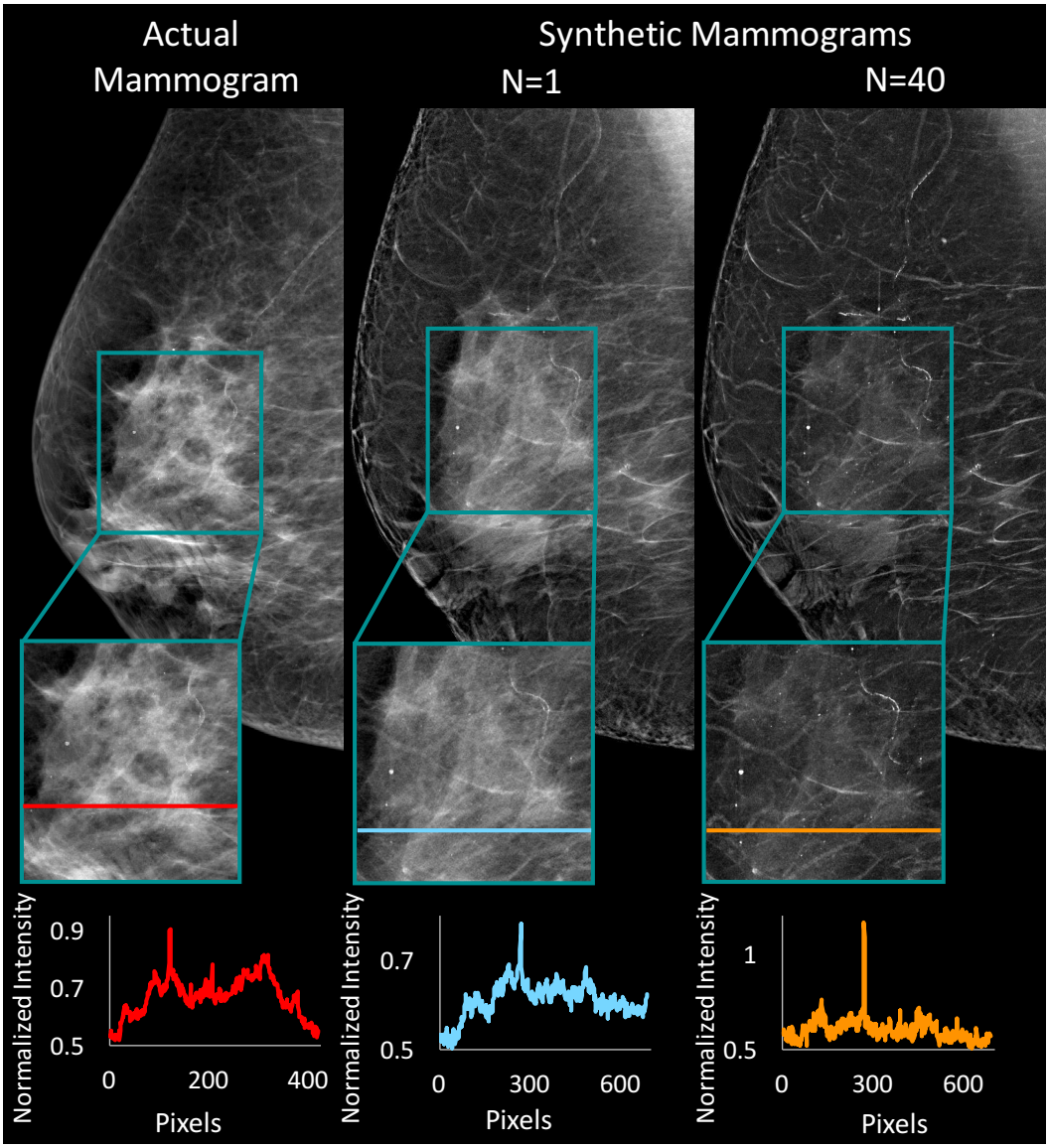


Figure 4. 21. A comparison of pixel intensities in the actual mammogram and *synthetic* mammograms generated from information collected by *stationary* digital breast tomosynthesis (sDBT). The *synthetic* mammograms were generated using a polynomial weighting function of order N=1 (center) and N=40 (right). Line profiles are drawn through the same

microcalcification for each image. The background pattern is different between the actual mammogram and sDBT-generated *synthetic* mammograms, since the two studies were done at different times and thus imaged different compressions. Figure adapted from [Puett 2019b].

Similarly, when assessed on eight individual microcalcifications visible in all three images, microcalcification contrast was significantly greater in the high-order weighted synthetic mammogram compared to the other images (Figure 4.22). This qualification of comparing only the microcalcifications visible in all three images is important, since it emphasizes the point that this study was not designed to assess relative differences in the visibility of all microcalcifications or their clustering. As such, the findings cannot be used to compare the clinical value of the two different imaging modalities - standard mammography and sDBT. Nevertheless, the findings were helpful in guiding continued work to optimize the forward projection algorithms that generate the *synthetic* mammograms.

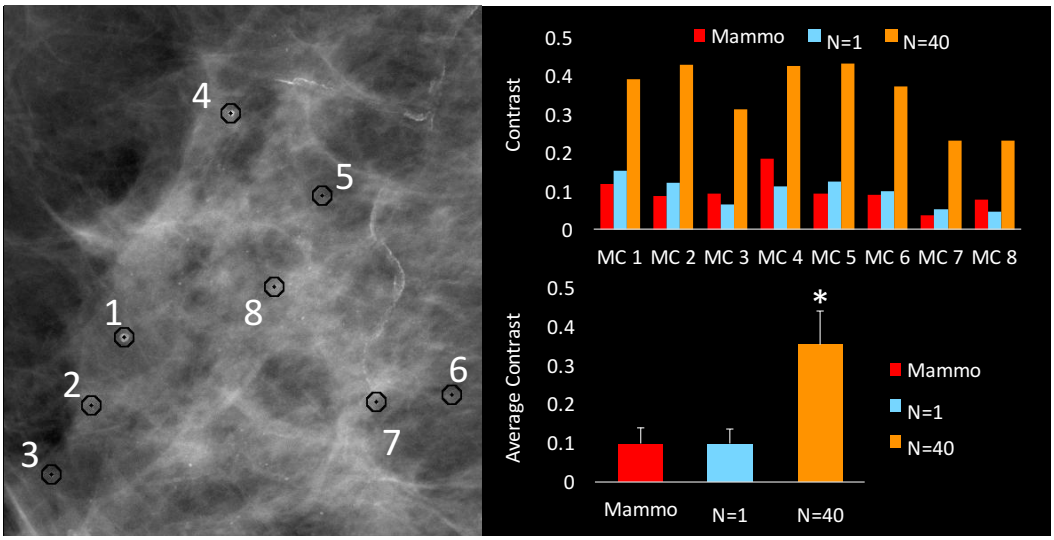


Figure 4. 22. A comparison of microcalcification contrast in the actual mammogram and *synthetic* mammograms generated from information collected by *stationary* digital breast tomosynthesis (sDBT). Eight microcalcifications visible in the actual mammogram (red bars) and two *synthetic* mammograms generated by sDBT, including a *synthetic* mammogram generated with a polynomial weighting function of order N=1 (blue bars) and a *synthetic* mammogram generated with a polynomial weighting function of order N=40 (orange bars), were used for comparison. The average microcalcification contrast in the *synthetic* mammogram generated using a high-order weighting (N=40) was significantly higher than the actual

mammogram and *synthetic* mammogram of order N=1 (* indicates $p<0.05$ by Student's t-test). Figure adapted from [Puett 2019b].

### *4.4.2 Phantom-based testing of a forward projection approach incorporating feature enhancement*

Forward projection refers to the steps in the image processing chain that integrate the information contained in the reconstructed image slices of the 3D image stack into 2D *synthetic* images (see 2.6 The image processing chain that generates sDBT images and the value of the *synthetic* mammogram, 3.5.3a The image processing chain for sDBT in context, and 3.5.3e Forward projecting the 3D image space into *synthetic* 2D mammograms). An understanding of the relationships between weighted forward projection and the visibility of features-of-concern provided a foundation for incorporating feature enhancement into the multistep process that generated the final *synthetic* images (see 4.4.1 Feature detectability in the *synthetic* mammogram as a function of intensity weighting during forward projection). This multistep process involved combining Laplacian decomposition, MSER-based feature identification, feature weighting through depth, and weighted recombinations of the resulting frequency-sorted and feature-weighted image slices. The processing chain culminated in a set of *synthetic* images, including a standard *synthetic* mammogram and two pathology-enhanced synthetic mammograms, one dedicated to the display of microcalcifications and the other to the display of masses (see 3.5.3e Forward projecting the 3D image space into *synthetic* 2D mammograms). Phantom-based image quality assessments (see 3.6.1a Quantifying signal and noise) were used to evaluate the performance of the feature-enhancement approach.

First, the appearance of mass and microcalcification mimics present in the ACR phantom (see 3.4.1 Breast-mimicking phantoms and 3.6.1 Measuring image quality and quantifying feature detectability) were asssessed. Standard, mass-enhanced, and microcalcification-enhanced

sDBT *synthetic* images of the ACR phantom were generated and compared to the processed FFDM image and *synthetic* image generated by conventional DBT (Figure 4.23).

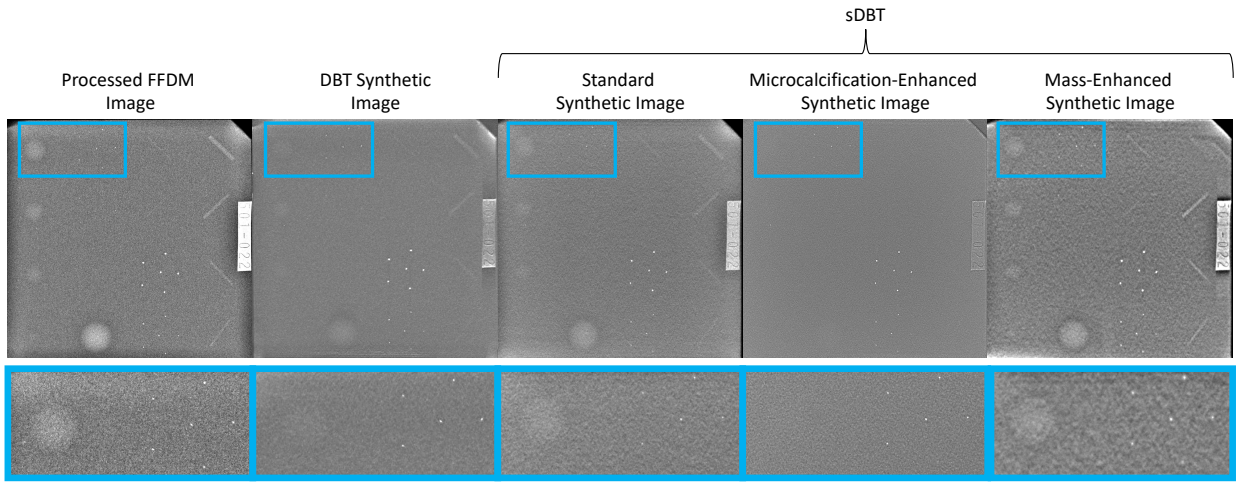


Figure 4. 23. Representative images of the American College of Radiology mammography accreditation phantom, allowing a comparison of the appearance of features in the mammogram and *synthetic* images generated by conventional digital breast tomosynthesis (DBT) and stationary digital breast tomosynthesis (sDBT). From left to right, these examples include a processed full field digital mammography (FFDM) image, a *synthetic* image generated by conventional digital breast tomosynthesis, a standard *synthetic* image generated by sDBT, and sDBT pathology-enhanced *synthetic* images. Figure adapted from [Puett 2020a].

Contrast, CNR, and the FWHM were measured in these images for the three largest microcalcification clusters (Figure 4.24A-C), since only these clusters were displayed consistently in images generated by all three modalities. Qualitatively, the next smallest cluster of microcalcifications was more visible in the FFDM image compared to both the conventional DBT and sDBT synthetic images. For the three clusters analyzed, microcalcification CNRs in both the conventional DBT *synthetic* image and the microcalcification-enhanced sDBT *synthetic* image were significantly higher than the microcalcification CNR in the FFDM image (Figure 4.24B). Additionally, the microcalcification FWHM was smallest in the microcalcification-enhanced sDBT *synthetic* image (Figure 4.24C), demonstrating that the microcalcifications were displayed with less blur (see 3.6.1c Measuring microcalcification size). Of note, the FWHM of

the microcalcification signal was greatest in the mass-enhanced sDBT *synthetic* image, emphasizing the significant impact of processing on the display of diagnostically-important features in the mammogram and the potential value of utilizing different processing approaches to generate different *synthetic* mammograms dedicated to either masses or microcalcifications.

Contrast and CNR for the five mass mimics present in the ACR phantom were compared in the FFDM image and the conventional DBT and sDBT *synthetic* images (Figures 4.24D and E). The smallest masses (numbers 4 and 5) had the highest contrast and CNR in the mass-enhanced sDBT synthetic image compared to the FFDM and conventional DBT *synthetic* images. Also, the mass-enhanced *synthetic* sDBT images had higher mass contrast and CNR than the standard and microcalcification-enhanced sDBT *synthetic* images, again suggesting value to providing a *synthetic* image dedicated to displaying soft-tissue features.

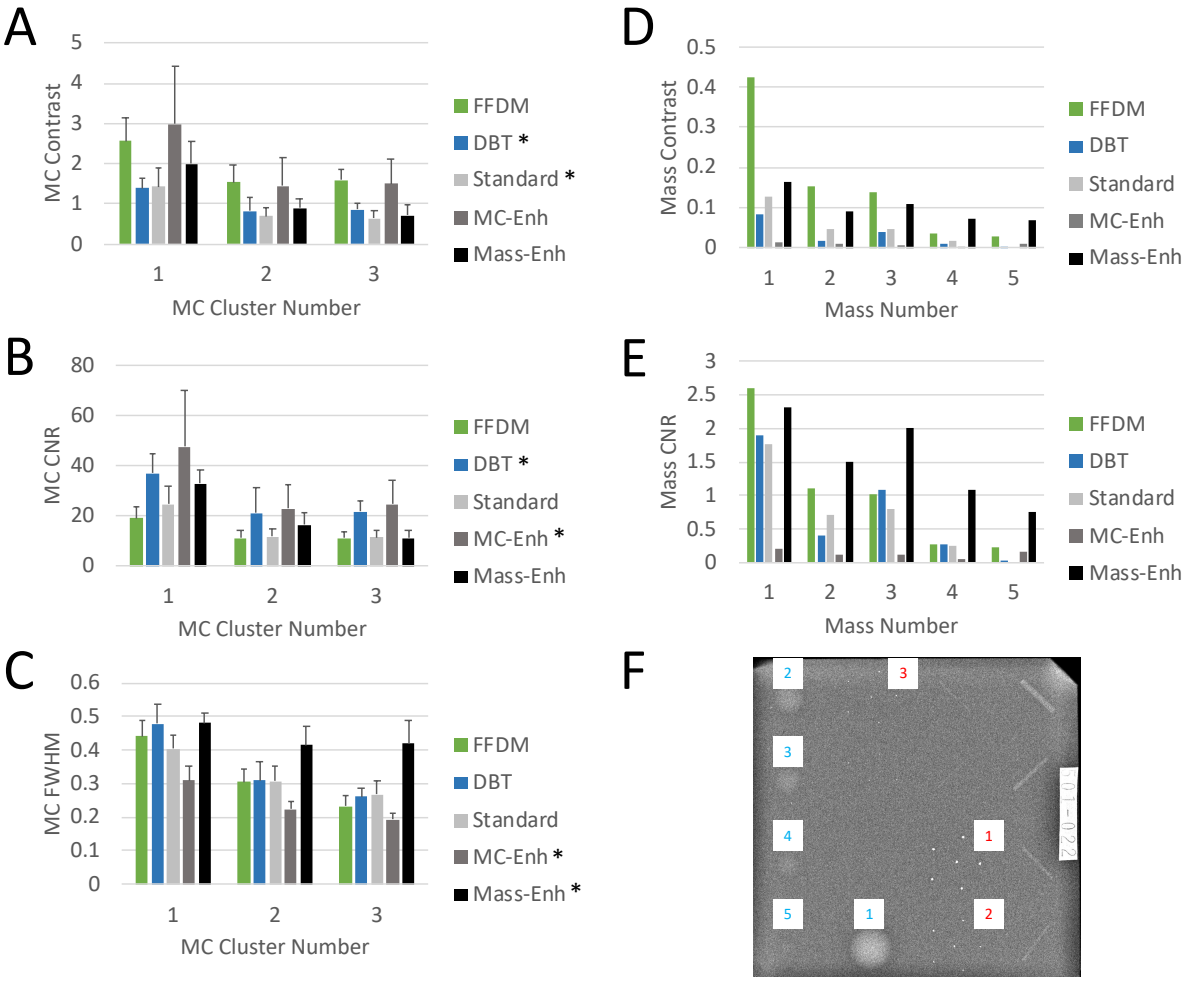


Figure 4. 24. Image quality measurements in the processed full field digital mammography (FFDM) image and *synthetic* images generated by conventional digital breast tomosynthesis (DBT) and *stationary* digital breast tomosynthesis (sDBT) of the American College of Radiology mammography accreditation phantom (ACR Phantom). For sDBT, standard, microcalcification-enhanced (MC-enh), and mass-enhanced (mass-enh) *synthetic* images were available for comparison. Since each microcalcification (MC) cluster contained 5 mimics, statistical analysis could be peformed during the comparison of MC contrast (A), CNR (B), and FWHM (C). * represents a statistically significant difference ($p<0.05$) between the synthetic image and the FFDM image for all three microcalcification clusters. Contrast (E) and CNR (F) of the 5 mass mimics present in the ACR Phantom were also compared. (F) A representative x-ray image of the ACR phantom. The numbers identify the microcalcification cluster (red) and mass (blue) mimics.

The appearance of mass and microcalcification mimics present in the combined CIRS Biopsy and Imaging phantoms (see 3.4.1 Breast-mimicking phantoms) was also asssessed.

Stacking the CIRS Biopsy phantom, which presents pathology against a smooth background, on

top of a single slab of the CIRS Imaging phantom with its complex background, provided the opportunity to demonstrate how the image processing chain used to generate sDBT *synthetic* images minimizes the display of background features present at depths other than the pathologic feature-of-concern. Figure 4.25 shows the processed FFDM, conventional DBT *synthetic*, and sDBT *synthetic* images of this phantom configuration. In the FFDM and conventional DBT *synthetic* image, the swirled background pattern was superimposed on the mass and microcalcification mimics, even though these features were actually present at different depths. However, since the processing to generate the mass-enhanced sDBT *synthetic* image weighted the display of structures as a function of their location in depth from the identified features-of-concern, the swirled background was less prominent in the pathology-enhanced *synthetic* sDBT image compared to the FFDM image and conventional DBT and standard sDBT *synthetic* images. Line profiles drawn through a feature-of-concern showed a more stable signal intensity in the pathology-enhanced sDBT *synthetic* image, suggesting that the pathology was less likely to be obscured by overlapping features present at different depths. Similarly, since the microcalcification-enhanced *synthetic* sDBT image processing approach provided higher weighting to microcalcifications relative to other features, microcalcification visibility was not diminished by overlapping regions.

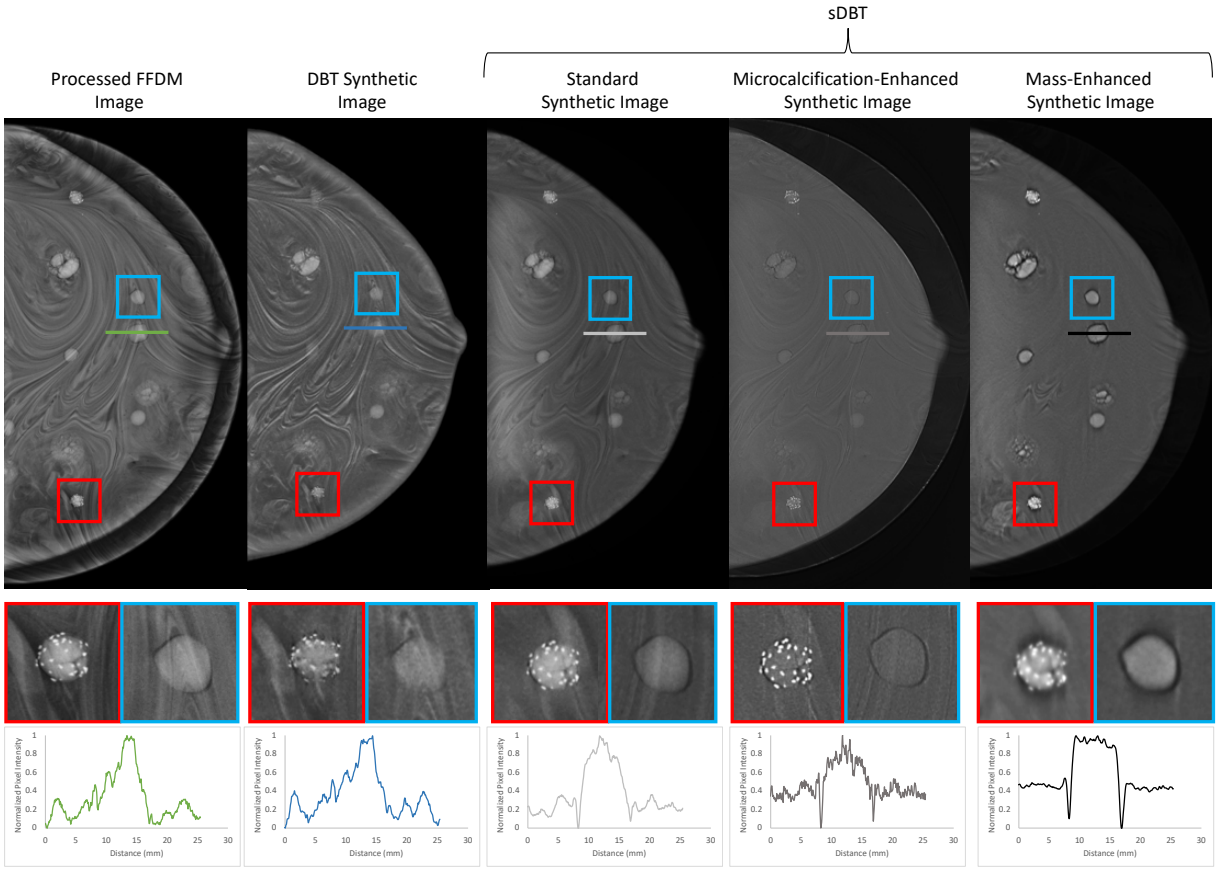


Figure 4. 25. The processed full field digital mammography (FFDM) image and *synthetic* images generated by conventional digital breast tomosynthesis (DBT), and *stationary* digital breast tomosynthesis (sDBT) of the CIRS Biopsy phantom stacked on top of a single slab of the CIRS Imaging phantom. The blue boxes demonstrate the appearance of the same mass in each image, and the red boxes demonstrate the appearance of a mass with calcifications. Note the relative absence of the swirled background pattern in the pathogy-enhanced sDBT synthetic images relative to the others. Line profiles drawn across the same mass mimic in each image demonstrate the effects of the weighting functions applied during the processing to generate these images. The pixel intensities of each line profile were normalized so that the shapes of each profile could be compared more directly. For example, in the mass-enhanced synthetic sDBT image, pixel intensities were stable across the mass, whereas overlapping background features from the CIRS Imaging slab present at a different depth partially obscured the mass in the other images.

Finally, the appearance of mass and microcalcification mimics present in the CIRS Imaging phantom was asssessed. The CIRS Imaging phantom presents mass and microcalcification mimics in a complex background (see 3.4.1 Breast-mimicking phantoms). Figure 4.26 shows this phantom as it appears in the processed FFDM image and *synthetic* images

generated by conventional DBT and sDBT. The overlapping background features make it difficult to visualize microcalcifications and masses in the processed FFDM, conventional DBT *synthetic* image, and standard *synthetic* image generated by sDBT. However, by applying weighting functions to the detected microcalcification or mass features, and thereby down-weighting the overlapping structures present at different depths (see 3.5.3e Forward projecting the 3D image space into *synthetic* 2D mammograms), the visibility of these features was improved (Figure 4.26).

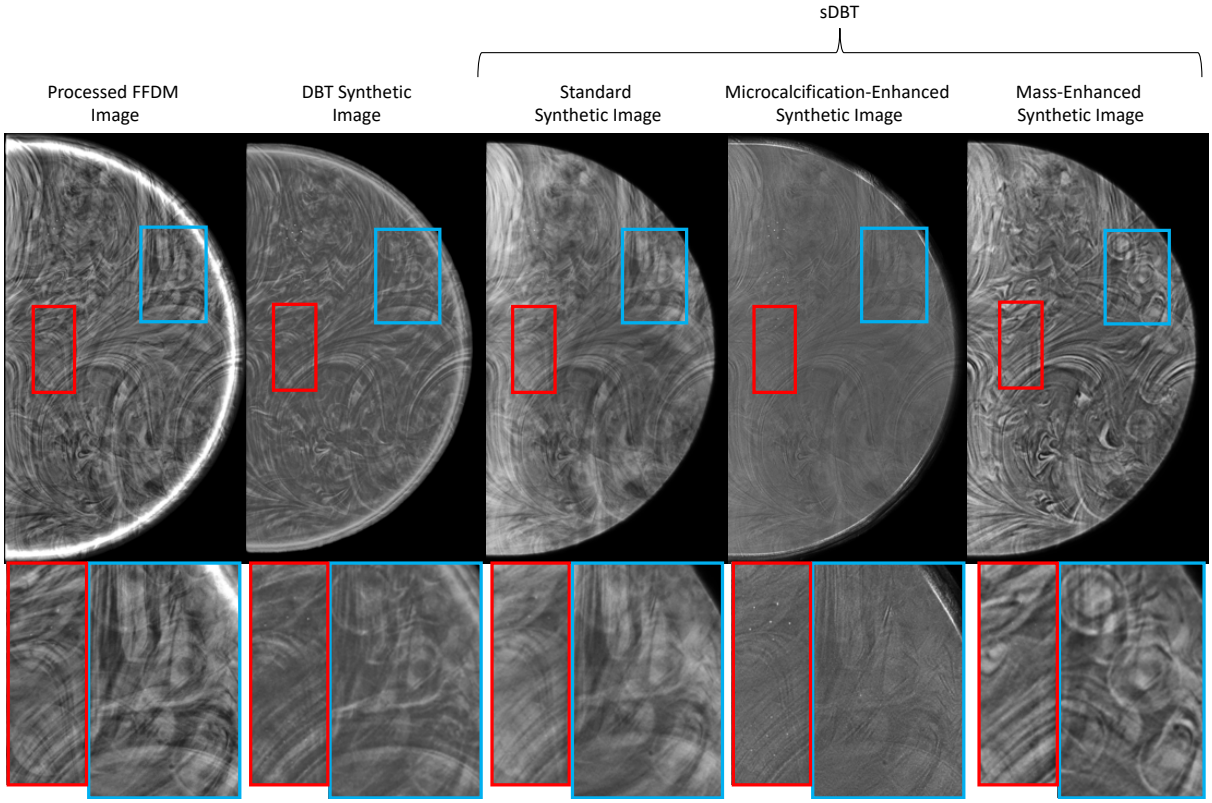


Figure 4. 26. The processed full field digital mammography (FFDM) image and *synthetic* images generated by conventional digital breast tomosynthesis (DBT), and *stationary* digital breast tomosynthesis (sDBT) of the CIRS Imaging phantom. The blue boxes demonstrate the appearance of three mass mimics in each image, and the red boxes demonstrate the appearance of two microcalcification clusters. By applying microcalcification and mass weighting functions during the processing to generate the pathology-enhanced *synthetic* sDBT images, the visibility of these features could be improved.

### *4.4.3 The effect of background equalization on the appearance of the synthetic mammogram*

Decreasing signal intensity in the breast image periphery relative to the central breast region is an inherent image presentation problem in the mammogram, given the fact that there is less tissue thickness where the peripheral breast loses contact with the compression paddle. Without correction, this difference in background intensity between central and peripheral regions is also present in the *synthetic* mammogram. As such, the peripheral breast tissue is difficult to visualize, as demonstrated in representative "uncorrected" clinical images (Figure 4.27). However, the background equalization algorithms developed for this study (see 3.5.3f Equalizing background in the *synthetic* mammogram) stabilized the signal intensity from the central to peripheral breast image regions in the "corrected" *synthetic* mammograms, across the full spectrum from low to high-ordered weighting.

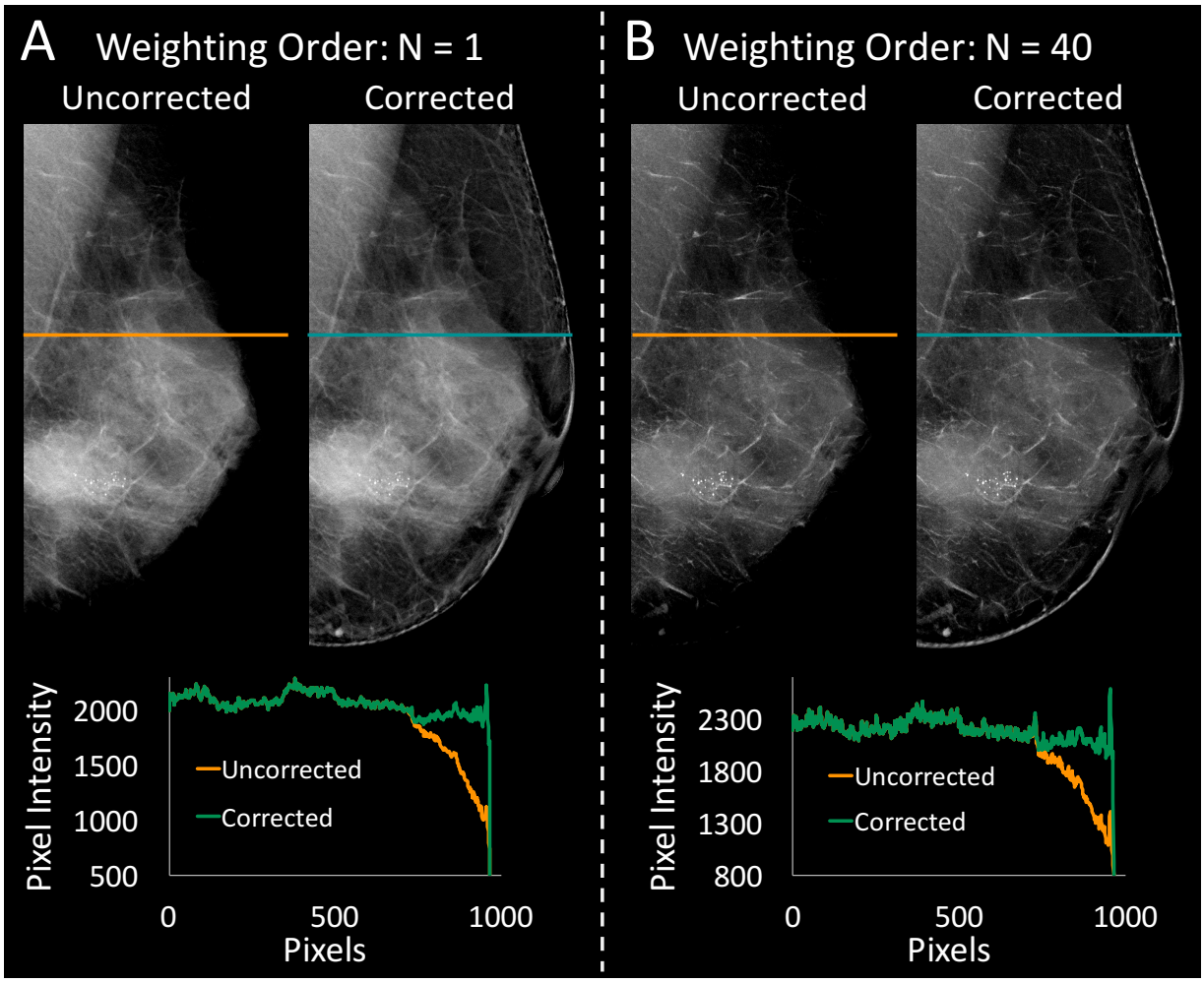


Figure 4. 27. The effect of applying background equalization algorithms to the *synthetic* mammograms generated by *stationary* digital breast tomosynthesis (sDBT). Background equalization algorithms stabilized the signal intensity from the central to peripheral breast image regions (line profiles) when applied with both low-order (A) and high-order (B) weighting during forward projection. Uncorrected and corrected images are displayed at the same window/level settings. Figure adapted from [Puett 2019b].

### *4.4.4 The clinical utility of sDBT-generated synthetic mammograms compared to standard mammography*

The viability of applying the image processing chain incorporating feature-enhancement during forward projection, which was developed through phantom-based experimentation, to clinical images was demonstrated using sDBT studies from two patients with concerning breast lesions. Figure 4.28 presents a mediolateral oblique (MLO) view of a breast with extremely

dense tissue, which obscures soft tissue lesions and their boundaries, making it more difficult to assess the likelihood of malignancy. As can be appreciated by comparing the conspicuity of the mass lesion in the FFDM image and the set of *synthetic* sDBT images, processing designed to isolate the mass in depth improved the display of its boundaries.

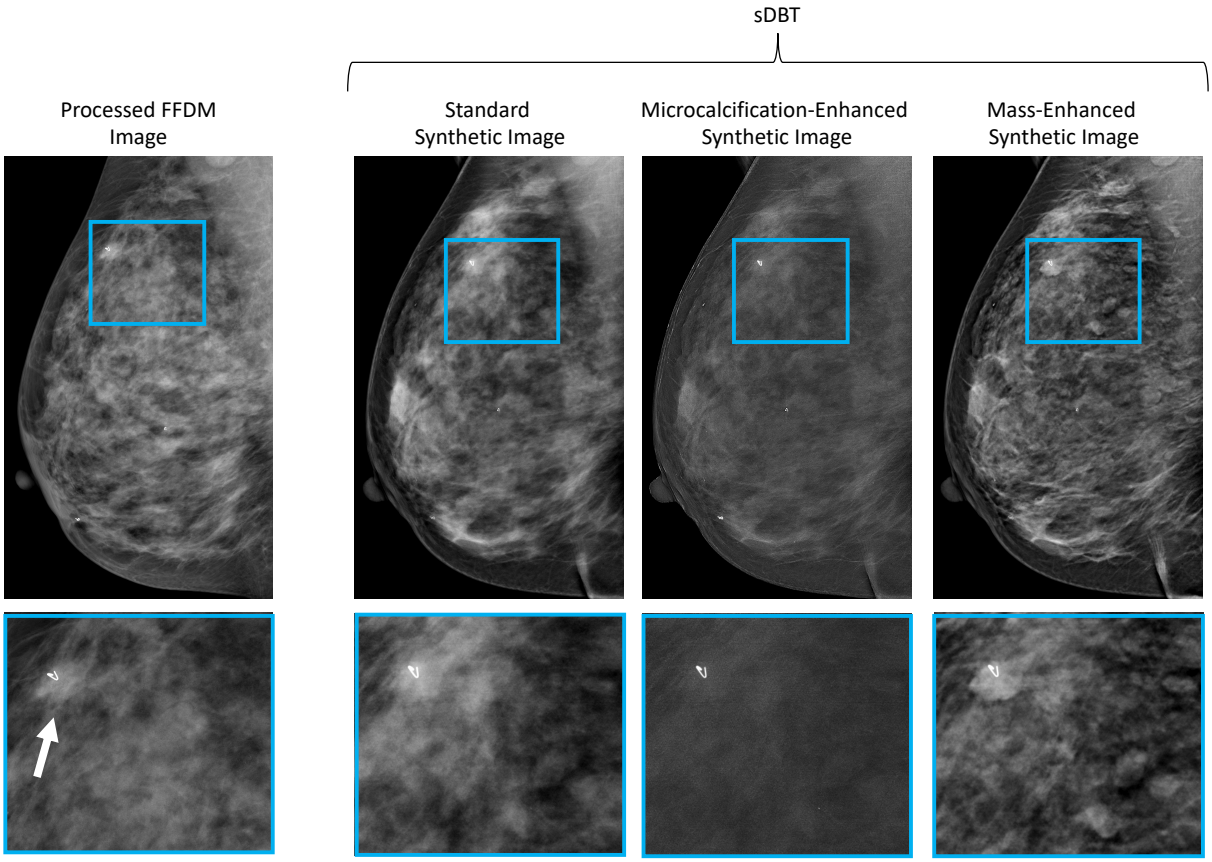


Figure 4. 28. A comparison of the appearance of the full field digital mammogram and *synthetic* images generated by *stationary* digital breast tomosynthesis (sDBT) of a patient with extremely dense breast tissue containing a maligancy. Biopsy of the concerning soft tissue mass (indicated by the white arrow) demonstrated intraductal carcinoma and ductal carcinoma in-situ. Note the improved conspicuity of the mass boundaries in the mass-enhanced *synthetic* image compared to the other images. The cropped image represents a 5.5 x 5 cm region. The full field digital mammogram (FFDM) and sDBT images were acquired at different times and thus involved different compressions.

Figure 4.29 demonstrates the effects of different processing approaches on the appearance of a craniocaudal (CC) view of a breast with microcalcifications. As a result of the the higher weighting given to microcalcifications relative to their background, it was easier to

appreciate the distribution of microcalcifications in the microcalcification-enhanced *synthetic* image, as compared to the FFDM, standard s*ynthetic*, and mass-enhanced *synthetic* images.

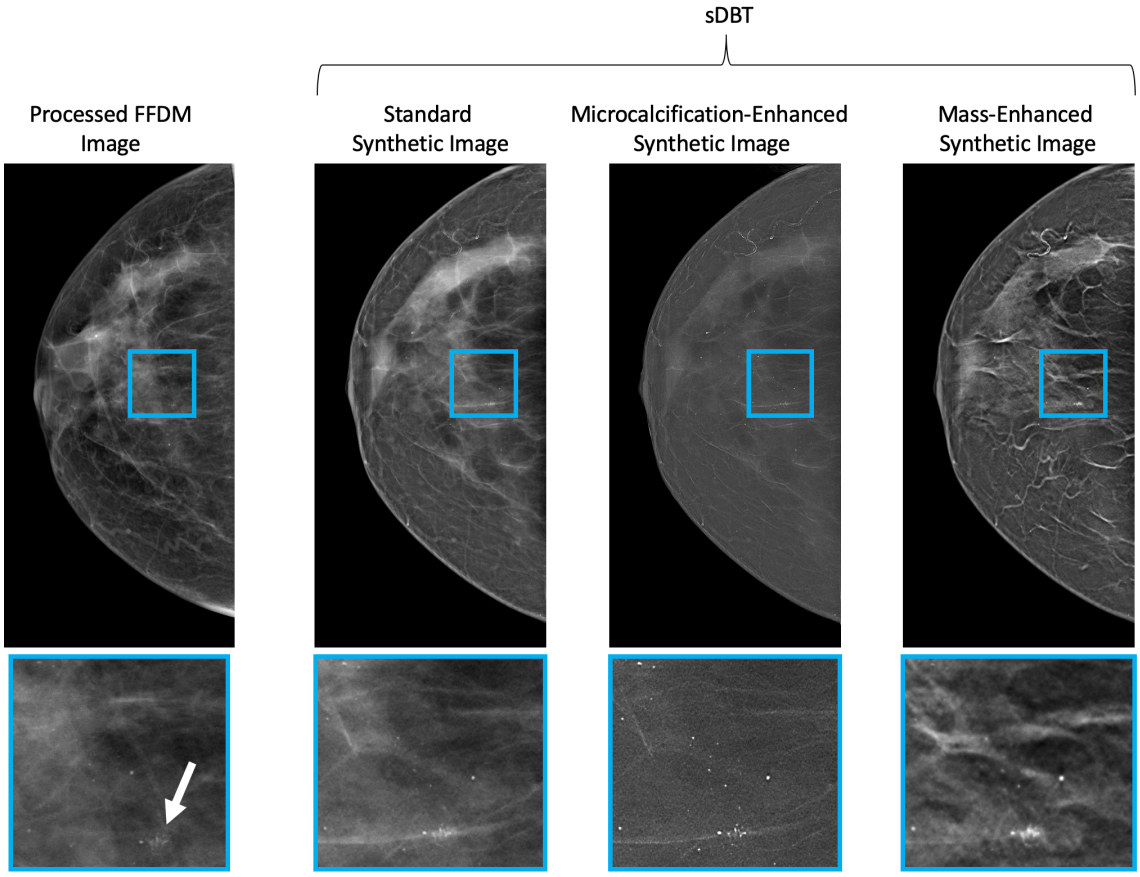


Figure 4. 29. The processed full field digital mammogram and *synthetic* images generated by *stationary* digital breast tomosynthesis (sDBT) of a breast containing microcalcifications. The cropped image represents a 2.5 x 2.25 cm region containing an area of grouped calcifications (indicated by the white arrow). The pathology findings from a stereotactic breast biopsy were indeterminate, and an excisional biopsy was recommended. Note the improved conspicuity of the microcalcification clustering in the microcalcification-enhanced *synthetic* image compared to the other images. The full field digital mammogram (FFDM) and sDBT images were acquired at different times and thus involved different compressions.

These representative examples demonstrate that the current image processing chain can be successfully applied to actual patient images. However, many questions remain. As currently implemented, the *synthetic* mammography information from an sDBT study is presented as a set of *synthetic* images. Although phantom-based experimentation suggests potential benefit to this

approach, which provides an opportunity to optimize the image processing for a specific pathology, this idea of presenting a set of different *synthetic* images is new, and as such, its true clinical value will need to be tested. A well-designed reader study will be necessary to determine if readers are more accurate when interpreting a set of pathology-enhanced *synthetic* images compared to standard FFDM or a single *synthetic* image generated by conventional DBT or sDBT, and if so, whether the improved accuracy is enough to justify the added expenses in reader effort, computation, and storage.

## 4.5 Summary for Chapter 4: Findings

This work sought to advance the clinical potential of sDBT by using a broad spectrum of research approaches, ranging from phantom-based experimentation to human study. As demonstrated by the results summarized in Chapter 4: Findings, testing often sought to define the performance of sDBT relative to other approved and commercially-available breast imaging devices, representing current state-of-the art technologies. Taken as a whole, the findings demonstrate that this experimental technology has the potential for providing images of high quality and diagnostic utility. Additionally, by characterizing the problematic issues of scatter, noise, and artifact, the findings allowed development of image processing approaches that minimized their impact on image quality. Finally, by combining the findings from this broad experience with sDBT, a complete image processing chain capable of generating feature-enhanced *synthetic* mammograms was developed. This important step prepares the way for ongoing human study and provides a foundation upon which future work can be built. Perhaps of most value, the findings help identify specific technological and computational concerns that still need to be addressed, and recommendations for future work suggested by these findings are discussed in Chapter 5: Analysis and Synthesis.

# CHAPTER 5: ANALYSIS AND SYNTHESIS

## 5.1 Introduction to Chapter 5: Analysis and Synthesis

Chapter 5: Analysis and Synthesis reviews the findings of this work in light of the rapidly evolving field of 3D mammography. Advances are being made through research at the academic level and also in the commercial sector, as companies compete in this growing and competitive market. These advances are occurring in both the technology of the devices that capture the information at the time of the study as well as the computational steps that process the images that are eventually displayed for interpretation. Indeed, good technology is wasted if the processing is inadequate to display the information as a clinically-useful image. Additionally, processing can shine light on the limits inherent to a specific technology. In this way, processing often guides system modification, and as a result, technology and processing tend to evolve together. The overall goal of this work was to evaluate the potential clinical utility of *stationary* digital breast tomosynthesis (sDBT) and, through processing, advance sDBT as a clinical tool (see 1.2 Purpose of this work). As a result of this work, processing was developed to address the problematic issues of scatter, noise, and artifact as well as complete the evolution of sDBT to a viable clinical tool through the incorporation of a *synthetic* mammography capability. The utility of the processing when integrated into the sDBT system was tested across a spectrum of applied tasks. sDBT images of breast-mimicking phantoms, lumpectomy tissue specimens, and patients were compared to images acquired by commercially-available full field digital mammography and conventional digital breast tomosynthesis (DBT) devices, which provided state-of-the art technologies as references. Indeed, this dissertation was focused on sDBT and therefore the

challenges introduced by this novel system. However, issues addressed in this work are inherent to some degree in all 3D mammography systems. As such, it is anticipated that the findings will be of value to the field of 3D breast imaging in general. Chapter 5: Analysis and Synthesis discusses the findings from this work in this broader context. It highlights differences between sDBT and conventional DBT in light of their functionality and anticipated directions for ongoing development. The discussion is initially organized around the three key issues that force compromise in the design and operation of 3D mammography systems: resolution, scatter, and artifact. Understanding how different systems handle these issues demonstrates the critical interplay of technology and processing, as each system seeks to generate high-quality images containing the most useful clinical information. The discussion then turns to the processing chain that generates the *synthetic* mammogram and the key step of feature-identification, since the development of *synthetic* mammography with an enhanced feature display is an active area of current research in this field. To conclude, the point is made that the sDBT technology is now poised to become a valuable clinical tool.

## 5.2 Discussion for Chapter 5: Analysis and Synthesis

### *5.2.1 Using resolution, scatter, and artifact to appreciate differences in DBT systems and directions of development*

The use of DBT has grown rapidly in the US since the first device was approved by the FDA in 2011 [Gao 2017]. Since then, seven manufacturers have brought devices to the market world-wide, each with different approaches to acquire the projection images at the time of the study. Each device seeks to produce projection images of the highest possible quality, as these projections contain the information utilized by processing to generate the images displayed for interpretation. The goal is to minimize noise, scatter, and artifact in order to capture images with the maximum possible resolution, working within the strict requirements imposed by using x-

rays for breast screening. More specifically, mammographic screening requires low radiation doses and fast scan times. Additionally, the images need to display tissue features with very different tissue compositions and sizes and therefore image characteristics. Design differences reflect attempts to optimize performance within these constraints, resulting in compromises in each system. These compromises involve a number of physical parameters, but in large part, they deal with the need to translate an x-ray source to different positions relative to the breast to acquire the set of projection views. As demonstrated throughout this work, sDBT is fundamentally different from all of the commercially-available systems, as it acquires projection images using an array of *stationary* and rapidly-responsive x-ray sources made possible by carbon-nanotube (CNT) technology. The implications in terms of acquiring wider angle spans quickly and eliminating source blur are clear. However, these benefits were achieved at a price, as the design and operation of the current multi-source x-ray tube itself forced compromise. The impact of this tube design on the key issues of resolution, scatter, and artifact are discussed below, with comparison to the commercially-available technologies against which sDBT is being judged. As a result of this comparison, directions for the ongoing development of sDBT are suggested in light of the evolving field of 3D mammography in general.

*5.2.1a Resolution: anode focal spot size, source motion, detector pixel size, and noise*

Resolution reflects the geometry of the imaging system and influences the quality of the images it produces (see 2.4 Defining and measuring the quality of the digitized image and 2.5 Image quality problems inherent to tomosynthesis in general and sDBT in particular). Commercially-available DBT technology requires physically moving an x-ray source through space to collect the series of oblique projections used to generate the 3D image [Zheng 2019]. As noted above, the limitations imposed by source motion are responsible for many of the design

differences in current 3D mammography devices (see 2.2.4 The clinical value and technical limitations of conventional 3D mammography). For example, since source motion elongates the effective focal spot in the direction of motion, some commercially-available systems utilize a step-and-shoot protocol [Mackenzie 2017, Vedantham 2015]. However, this approach prolongs the overall scan time, increasing the risk of introducing blur by patient motion and limiting the number projection views and angle span achievable during the scan. Decreasing the x-ray on-time, thereby decreasing the distance the source travels while firing, also decreases focal spot elongation. However, it decreases the signal-to-noise ratio, as fewer photons are released during the shorter on-time. Increasing the relative noise contribution to the total signal, especially in a low-dose study such as DBT, compromises image quality (see 2.4 Defining and measuring the quality of the digitized image). Similarly, decreasing the size of the detector pixel can improve resolution. However, smaller pixels collect fewer photons, again compromising the signal-to-noise ratio.

The appeal of using stationary arrays of CNT-enabled x-ray sources is that it solves the problem of source motion. As such, *stationary* DBT has the potential to collect higher resolution images. However, as currently-operated, the resolution of the first and second generation sDBT devices is similar to conventional DBT, despite its stationary design, as demonstrated by comparisons to the parent moving-source DBT system that provided the foundation for sDBT. This similarity was reflected by their modulation transfer functions (MTFs) (see 3.5.1a Differences in the breast-imaging systems) as well as the fact that sDBT and conventional DBT displayed equivalent in-plane microcalcification sizes in images of lumpectomy specimens when binning was used to equalize the detector pixel sizes (see 4.3.1 Visualizing microcalcifications in lumpectomy specimens). Finally, as expected given its larger anode focal spot size, the

resolution of the sDBT system was lower than standard mammography, perhaps best reflected at the clinical level by the display of microcalcifications. Readers consistently rated the conspicuity of microcalcifications higher in standard mammograms than sDBT images, when comparisons were made to both reconstructed 3D sDBT images of actual patients (see 4.3.2c Reader preference when interpreting image features) and *synthetic* slab images of lumpectomy specimens (see 4.3.1 Visualizing microcalcifications in lumpectomy specimens).

The main technological issue lowering the resolution of the sDBT systems is the focal spot size. Although sDBT solves the problem of source blur, the current tube design requires using larger anode focal spot sizes than conventional DBT, since the stationary anode does not include a cooling method for dissipating heat generated during x-ray production. In order to achieve the dose rates necessary for clinical imaging, the focal spot size is increased to distribute anode heating over a larger area. To compensate, the sDBT detector is operated in a full-resolution mode, with a small detector pixel size of 70 μm. However, as noted above, smaller pixels result in a lower signal-to-noise ratio, and the relative increase in noise must be addressed in processing. Therefore, the current performance of sDBT balances its advantages of fast scanning over a large angular span with no source motion against its current limitations of larger focal spot sizes and higher noise.

Altogether, sDBT performed as well as, and in many cases better than, conventional DBT, when quality was assessed in *synthetic* images of breast-mimicking phantoms (see 4.4 Incorporating *synthetic* mammography into sDBT) and when readers rated the display of microcalcifications in *synthetic* images (see 4.3.1 Visualizing microcalcifications in lumpectomy specimens). As such, it can be anticipated that changes in the x-ray tube design to improve the resolution of the sDBT system would produce a device with significant advantages over the

currently-available technology. The key will be the incorporation of a rotating anode or anode cooling, thereby supporting electronic focusing to achieve smaller focal spot sizes and higher dose rates to improve the resolution and signal-to-noise ratio.

*5.2.1b Scatter: approaches to practical scatter reduction*

Although scatter is present in every x-ray image, the scatter signal can actually predominate the non-scattered or primary signal in some modalities and anatomic environments (see 2.4.3 Scatter and noise). As such, scatter reduction techniques such as air gaps or anti-scatter grids are utilized during most x-ray studies, including standard mammography. These techniques make it less likely that photons traveling oblique paths, and thus more likely to have been scattered, will reach the detector. However, tomosynthesis works by collecting a series of projection views at oblique angles. As such, standard scatter-reduction techniques are problematic, since they further decrease the photon count of an already low-dose technique, thereby compromising the signal-to-noise ratio (see 2.4 Defining and measuring the quality of the digitized image and 2.5 Image quality problems inherent to tomosynthesis in general and sDBT in particular). As demonstrated in this work, there is a significant scatter component to the total signal in sDBT images (see 4.2.1 Quantifying scatter in contrasted and non-contrasted sDBT images). In fact, similar to findings with conventional DBT, there is a strong correlation between the scatter-to-primary (SPR) ratio and breast thickness, with SPR values in the range of 0.4 for 3 cm thick and greater than 0.5 for 5 cm thick tissues [Puett 2018b].

A variety of solutions have been proposed for addressing the issue of scatter in DBT imaging. One DBT system incorporates a linear anti-scatter grid just above the detector [Vedantham 2015]. Others have proposed the use of a precomputed scatter library, which can be used to efficiently look up scatter values based on patient characteristics and a given set of

system parameters [Feng 2014]. Our approach to scatter correction involved acquiring a second scan to indirectly sample scatter using a primary sampling device (PSD). This method provides a patient-specific measure of scatter, which can be corrected through processing. Scatter correction through image processing improved image quality, yielding a statistically-significant improvement in the CNR when a filtered scatter-correction algorithm addressing the noise component of the scattered signal was incorporated into the image processing chain (see 4.2.2 The effect of scatter and noise correction through processing on sDBT image quality). The additional dose from the second scan with the PSD in place is only 3% of the scan without the PSD. However, this additional imaging increases the overall study duration, increasing the breast compression time and chance for patient motion. Improving the dose rate of the sDBT system (see 5.2.1a Resolution: anode focal spot size, source motion, detector pixel size, and noise) and utilizing a detector with a short readout time would allow for the fast collection of images with and without the PSD in place. Future work is needed to develop the hardware to quickly and safely insert and remove the PSD from the field-of-view during clinical imaging.

*5.2.1c Artifact: angular span and reconstruction*

The ability to detect the boundaries of a feature in an x-ray image through depth is directly related to the angular span of the projection images [Zhou 2007]. A wider-angle span supplies more depth information, reducing the amount of tissue overlap in the reconstructed 3D image space. In addition to improving depth resolution, increasing the angle span would be expected to yield fewer out-of-plane artifacts in the images displayed for interpretation. The benefits of the wider span of projection views achievable by sDBT compared to conventional DBT was demonstrated by the smaller artifact spread function (ASF) through the reconstructed sDBT image stack of lumpectomy specimens (see 4.3.1. Visualizing microcalcifications in

lumpectomy specimens). This work also demonstrated the clinical utility of dense-feature artifact reduction algorithms for sDBT (see 4.2.3 Understanding and removing artifact related to highly-attenuating features with *stationary* tomosynthesis and 4.2.4 Applying artifact reduction algorithms to sDBT). However, artifact cannot be completely eliminated, suggesting that the ability to collect a wider span of projection views would also be of benefit. The first and second generation sDBT devices studied in this work offered an angle span of 28° and 35°, respectively. Placing this in context, commercially-available DBT devices offer angle spans ranging from 15 to 50° [Vedantham 2015]. In addition to improving resolution, technological changes in the CNT-enabled x-ray source allowing a higher dose rate, combined with a detector offering a full-resolution pixel size with a faster read-out rate, would provide the opportunity to collect a wider span of projection views within a short scan time.

### *5.2.2 Appreciating the critical step of feature-identification for enhanced synthetic mammography*

The *synthetic* mammogram is proving to be a valuable clinical tool [Durand 2018, Ratanaprasatporn 2017]. In fact, the ability to generate a clinically-useful *synthetic* mammogram is considered to be a key step by which 3D mammography will replace standard 2D mammography as the breast imaging tool of choice, since it would obviate the need to collect both 2D and 3D mammography scans for screening (see 2.6 The image processing chain that generates sDBT images and the value of the *synthetic* mammogram). Therefore, the incorporation of a *synthetic* mammography capability into the sDBT system was identified as a key step to advance the clinical potential of the sDBT system and therefore considered a Specific Aim of this dissertation project (see 1.2 Purpose of this work, 1.3 Research questions asked in this work, and 4.4 Incorporating *synthetic* mammography into sDBT). As originally conceived, the *synthetic* mammogram was seen as a complement to the 3D image stack with several

potential uses. For example, compared to the full image stack, the *synthetic* mammogram could be compared more directly to previous standard mammograms in order to assess change. Also, since it summarized the findings distributed through the full image stack into a single image, it could provide an efficient reference, guiding readers to regions of concern in the full image stack. However, research over the past few years has demonstrated that the *synthetic* mammogram has the potential to offer readers information with a higher diagnostic value than the standard mammogram [James 2018]. Improving the diagnostic value of the *synthetic* 2D image is accomplished by identifying features-of-interest in the 3D image stack and emphasizing these features in the *synthetic* image. In other words, the *synthetic* mammogram may be able to combine the benefits of decreased tissue overlap available in the 3D image stack with the efficiency of interpreting a 2D image. However, identifying and enhancing breast pathology in the x-ray image are difficult tasks, given the highly-variable appearance of diagnostically-important breast lesions. For example, masses and microcalcifications have very different image properties, including size and contrast, and often need to be distinguished from the dense and complex backgrounds in which they are located. As a result, numerous steps are required in the image processing chain that generates the *synthetic* mammogram. In fact, the algorithms developed for sDBT generate a set of *synthetic* images, each the result of a different image processing chain dedicated to the display of a specific type of pathology, such as the soft-tissue mass or microcalcification cluster. These processing chains incorporate combinations of Laplacian decomposition, weighted forward projection, and weighted recombination customized to sDBT to generate the *synthetic* image (see 4.4 Incorporating *synthetic* mammography into sDBT). Testing to date using objective measures of signal intensity and feature detectability suggest that these sDBT *synthetic* images will be useful (see 4.4.2 Phantom-based testing of a

forward projection approach incorporating feature enhancement). However, reader study of patient images will be required to determine their actual clinical value (see 4.4.4 The clinical utility of sDBT-generated *synthetic* mammograms compared to standard mammography). Several vendors offer the option to generate s*ynthetic* mammograms, including Hologic (C-View), GE (V-Preview), and Siemens (Insight) [Durand 2018]. Each is proprietary and yields images that emphasize different characteristics. As such, the clinical value of each differs, and the development of computer algorithms to generate *synthetic* images from the information collected by a DBT study remains a rapidly-evolving area of quite active research [Geras 2019, James 2018]. In large part, this research is focused on improving the detection of features in the 3D image space, so that diagnostically-important features are most-importantly (1) not missed, (2) accurately displayed, and (3) perhaps even enhanced in the *synthetic* image. Indeed, for all image processing approaches designed to produce feature-enhanced *synthetic* images, the accuracy of the feature-detection step is key.

Recent experience with standard 2D mammography as well as moving-source DBT has suggested that deep learning algorithms have the potential to improve the accuracy of feature identification [James 2018, Rodriguez-Ruiz 2018, Rodriguez-Ruiz 2019, Geras 2019]. GE offers a CAD-enhanced *synthetic* mammography option (Enhanced V-Preview) that identifies up to five suspicious soft tissue lesions in the 3D image stack and enhances the lesions in the *synthetic* image [iCAD 2017]. Hologic has developed an artificial intelligence-based approach to generate 6-mm-thick "SmartSlices," in order to reduce the number of images and storage space requirements of the 3D stack while maintaining important feature display [Hologic 2020]. The image processing chain developed for sDBT in this dissertation work should accommodate a deep learning feature-detection algorithm. However, such networks require extensive training.

As such, their development is dependent on the availability of a library of annotated images displaying a broad range of pathology. Building such a library of actual patient images would require many years of ongoing clinical experience, which should be considered an important step for sDBT. However, recent advances in the generation of images using a virtual DBT model have suggested the opportunity to generate image databases through virtual clinical studies for algorithm training [Badano 2018]. Computer training based on a virtual sDBT system and a collection of virtual sDBT images would greatly accelerate the development of image processing for the sDBT system and should be considered as a future direction for research with this experimental technology.

### 5.3 Summary for Chapter 5: Analysis and Synthesis

This dissertation work sought to advance the clinical potential of sDBT. It did so through experimentation to understand the problematic areas of scatter, noise, and artifact in the sDBT system and to compare the performance of sDBT to commercially-available devices that define the current standards for reference. The findings were used to develop key image processing capabilities for the sDBT system, culminating in a complete image processing chain to generate *synthetic* mammograms. By identifying the most problematic limitations in the sDBT system, this work also suggested future avenues of technological development that would complement ongoing advances in processing, since technology and processing need to evolve together to produce a system capable of generating images with the highest clinical value. Chapter 5: Analysis and Synthesis placed the findings of this dissertation work in the context of the rapidly-evolving field of 3D mammography in general. As discussed in this chapter, continued work with the sDBT system should focus on incorporating anode cooling to support smaller focal spot sizes and higher dose rates, an efficient scatter measurement system to collect the information

needed for scatter correction, and a digital detector with a high readout rate. In addition, from a computational standpoint, building an extensive library of sDBT images through continued clinical studies or virtual modeling will provide the data for the ongoing development of advanced image processing. The goal of this project was to advance the clinical potential of sDBT, and as a result of this work, sDBT is now capable of generating both 3D and *synthetic* 2D images of high clinical value. Additionally, directions for ongoing development are better defined. At this point, sDBT is well-positioned for the next step in its evolution, as it appears clear that this unique technology provides an opportunity to improve the detection and evaluation of breast cancer.

# CHAPTER 6: CONCLUDING WITH A LOOK TO THE FUTURE

## 6.1 Exploring unique diagnostic applications of sDBT: dynamic, magnified, and multiplexed imaging

This dissertation work focused on the clinical potential of sDBT as a screening tool. The findings are encouraging, demonstrating that this experimental technology performs as well as commercially-available standards while also suggesting avenues of research and development in terms of both technology and processing that may significantly improve its performance (see Chapter 5: Analysis and Synthesis). Given its potential to collect images over a wider-angle span more quickly than existing technologies as well as its potential for a higher system resolution, sDBT is certainly a promising screening tool. However, sDBT may prove to be of most value in the arena of diagnostic breast imaging, which refers to the detailed characterization of concerning lesions identified by screening. Given its unique design, sDBT can perform 3D breast imaging tasks that are difficult or even impossible with conventional 3D mammography. Examples include dynamic, multiplexed, and magnified 3D mammography. As a group, these approaches to diagnostic breast imaging require the ability to coordinate and collect multiple different projection views quite quickly or even simultaneously. Magnified mammography utilizes a small focal spot size and positions the breast closer to the x-ray source. Given this geometry, image quality is significantly compromised by blur if there is any motion from the x-ray source or patient, as these motions have a relatively greater influence on resolution given the larger distance between the target and detector [Marshall 2012]. As such, a brief scan time and stationary x-ray source at image acquisition would be beneficial. Multiplexed imaging refers to

the collection of several projection views simultaneously, thereby providing an opportunity to complete a full scan very quickly [Yang 2011]. Collecting multiple projections simultaneously is not possible when working with a single source. Dynamic contrast-enhanced, or four-dimensional (4D), mammography involves collecting images through time, as intravenously-injected contrast accumulates in and then washes out from a breast lesion [Brandan 2016]. Both the appearance of the contrasted vasculature as well as the timing of the wash-in and wash-out phases can have diagnostic value [Dromain 2006, Diekmann 2011]. Therefore, the ability to collect temporal information from multiple views quickly would be beneficial. Collectively, these diagnostic applications take advantage of the very high temporal resolution offered by the sDBT system. The processing algorithms developed in this work can be adapted to these unique image acquisition protocols, although modifications to the hardware that coordinates source firing, such as the electronic control system (ECS), and detector activity would also need to be made.

### 6.2 Exploring advanced image processing for sDBT: deep learning and radiomics

The application of the image processing and technological advances suggested by this work should prepare this experimental technology for large-scale human studies. From a processing standpoint, the collection of patient images across a broad spectrum of breast densities and pathologies would provide a library for future study. Such a library would be invaluable, as it would make possible the exploration of cutting-edge image processing approaches, including deep learning [Geras 2019] and radiomics [Tagliafico 2018]. In its most basic form, deep learning exposes a computational network to a large number of images, applying algorithms with which the computer learns to recognize key patterns. With enough experience, the network can be trained to accomplish a variety of tasks, including feature

detection and feature classification. For example, the network might recognize a potential mass in the reconstructed image stack, bringing it to the reader's attention, perhaps by emphasizing it in the *synthetic* mammogram (see 5.2.2 Appreciating the critical step of feature-identification for enhanced *synthetic* mammography). Current experience with deep-learning suggests the need to expose a network to thousands of images to train an accurate pattern recognition [Shen 2019]. Radiomics builds upon this concept of pattern recognition, using computational approaches to extract image features from a defined region of the image with known pathology. The goal is to associate image features with physical characteristics of the lesion, such as genetic or molecular signatures [Tagliafico 2018]. To the human eye, the extracted image features may appear meaningless, but recent work with mammography has shown that the application of deep learning and radiomics allows a correlation between image features and breast cancer type [Yala 2019]. Additionally, there is early evidence that radiomic analysis can identify image markers that may help guide treatment [Tagliafico 2019]. In light of these exciting possibilities, we can only imagine the potential utility of providing these algorithms with the additional high-quality and 3D information collected by an sDBT study.

## 6.3 Applying the lessons learned

To conclude, it is hoped that the work contained in this dissertation will provide a useful step toward expanding our clinical experience with sDBT. The lessons learned will certainly impact the direction of future progress with sDBT. However, these lessons also have application to CNT-enabled *stationary* tomosynthesis devices across the diverse spectrum of imaging tasks that are being explored. Currently, *stationary* tomosynthesis is also being tested at the clinical level for dental, musculoskeletal, and chest imaging. Also, a CNT-enabled *stationary* head CT scanner is under construction [Spronk 2020]. When viewed in this broader context, it is clear that

the true value of the work contained in this dissertation does not lie in details of the experimental findings themselves or the algorithms that have been developed specifically for sDBT, as these are expected to evolve with the technology over time. Rather, its value lies in the lessons that have been learned regarding the performance of *stationary* tomosynthesis devices in general and the opportunities for future study that the findings and developed tools will help make possible.

# APPENDIX: DEVELOPING *SYNTHETIC* DENTAL RADIOGRAPHY

## A.1 Recognizing the influential relationship between *synthetic* dental radiography and *synthetic* mammography

Although this dissertation work was focused on breast imaging by *stationary* digital breast tomosynthesis (sDBT), it was carried out in the context of applying *stationary* tomosynthesis across a broad range of applications, using carbon nanotube (CNT)-enabled devices customized for different imaging tasks (see 2.3.2 Carbon nanotube-enabled x-ray source arrays and *stationary* digital tomosynthesis). The preclinical characterization of *stationary* intraoral tomosynthesis (sIOT) [Inscoe 2018] was of particular relevance, given the image processing challenges introduced by the unique dental anatomic environment. Lessons learned from experience with sIOT influenced the processing approaches developed for sDBT, which in turn provided much of the basis for the ongoing development of the processing approaches applied to the sIOT system.

## A.2 3D dental imaging and the potential clinical value of the *synthetic* dental radiograph

X-ray imaging is used extensively in clinical dentistry for screening and diagnosis. During intraoral imaging, which typically involves bitewing, periapical, or occlusal viewing, the x-ray detector is positioned inside the oral cavity, yielding one or more two-dimensional (2D) images. These images are immediately available and familiar to the dentist, such that their information can be used to make clinical decisions at that visit. However, 2D images are inherently limited by overlapping tissues, which can make it difficult to visualize pathology. Common problematic imaging tasks for which three-dimensional (3D) imaging has been shown to be helpful include the identification of interproximal caries [van Daatselaar 2003], recurrent caries adjacent to restorations [Nair 1998], root fractures in endodontically-treated teeth [Hekmatian 2018], and bone resorption around implants [Vera 2012].

However, at least until recently, the technologies for 3D imaging have not been appropriate or practical for the busy dental clinic. Cone beam computed tomography (CBCT) is available, but the equipment is large, expensive to purchase, and difficult to maintain. Also, both its operation and image interpretation require specialized training and experience, and the relatively large field-of-view and number of image slices require longer interpretation times. It delivers a radiation dose that is unacceptably high for frequent use, and finally, and perhaps most importantly, CBCT has a lower in-plane spatial resolution than intraoral 2D imaging, and the images themselves often contain artifact [Schulze 2011]. As a result, CBCT is not used as a primary tool for caries detection [Park 2011]. Tuned-aperture CT (TACT) has been explored as an option to provide quasi-3D imaging using an intraoral detector [Webber 1997]. TACT involves the acquisition of multiple x-ray projections over a limited angle relative to the detector, providing the information to construct a 3D image. Relative to CBCT, TACT offers a higher in-plane resolution but lower depth resolution. However, since the image processing steps that construct the 3D image require precise knowledge of the system geometry, care is needed when acquiring the images, and this relatively time-consuming process made TACT impractical for routine use [Tyndall 2008].

*stationary* intraoral tomosynthesis (sIOT) is an experimental 3D imaging technology that has been developed specifically for the busy dental clinic [Inscoe 2018]. sIOT uses a fixed and distributed array of carbon nanotube (CNT)-enabled x-ray sources. Similar to TACT, it acquires x-ray projections from multiple views relative to a fixed intraoral detector. However, the equipment itself and its operation were designed to mimic the standard intraoral x-ray equipment currently in use, and since the imaging geometry is stationary, no additional time or training is needed to perform the scan. Given its potential to provide some 3D information using a protocol

similar to standard intraoral imaging, sIOT may provide a viable 3D imaging option, and its utility is being explored for a host of imaging tasks. For example, previous work with sIOT has demonstrated its ability to reduce tooth overlap [Inscoe 2018, Mauriello 2018, Mauriello 2020] as well as significantly improve the detection of interproximal caries [Inscoe 2018, Mol 2015, Shan 2015] in the 3D images of ex-vivo tooth specimens, as compared to standard 2D intraoral radiography. A clinical study is underway to evaluate sIOT for the detection of interproximal caries in human subjects (ClinicalTrials.gov Identifier: NCT02873585).

However, sIOT does have limitations, perhaps most notably in the presentation of the information for interpretation. Similar to other 3D imaging technologies, the information obtained during a tomosynthesis study is most commonly displayed as a stack of image slices. This 3D stack of images is "reconstructed" by computer programs from the 2D information present in the multiple projection views collected at the time of the study. The reader scrolls through the stack of image slices to appreciate anatomic and pathologic changes through depth. In this way, features-of-interest can be separated from overlapping structures that would otherwise obscure them in a single 2D image. Typically, the reconstructed image slices step 0.5 mm through depth, such that an sIOT scan can produce an image stack containing more than 40 images. Reviewing all of these images takes time, and since the reconstructed images do not appear exactly the same as the standard 2D radiograph, training and experience are needed for accurate interpretation. Additionally, the reconstructed image slices often contain prominent artifact. This artifact results from the fact that tomosynthesis involves collecting only a small number of projection views over a limited angle span, and as a result, there is incomplete data to isolate features fully through depth. Artifact is most problematic when the images contain dense features with sharp edges, as is characteristic of enamel, bone, and especially metal, and can

include in-plane shadowing and out-of-plane ringing [Puett 2020b]. Even though these artifacts become less distracting with experience, they can hide pathology. have been shown to improve the visibility of regions adjacent to amalgam restorations and implants in the 3D image stack [Puett 2018c], although assessing subtle pathology in these critical boundary regions remains problematic.

Processing provided an opportunity to improve the appearance of the reconstructed image slices generated by sIOT, and as noted above, work developing image processing chains for sIOT was carried out alongside the development of processing for sDBT. Although the processing goals with sIOT and sDBT were similar and sought the display of high-quality images for interpretation, dental and breast imaging introduced quite different challenges, given their very different anatomic environments and the different clinical questions that the images were being used to answer. Working through these challenges provided invaluable lessons, so that the work on dental and breast imaging tended to evolve together. Initial work focused on segmentation approaches to reduce the dense-feature artifacts present in the reconstructed slices of the 3D image stack. With breast imaging, dense-feature artifact was most prominent around metal needles and wires used to guide biopsy, metal clips, and large calcifications (see 3.5.3c Reducing artifact, 4.2.3 Artifact reduction in reconstructed and *synthetic* sDBT images), while metal restorations and implants offered good models to study dense-feature artifact during dental imaging (see A.5 Understanding and correcting dense-feature artifact in sIOT images). However, even an artifact-reduced stack of reconstructed image slices proved problematic. An sIOT scan can produce a stack containing more than 40 images. Reviewing all of these images takes time, and since the reconstructed images do not have the same appearance as the standard 2D dental radiograph, training and experience are needed for accurate interpretation. Based on experience

with sDBT, *synthetic* radiography was explored as an option to combine the efficiency and familiarity of 2D imaging with the improved diagnostic accuracy of 3D imaging.

For the development of *synthetic* dental radiography, images of recurrent caries adjacent to previous restorations (CAR) and vertical root fractures (VRF) in extracted teeth were utilized (see A.3 Tooth specimens used to develop image processing for sIOT). These two pathologies were selected for study for several reasons. First, both conditions are challenging to diagnose in the clinic and represent conditions for which a 3D imaging tool would be beneficial. Additionally, both challenge tomosynthesis as an imaging modality, since they exemplify subtle pathologies adjacent to dense features. As a result, the processing chain producing the *synthetic* radiograph needed to conserve the pathologic feature in the image while also removing the often more prominent artifact and obscuring structures around them. Finally, from an image processing standpoint, CAR and VRF lesions are features with very different properties in the image. CAR lesions are diffuse with indistinct boundaries, while VRFs are thin and defined by sharp edges. As such, the development of image processing chains for both provided experience across a range of processing challenges, with applications to breast as well as dental imaging.

### A.3 Tooth specimens used to develop image processing for sIOT

Images of extracted and de-identified human tooth specimens were used during the development of processing for sIOT. These specimens often contained caries, restorations, and fractures. A cadaveric mandible with an implant and a dental x-ray teaching and training replica (DXTTR) including cadaveric dentition as well as a ratcheting clamp to reproduce biting forces (Figure A.1C) were also imaged [Puett 2018c]. As much as possible, the tooth specimens were prepared so as to mimic the anatomic structures of the oral cavity. For example, specimens containing CAR were mounted between two other teeth in a plastic block using modeling clay

[Hilton 2019]. This model recreated interproximal spaces and approximated the attenuation of surrounding tissues. The fractures in the VRF specimens were induced using a steel wedge applied to decoronated premolars [Regan Anderson 2017]. The root canals were debrided, simulating an endodontic procedure, and some of the debrided canals were obturated with gutta-percha using a single cone technique, so as to avoid the chance that any dense obturation material would infiltrate the fracture. The individual specimens were stabilized using rubber cement, which also replicated the periodontal ligament space, and were then mounted in plaster and crushed walnut shells to simulate alveolar bone and bone marrow spaces. When imaged, both specimen groups were positioned directly on the detector to reproduce the proximity achieved by an intraoral sensor location and then covered with 1-cm thick wax, simulating the soft-tissues of the cheek. Ground-truth knowledge of the dental pathology in these specimens was obtained by direct visualization, with sectioning of the tooth used to confirm the CAR lesions [Hilton 2019].

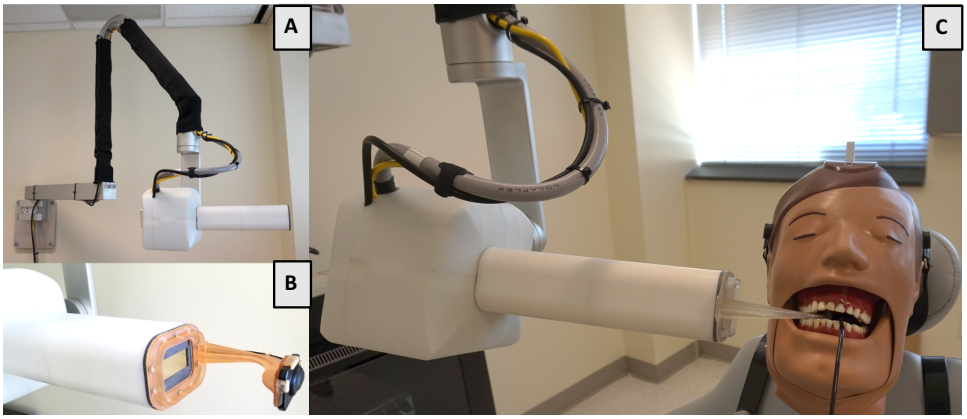


Figure A. 1. Pictures of the first-generation *stationary* intraoral tomosynthesis (sIOT) device, which has been installed in the clinic at The University of North Carolina at Chapel Hill School of Dentistry for human study. The articulating arm and compact size of the x-ray tube (A) were designed to be similar to standard dental imaging equipment. A custom connector (B) aligns the detector with the x-ray tube and maintains a fixed system geometry, as demonstrated during its application on a dental x-ray teaching and training replica (DXTTR), complete with cadaveric dentition and biting clamp (C). Figure adapted from [Puett 2018c].

## A.4 Acquiring sIOT images and reconstructing the 3D image stack

The sIOT system was designed to fit into the typical workspace of a busy dental office. Constructed by Surround Medical Systems, Inc., the system has a wall-mounted x-ray tube that is positioned using an articulating arm (Figure A.1). The fixed and linear array of seven CNT-enabled x-ray sources provided an angular span of 12$^{o}$ when positioned 40 cm from the intraoral detector. Previous work had characterized the performance of the first-generation sIOT device [Inscoe 2018]. The detector used for sIOT was a size 2 digital intraoral CMOS sensor [Handy HDR 600] with an active area of 1920 x 1440 pixels, each measuring 18.5µm.

The sIOT images were compared two commercially-available digital imaging systems, including an Instrumentarium Dental x-ray source combined with a Dentsply Sirona Schick 33 CMOS intraoral sensor to image CAR specimens and a Preva DC x-ray source utilizing a Carestream RVG 6100 CMOS intraoral sensor to image the VRF specimens. Table A.1 compares the operational parameters of these three systems.

| | CAR Imaging | | VRF Imaging | |
|---|---|---|---|---|
| | Bitewing Radiography | sIOT | Periapical Radiography | sIOT |
| Tube Voltage (kV) | 70 | 70 | 70 | 70 |
| Tube Current (mA) | 7 | 7 | 6 | 7 |
| Exposure Time (ms) | 80 | 100 | 160 | 50 |

Table A. 1. Differences in the operational settings used by the standard dental x-ray equipment for bitewing and periapical imaging and *stationary* intraoral tomosynthesis (sIOT) during studies comparing the quality of their images. Imaging was directed at extracted tooth specimens containing caries adjacent to restorations (CAR) and vertical root fractures (VRF).

The information contained in the seven projection view images was used to reconstruct a 3D image stack using a fan-volume adaptation of algebraic iteration (see 3.5.3d Reconstructing 3D images from 2D projections). Figure A.2 provides representative image slices from the reconstructed 3D stack of a cadaveric mandible.

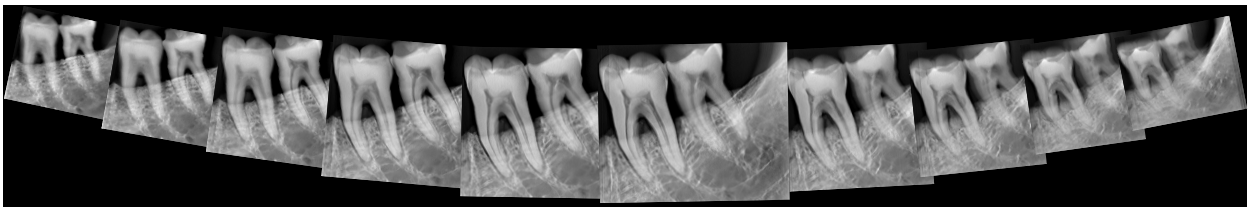

Figure A. 2. Example image slices of a cadaveric mandible selected from the reconstructed 3D stack generated by *stationary* intraoral tomosynthesis (sIOT). The complete stack included 45 images, through which the reader would scroll to appreciate changes through depth. Figure adapted from [Puett 2018c].

## A.5 Understanding and correcting dense-feature artifact in sIOT images

### *A.5.1 Characterizing dense-feature artifact*

Given the common presence of dense features in the oral cavity, most of the work characterizing dense-feature artifact and the development of processing to reduce it was carried out for sIOT (see A.2 3D dental imaging and the potential clinical value of the *synthetic* dental radiograph and 2.3.2 Carbon nanotube-enabled x-ray source arrays and *stationary* tomosynthesis) and then adapted for other imaging tasks. Metal artifact in reconstructed sIOT image slices appeared as a "shadow" extending off metal edges in the direction parallel to the linear x-ray source array (Figures A.3 and A.4) as well as "rippling" in out-of-plane reconstructed image slices [Puett 2018c]. Line profiles show the artifact at the boundary of the metal restoration to consist primarily of an overshoot followed by an undershoot, which is responsible for the shadowing (Figure A.3).

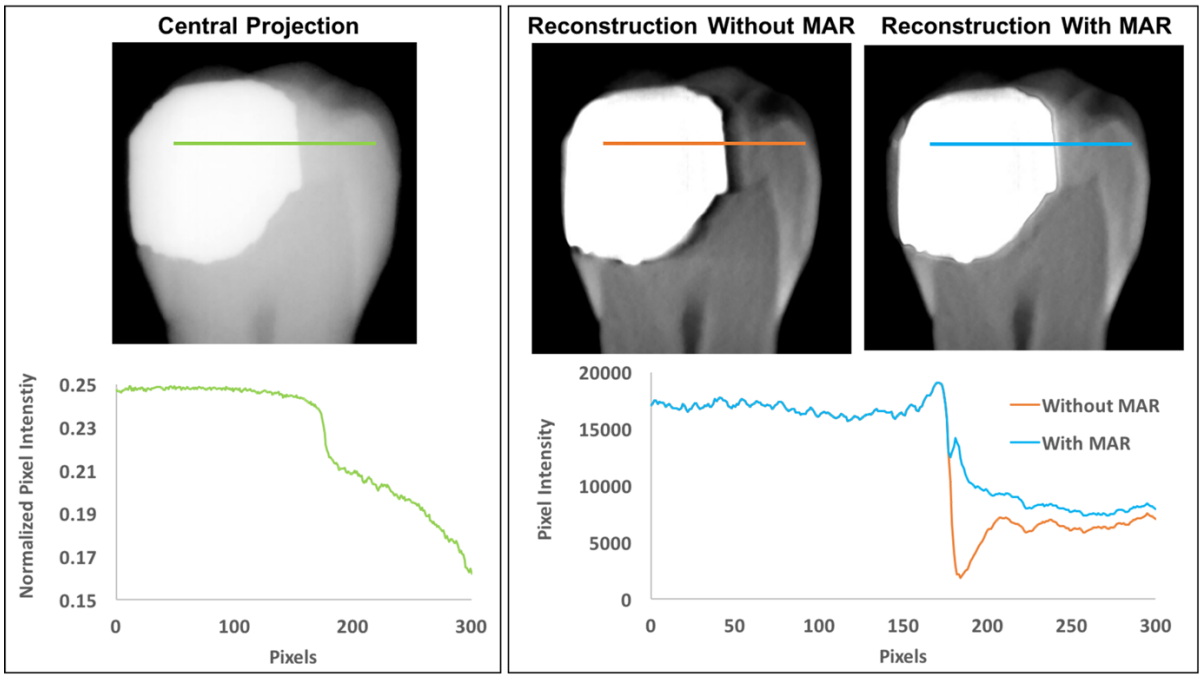


Figure A. 3. Characterizing artifact related to a metal restoration in the reconstructed image slices generated by *stationary* intraoral tomosynthesis (sIOT) as well as the effects of metal artifact reduction (MAR) through processing on image appearance. As demonstrated by the line profiles, MAR minimized the undershoot adjacent to the restoration edge. Figure adapted from [Puett 2018c].

The rounded and grooved implant-bone interface was less stark than the metal amalgam-enamel interface. Line profiles across the implant-bone interface showed minimal initial overshoot but still contained undershoot (Figure A.4). The artifact masks this boundary, a critical region requiring visualization, given the clinical concern of bone resorption.

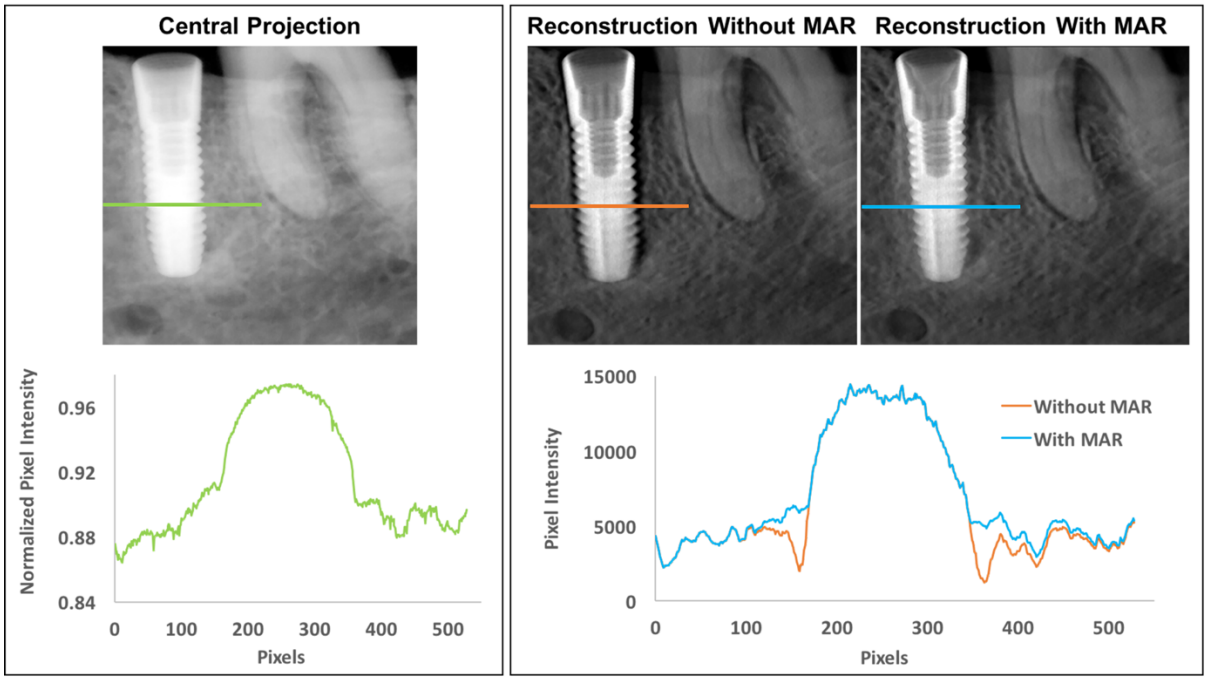


Figure A. 4. Characterizing artifact related to a metal implant in the reconstructed image slices generated by *stationary* intraoral tomosynthesis (sIOT) as well as the effects of metal artifact reduction (MAR) through processing on image appearance. As demonstrated by the line profiles, MAR decreased the undershoot adjacent to the implant (right), tending to return the profile to that of the central projection image (left). Figure adapted from [Puett 2018c].

### *A.5.2 Processing to minimize dense-feature artifact*

The processing steps to achieve metal artifact reduction (MAR) in the reconstructed image slices required manipulating images at both the projection and reconstruction levels in the processing chain, using segmentation and registration steps. First, the metal signal was segmented from one set of projection images and replaced by pixel values generated through interpolation-based in-painting prior to reconstruction. The stack of reconstructed image slices was then registered to a corresponding stack of reconstructed images generated from the same projections in which the metal signal had not been removed. The segmentation step proved difficult, given the significant variability in pixel values within the image regions containing metal, especially at the critical metal-tissue interface. As such, simple thresholding was inadequate, and region-growing algorithms using seed-points identification from the histogram

were required to identify most metallic regions correctly in the projection images, while an active contours method was used to locate the metallic boundaries [Puett 2018c].

### *A.5.3 Assessing the potential clinical benefit of dense-feature artifact reduction*

As line profiles demonstrate, MAR restored much of image region previously shadowed in the reconstructed image slice adjacent to the amalgam restoration and the metal implant (Figures A.3 and A.4). As such, features lost in the artifact became apparent after MAR. For example, the application of MAR improved the conspicuity of a carious lesion adjacent to an amalgam restoration (Figure A.5), suggesting a potential clinical benefit to its application.

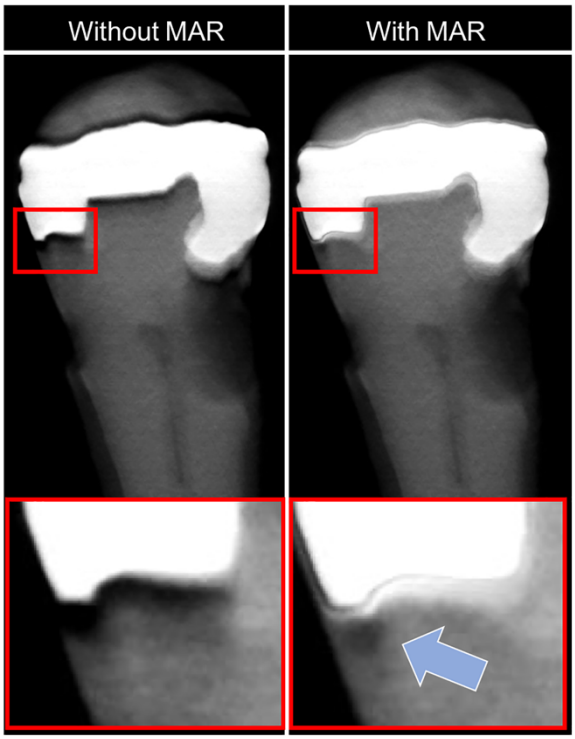


Figure A. 5. Example slices from the reconstructed stack of an extracted tooth specimen generated by *stationary* intraoral tomosynthesis (sIOT), demonstrating the effect of metal artifact reduction (MAR) through processing on the display of caries adjacent to restorations. Zooming into the image area adjacent to the metal restoration (red boxes) allows appreciation of the significant shadowing artifact. The shadowing was hiding a small region of decay, which was only apparent after MAR (blue arrow). Figure adapted from [Puett 2018c].

## A.6 Processing to generate multi-view *synthetic* dental radiographs

Although the information collected during an sIOT scan can be presented as a reconstructed 3D image stack, there are a host of potential benefits to generating and displaying the *synthetic* dental radiograph (see A.2 3D dental imaging and the potential clinical value of the *synthetic* dental radiograph). As with sDBT, *synthetic* dental radiography involves substantial image processing. However, the specific processing steps needed to generate the *synthetic* dental radiograph differed significantly from those developed for sDBT, reflecting the marked differences between these two anatomic environments as well as differences in the nature of the clinical questions being asked during breast and dental imaging. Understanding these differences and solving the processing challenges offered by them provided important lessons as the development of sDBT-based *synthetic* mammography and sIOT-based *synthetic* dental radiography evolved together.

The sIOT *synthetic* radiographs were generated by image processing chains that integrated the information available in the projection views and the reconstructed 3D image stack. Early experience with sIOT had demonstrated the value of displaying a set of *synthetic* images, each reflecting a different viewing angle, given the fact that a pathologic site may be conspicuous at one angle but quite difficult to detect at another angle [Puett 2020b]. As such, the processing chains for sIOT generated a set of multi-view *synthetic* images. This set included seven *synthetic* images, replicating the seven projection-view angles collected at the time of the scan. In this work, two different image processing chains were evaluated (Figure A.6). Each chain was optimized to display a pathology with quite different image characteristics. Caries are diffuse, lower-frequency image features, and since the processing step of reconstruction inherently emphasizes lower-frequency image components, caries lesions tend to be displayed

well in the reconstructed 3D image stack. Filtering was therefore used to enhance them prior to forward projection (Figure A.6A). However, fractures are high-frequency image features and therefore displayed best in the projection views prior to reconstruction. As such, filtering was used to isolate potentially-obscuring background features in the reconstructed image stack, which were subtracted prior to forward projection (Figure A.6B). In both cases, reconstruction was accomplished using a fan-volume adaptation of algebraic iteration customized to the unique geometry of the sIOT system.

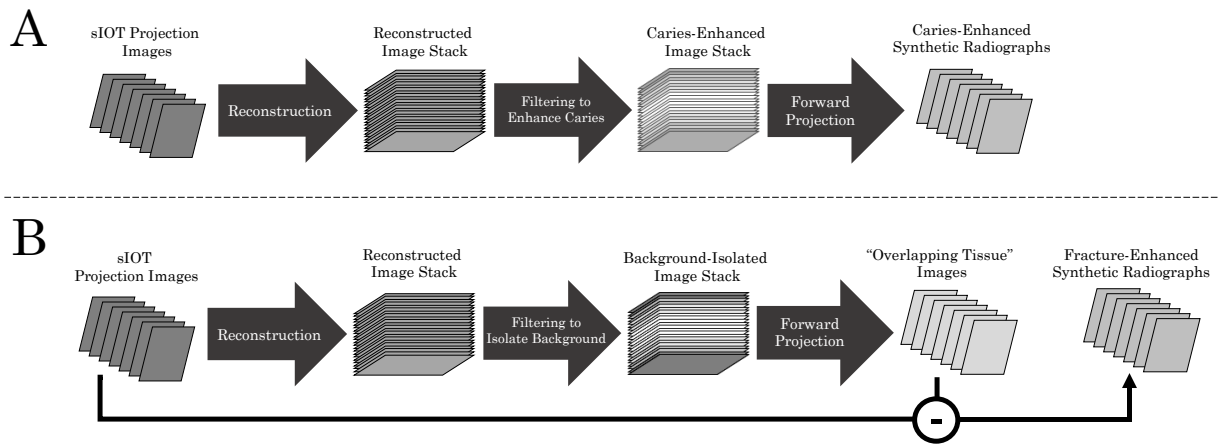


Figure A. 6. Schematic representations of the key steps in the image processing chains used to generate pathology-enhanced *synthetic* images from the information collected by *stationary* intraoral tomosynthesis (sIOT). Unique processing chains were developed for images containing caries (A) and fractures (B).

Since the individual sIOT projection images were acquired at relatively low doses, the images tended to be noisier, requiring a bilateral filtering step in order equalize the appearance of the *synthetic* image to the standard radiograph. It is important to note that this final appearance of the *synthetic* image can be quite different from the original projection view from which it was generated. Figure A.7 demonstrates this changing appearance as the information collected by sIOT of an obturated root specimen with a VRF is moved from the 2D projection level, through 3D reconstruction, and then forward projected into the *synthetic* 2D radiograph.

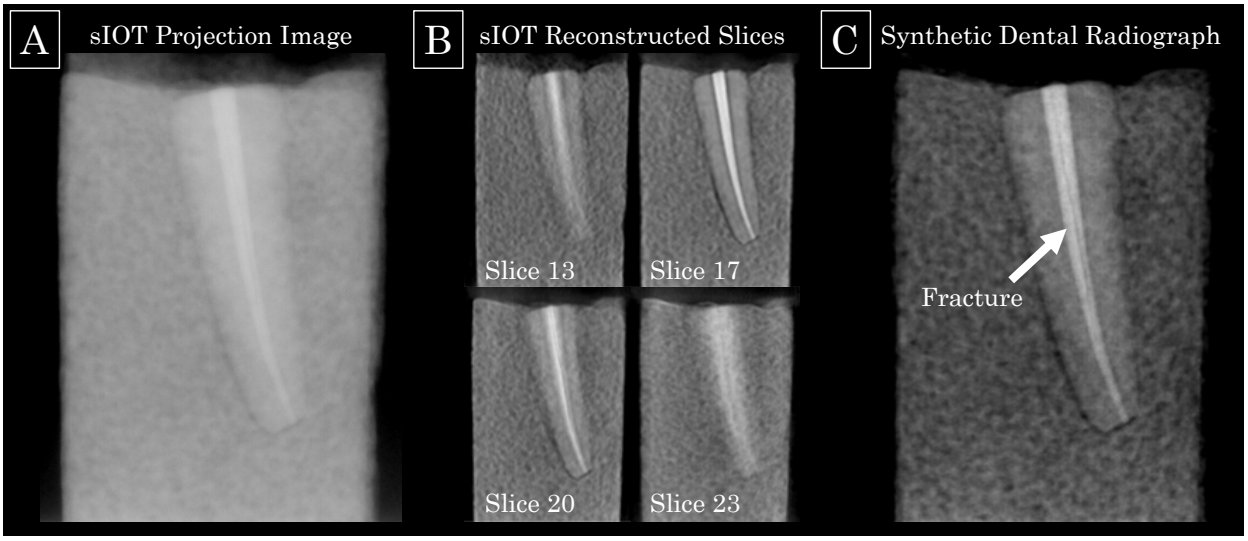


Figure A. 7. Example images of a vertical root fracture (VRF) in an obturated root specimen generated by *stationary* intraoral tomosynthesis (sIOT), demonstrating the changing appearance of the image as it moves through the processing chain. Representative images have been selected from the set of projection views (A), reconstructed 3D stack (B), and multi-view set of *synthetic* radiographs (C). The single *synthetic* image (C) corresponds to the same projection view (A). The fracture (white arrow) is best displayed in the *synthetic* dental radiograph. Figure adapted from [Puett 2020b].

## A.7 The utility of multi-view *synthetic* dental radiographs

### *A.7.1 Minimizing artifact*

The shadowing and ringing artifacts related to restorations (Figure A.8A) and obturation material (Figure A.8C) can be quite prominent. Minimizing these artifacts in the images generated by an sIOT study was a primary motivation for the development of the *synthetic* dental image. Comparing the appearance of a reconstructed image slice to the appearance of a *synthetic* radiograph generated from the same reconstructed 3D stack (Figures A.8B and A.8D) demonstrates the effectiveness of the image processing chain to minimize dense-feature artifact in the *synthetic* images.

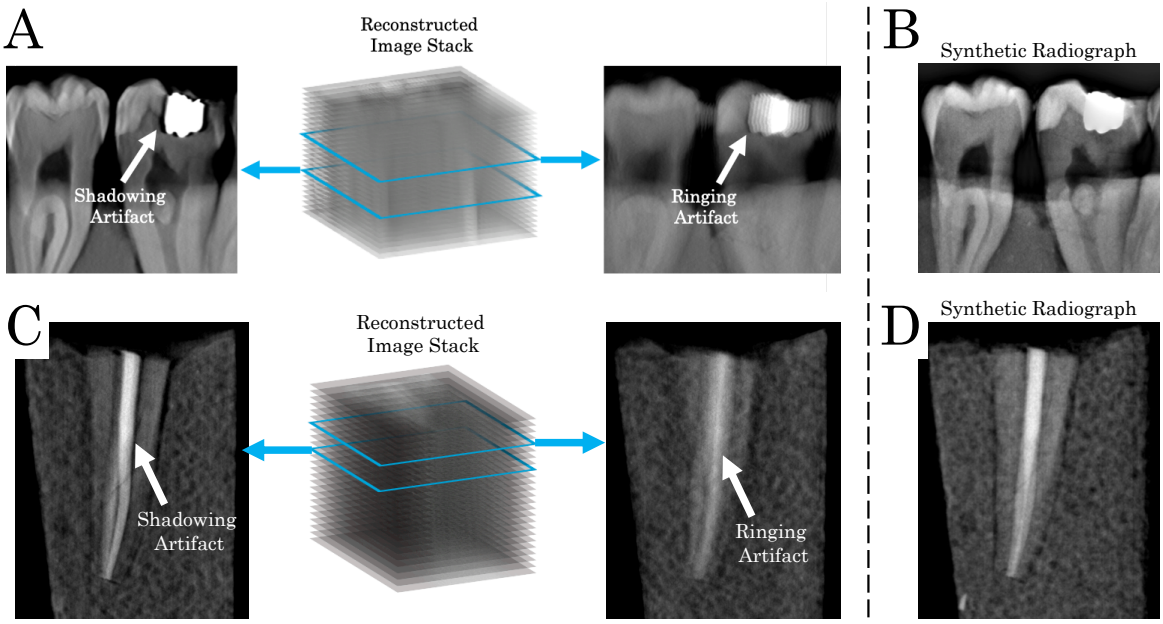


Figure A. 8. Example image slices from reconstructed 3D stacks and *synthetic* radiographs generated by *stationary* intraoral tomosynthesis (sIOT). Note the shadowing and ringing artifact associated with highly-dense features, including the metal restoration (A) and gutta-percha obturation (C). These image slices can be compared to the *synthetic* images generated from the same reconstruction stack (B and D) to appreciate the extent to which *synthetic* radiography removes these artifacts.

### *A.7.2 Seeing the interproximal space*

Evaluating the contact area between adjacent teeth can be problematic, as tooth overlap and tissue superimposition is common in the standard 2D radiograph. By providing a set of multi-view *synthetic* images across an angle span, the sIOT system is more likely to provide a better view of the proximal tooth surfaces (Figure A.9), decreasing the need for additional imaging.

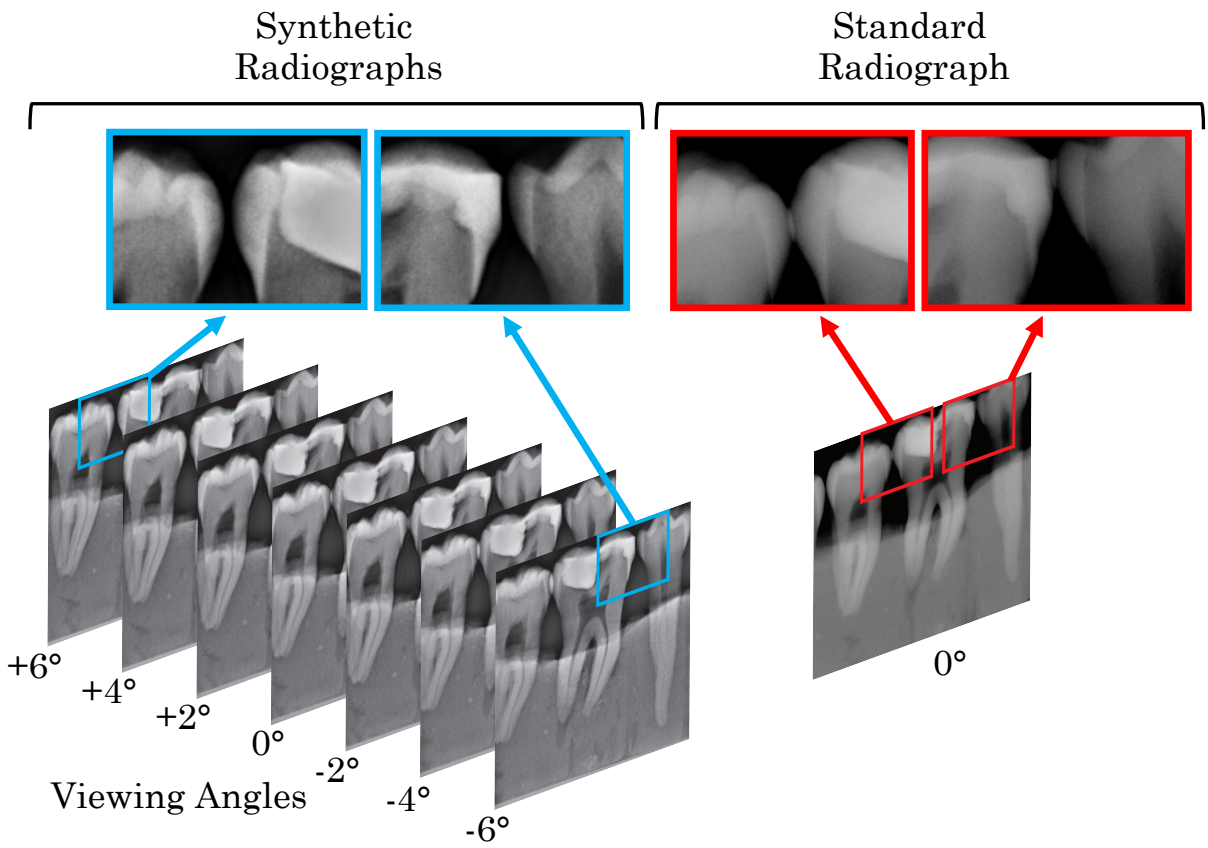


Figure A. 9. Example images comparing the *synthetic* radiographs generated by *stationary* intraoral tomosynthesis (sIOT) to standard dental radiographs of tooth specimens with restorations. The insets show the contact regions between teeth. This region can be obscured by overlapping structures in the standard radiograph (right and red). However, the multiple views provided by the set of *synthetic* radiographs (left and blue), which extends the viewing angles from -6° to +6° compared to the standard radiograph, can improve the chance of seeing the proximal surfaces well.

### *A.7.3 Displaying caries adjacent to restorations*

Figure A.10 provides a representative example of a set of multi-view synthetic radiographs of a CAR lesion. As can be appreciated, these synthetic images are free of most artifact and have a similar general appearance to a standard radiograph, thereby improving the efficiency of their review. Additionally, by integrating the information in the 3D image stack into a single image, the synthetic image tends to display the carious lesion better than the standard radiograph.

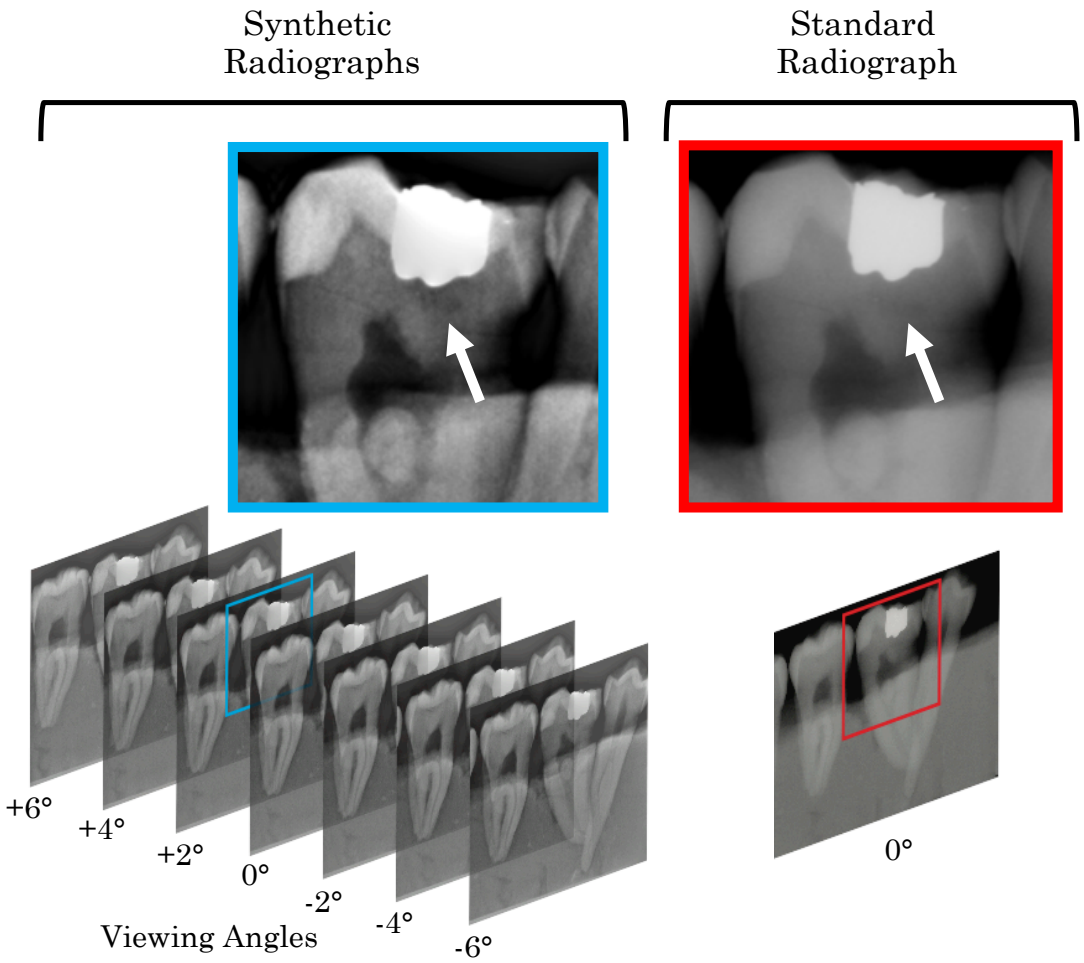


Figure A. 10. Example images comparing a set of multi-view s*ynthetic* radiographs generated by *stationary* intraoral tomosynthesis (sIOT) to the standard dental radiograph of a tooth specimen containing a caries lesion adjacent to a restoration. The *synthetic* sIOT images (left and blue) have a similar overall appearance to the standard radiograph, providing relatively artifact-free images, which display the caries adjacent to restoration (CAR) lesion compared to the better than the standard dental radiograph obtained at the same viewing angle (right and red).

### *A.7.4 Displaying vertical root fractures*

The set of multi-view *synthetic* radiographs of a non-obturated root specimen containing a VRF also includes seven images (Figure A.11). Demonstrating the value of access to a span of viewing perspectives, the VRF was best displayed in the *synthetic* radiographs representing a -6° viewing angle relative to the central projection. Similarly, identifying the fracture using standard

radiography also required collecting oblique perspectives. As such, compared to the single sIOT scan, multiple standard x-rays were needed to ensure that the same information was available.

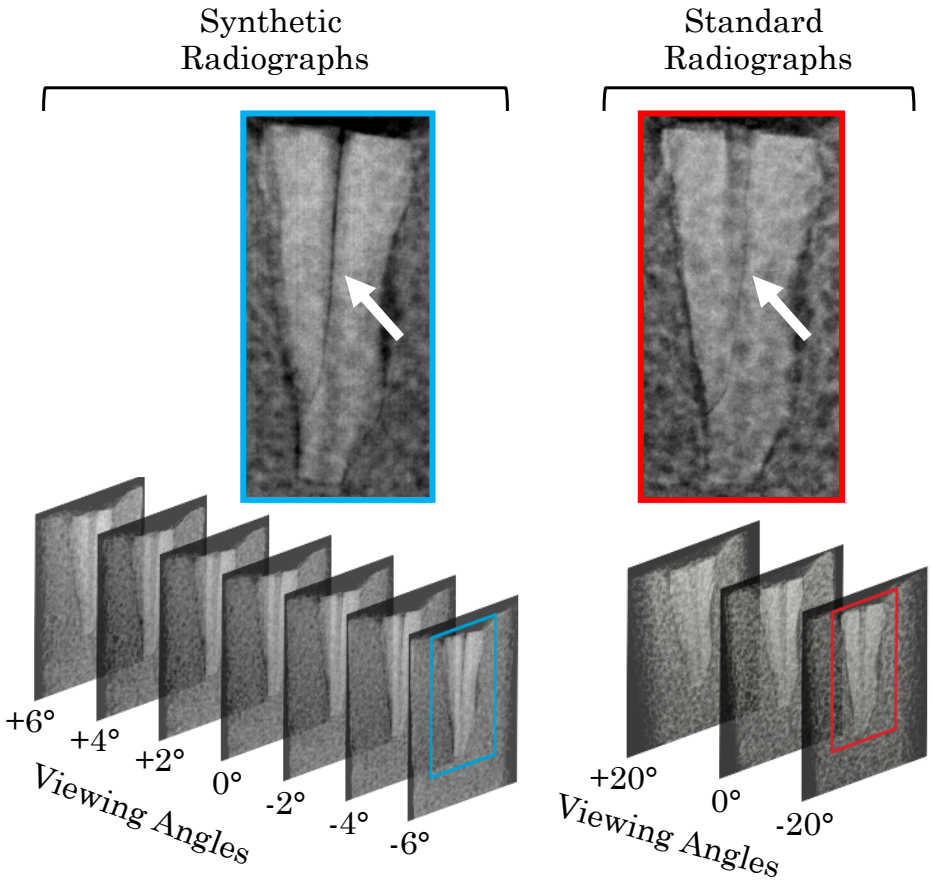


Figure A. 11. Example images comparing a set of multi-view *synthetic* radiographs generated by *stationary* intraoral tomosynthesis (sIOT) to standard dental radiographs of a non-obturated tooth root specimen with a vertical root fracture. The fracture was clearly displayed in the synthetic images generated from a single sIOT scan, particularly the -6° viewing angle (blue inset). For standard radiography, the x-ray source must be physically moved to acquire images from different angles. The fracture was best displayed in the standard radiograph acquired from a -20° viewing angle (red inset). Figure adapted from [Puett 2020b].

## A.8 Conclusions: Extending the concept of multi-view synthetic dental radiography

This dissertation work has explored the concept of displaying a set of *synthetic* images for interpretation. For breast imaging, generating multiple *synthetic* images provided an opportunity to maximize the display of diagnostically-important features with quite different

image characteristics (see 3.5.3e Forward projecting the 3D image space into *synthetic* 2D mammograms and 4.4 Incorporating *synthetic* mammography into sDBT). For dental imaging, employing different image processing chains to optimize the display of different pathologies also proved to be beneficial (see A.6 Processing to generate multi-view *synthetic* dental radiographs). However, in the case of dental imaging, presenting a set of *synthetic* images was valuable for another reason as well. It allowed for the display of different viewing perspectives (see A.7 The utility of multi-view *synthetic* dental radiographs). This ability to visualize potential pathology from different perspectives is critical in dental imaging. As such, the unique approaches of collecting dental information by sIOT combined with displaying this information as a set of multi-view *synthetic* radiographs is anticipated to have significant clinical value and forms the basis of a pending patent submission.

## REFERENCES


Acciavatti RJ, Maidment ADA. Optimization of continuous tube motion and step-and-shoot motion in digital breast tomosynthesis systems with patient motion. 2012. In: *Medical Imaging 2012: Physics of Medical Imaging*. Proc. of SPIE Vol 8313, 831306. doi:10.1117/12.911016.

American Cancer Society. Breast Cancer Facts & Figures 2019-2020. *Atlanta: American Cancer Society, Inc*. 2019.

Argus A, Mahoney M. Clinical indications for breast MRI. *Applied Radiology*. 2010. http://appliedradiology.com/articles/clinical-indications-for-breast-mri (accessed March 10, 2020).

Badano A, Graff CG, Badal A, et al. Evaluation of Digital Breast Tomosynthesis as Replacement of Full-Field Digital Mammography Using an In Silico Imaging Trial. *JAMA Netw Open*. 2018;1(7). doi:10.1001/jamanetworkopen.2018.5474.

Behling R. *Modern Diagnostic X-Ray Sources: Technology, Manufacturing, Reliability*. CRC Press; 2015.

Berg WA. Current Status of Supplemental Screening in Dense Breasts. *J Clin Oncol*. 2016;34(16):1840-1843. doi:10.1200/JCO.2015.65.8674.

Bonard J-M, Kind H, Stöckli T, Nilsson L-O. Field emission from carbon nanotubes: the first five years. *Solid-State Electronics*. 2001;45(6):893-914. doi:10.1016/S0038-1101(00)00213-6.

Boone JM, Lindfors KK, Cooper VN, Seibert JA. Scatter/primary in mammography: Comprehensive results. *Medical Physics*. 2000;27(10):2408-2416. doi:10.1118/1.1312812.

Brandan M-E, Cruz-Bastida JP, Rosado-Méndez IM, et al. Clinical study of contrast-enhanced digital mammography and the evaluation of blood and lymphatic microvessel density. *Br J Radiol*. 2016;89(1065). doi:10.1259/bjr.20160232.

Bushberg JT. The AAPM/RSNA physics tutorial for residents. X-ray interactions. *RadioGraphics*. 1998;18(2):457-468. doi:10.1148/radiographics.18.2.9536489.

Calderón-Colón X, Geng H, Gao B, An L, Cao G, Zhou O. A carbon nanotube field emission cathode with high current density and long-term stability. *Nanotechnology*. 2009;20(32):325707. doi:10.1088/0957-4484/20/32/325707.

Calliste J, Wu G, Laganis PE, et al. Second generation stationary digital breast tomosynthesis system with faster scan time and wider angular span. *Med Phys*. 2017;44(9):4482-4495. doi:10.1002/mp.12393.

Chan H-P, Helvie MA, Hadjiiski L, et al. Characterization of breast masses in digital breast tomosynthesis and digital mammograms: an observer performance study. *Acad Radiol*. 2017;24(11):1372-1379. doi:10.1016/j.acra.2017.04.016.

Chen L, Lu Y, Hu Y-H, Zhao W, Gindi G. Impact of subtraction and reconstruction strategies on dual-energy contrast enhanced breast tomosynthesis with interleaved acquisition. 2013. In: *Medical Imaging 2013: Physics of Medical Imaging*. Proc. of SPIE Vol 8668, 86685O. doi:10.1117/12.2007960.

Chen H, Danielsson M, Xu C, Cederström B. On image quality metrics and the usefulness of grids in digital mammography. *J Med Imaging*. 2015;2(1). doi:10.1117/1.JMI.2.1.013501.

Chong A, Weinstein SP, McDonald ES, Conant EF. Digital Breast Tomosynthesis: Concepts and Clinical Practice. *Radiology*. 2019;292(1):1-14. doi:10.1148/radiol.2019180760.

CIRS Imaging. BR3D Breast Imaging Phantom. CIRS. 2020a. https://www.cirsinc.com/products/mammography/br3d-breast-imaging-phantom/ (accessed January 10, 2020).

CIRS Biopsy. Stereotactic Needle Biopsy Phantom. CIRS. 2020b. https://www.cirsinc.com/products/mammography/stereotactic-needle-biopsy-phantom/ (accessed January 10, 2020).

Consumer Reports. The surprising dangers of CT Scans and X-Rays. 2015. https://www.consumerreports.org/cro/magazine/2015/01/the-surprising-dangers-of-ct-sans-and-x-rays/index.htm (accessed January 10, 2020).

Diekmann F, Meyer H, Diekmann S, et al. Thick Slices from Tomosynthesis Data Sets: Phantom Study for the Evaluation of Different Algorithms. *J Digit Imaging*. 2009;22(5):519-526. doi:10.1007/s10278-007-9075-y.

Diekmann F, Freyer M, Diekmann S, et al. Evaluation of contrast-enhanced digital mammography. *Eur J Radiol*. 2011;78(1):112-121. doi:10.1016/j.ejrad.2009.10.002.

Dobbins JT, Godfrey DJ. Digital x-ray tomosynthesis: current state of the art and clinical potential. *Phys Med Biol*. 2003;48(19):R65–R106. doi:10.1088/0031-9155/48/19/R01.

Dromain C, Balleyguier C, Muller S, et al. Evaluation of Tumor Angiogenesis of Breast Carcinoma Using Contrast-Enhanced Digital Mammography. *American Journal of Roentgenology*. 2006;187(5):W528-W537. doi:10.2214/AJR.05.1944.

Duncan J, Panahipour S. Tissue Attenuation of XRays. *Image Wisely*. 2014. https://www.imagewisely.org/Imaging-Modalities/Fluoroscopy/Tissue-Attenuation-of-XRays (accessed January 23, 2020).

Durand MA. Synthesized Mammography: Clinical Evidence, Appearance, and Implementation. *Diagnostics*. 2018;8(2). doi:10.3390/diagnostics8020022.

EUREF. European Reference Organisation for Quality Assured Breast Screening and Diagnostic Services. Tomosynthesis Protocol version 1.03. 2018. https://www.euref.org/downloads. (accessed January 10, 2020).

Feng SSJ, D'Orsi CJ, Newell MS, Seidel RL, Patel B, Sechopoulos I. X-ray scatter correction in breast tomosynthesis with a precomputed scatter map library. *Med Phys*. 2014;41(3):031912. doi:10.1118/1.4866229.

Ferrari A, Bertolaccini L, Solli P, Di Salvia PO, Scaradozzi D. Digital chest tomosynthesis: the 2017 updated review of an emerging application. *Ann Transl Med*. 2018;6(5). doi:10.21037/atm.2017.08.18.

Gang GJ, Lee J, Stayman JW, et al. Analysis of Fourier-domain task-based detectability index in tomosynthesis and cone-beam CT in relation to human observer performance. *Med Phys*. 2011;38(4):1754-1768. doi:10.1118/1.3560428.

Gao Y, Babb JS, Toth HK, Moy L, Heller SL. Digital Breast Tomosynthesis Practice Patterns Following 2011 FDA Approval: A Survey of Breast Imaging Radiologists. *Acad Radiol*. 2017;24(8):947-953. doi:10.1016/j.acra.2016.12.011.

Garrison JB, Grant DG, Guier WH, Johns RJ. Three dimensional roentgenography. *American Journal of Roentgenology*. 1969;105(4):903-908. doi:10.2214/ajr.105.4.903.

Geiser WR, Einstein SA, Yang W-T. Artifacts in Digital Breast Tomosynthesis. *American Journal of Roentgenology*. 2018;211(4):926-932. doi:10.2214/AJR.17.19271.

Gennaro G, Bernardi D, Houssami N. Radiation dose with digital breast tomosynthesis compared to digital mammography: per-view analysis. *Eur Radiol*. 2018;28(2):573-581. doi:10.1007/s00330-017-5024-4.

Geras KJ, Mann RM, Moy L. Artificial Intelligence for Mammography and Digital Breast Tomosynthesis: Current Concepts and Future Perspectives. *Radiology*. 2019;293(2):246-259. doi:10.1148/radiol.2019182627.

Gilbert FJ, Tucker L, Gillan MG, et al. The TOMMY trial: a comparison of TOMosynthesis with digital MammographY in the UK NHS Breast Screening Programme – a multicentre retrospective reading study comparing the diagnostic performance of digital breast tomosynthesis and digital mammography with digital mammography alone. *Health Technology Assessment*. 2015;19(4):1-136. doi:10.3310/hta19040.

Gold RH, Bassett LW, Widoff BE. Highlights from the history of mammography. *RadioGraphics*. 1990;10(6):1111-1131. doi:10.1148/radiographics.10.6.2259767.

Gunnell ET, Franceschi DK, Inscoe CR, et al. Initial clinical evaluation of stationary digital chest tomosynthesis in adult patients with cystic fibrosis. *Eur Radiol*. 2019;29(4):1665-1673. doi:10.1007/s00330-018-5703-9.

Hartman AE, Shan J, Wu G, et al. Initial clinical evaluation of stationary digital chest tomosynthesis. 2016. In: *Medical Imaging 2016: Physics of Medical Imaging*. Proc. of SPIE Vol 9783, 978366. doi:10.1117/12.2216850.

Hassan SA, Sayed MS, Abdalla MI, Rashwan MA. Detection of breast cancer mass using MSER detector and features matching. *Multimed Tools Appl*. 2019;78(14):20239-20262. doi:10.1007/s11042-019-7358-1.

Hekmatian E, Karbasi kheir M, Fathollahzade H, Sheikhi M. Detection of Vertical Root Fractures Using Cone-Beam Computed Tomography in the Presence and Absence of Gutta-Percha. *The Scientific World Journal*. doi:10.1155/2018/1920946.

Hellquist BN, Duffy SW, Abdsaleh S, et al. Effectiveness of population-based service screening with mammography for women ages 40 to 49 years. *Cancer*. 2011;117(4):714-722. doi:10.1002/cncr.25650.

Hendrick RE. Radiation Doses and Cancer Risks from Breast Imaging Studies. *Radiology*. 2010;257(1):246-253. doi:10.1148/radiol.10100570.

Henrot P, Leroux A, Barlier C, Génin P. Breast microcalcifications: The lesions in anatomical pathology. *Diagnostic and Interventional Imaging*. 2014;95(2):141-152. doi:10.1016/j.diii.2013.12.011.

Hill ML, Mainprize JG, Yaffe MJ. System Calibration for Quantitative Contrast-Enhanced Digital Breast Tomosynthesis (CEDBT). IWDM 2016. *Breast Imaging*. Vol 9699, 645-653.

Hilton R. Detection of Caries Adjacent to Tooth Colored Proximal Restorations Using Stationary Intraoral Tomosynthesis. 2019. The University of North Carolina at Chapel Hill. https://cdr.lib.unc.edu/concern/dissertations/70795d422 (accessed February 19, 2020).

Hologic. 3DQuorum Imaging Technology. 2020. https://www.hologic.com/hologic-products/breast-skeletal/3dquorum-imaging-technology. (accessed February 26, 2020).

Homann H, Bergner F, Erhard K. Computation of synthetic mammograms with an edge-weighting algorithm. 2015. In: *Medical Imaging 2015: Physics of Medical Imaging*. Proc. of SPIE Vol 9412, 94121Q. doi:10.1117/12.2081797.

Horvat JV, Keating DM, Rodrigues-Duarte H, Morris EA, Mango VL. Calcifications at Digital Breast Tomosynthesis: Imaging Features and Biopsy Techniques. *RadioGraphics*. 2019;39(2):307-318. doi:10.1148/rg.2019180124.

Hubbard RA, Kerlikowske K, Flowers CI, Yankaskas BC, Zhu W, Miglioretti DL. Cumulative probability of false-positive recall or biopsy recommendation after 10 years of screening mammography: a cohort study. *Ann Intern Med*. 2011;155(8):481-492. doi:10.7326/0003-4819-155-8-201110180-00004.

IARC Working Group. *Breast Cancer Screening*. Vol 15. Lyon: IARC Press; 2016. http://publications.iarc.fr/Book-And-Report-Series/Iarc-Handbooks-Of-Cancer-Prevention/Breast-Cancer-Screening-2016 (accessed March 10, 2020).

iCAD. PowerLook Tomo Detection Software Labeling and User Manual (Revision C). 2017. https://www.accessdata.fda.gov/cdrh_docs/pdf16/P160009C.pdf (accessed February 26, 2020).

Ikejimba LC, Kiarashi N, Ghate SV, Samei E, Lo JY. Task-based strategy for optimized contrast enhanced breast imaging: analysis of six imaging techniques for mammography and tomosynthesis. *Med Phys*. 2014;41(6):061908. doi:10.1118/1.4873317.

Inscoe CR, Tucker AW, Zhou OZ, Lu J. Demonstration of a scatter correction technique in digital breast tomosynthesis. 2013. In: *Medical Imaging 2013: Physics of Medical Imaging*. Proc. of SPIE Vol In: Vol 8668, 86680H. doi:10.1117/12.2008044.

Inscoe CR, Platin E, Mauriello SM, et al. Characterization and preliminary imaging evaluation of a clinical prototype stationary intraoral tomosynthesis system. *Medical Physics*. 2018;45(11):5172-5185. doi:10.1002/mp.13214.

Inscoe CR, Puett C, Billingsley A, et al. Evaluation of patient-specific scatter-corrected digital chest tomosynthesis. 2020a. In: *Medical Imaging 2020: Physics of Medical Imaging*. Proc. of SPIE Vol 11312, 1131224. doi:10.1117/12.2549316.

Inscoe CR, Billingsley A, Puett C, et al. Preliminary imaging evaluation of a compact tomosynthesis system for potential point-of-care extremity imaging. 2020b. In: *Medical Imaging 2020: Physics of Medical Imaging*. Proc. of SPIE Vol 11312, 1131204. doi:10.1117/12.2549329.

James JJ, Giannotti E, Chen Y. Evaluation of a computer-aided detection (CAD)-enhanced 2D synthetic mammogram: comparison with standard synthetic 2D mammograms and conventional 2D digital mammography. *Clin Radiol*. 2018;73(10):886-892. doi:10.1016/j.crad.2018.05.028.

Jardines L, Goyal S, Fisher P, et al. Breast Cancer Overview: Risk Factors, Screening, Genetic Testing, and Prevention. Cancer Network. https://www.cancernetwork.com/cancer-management/breast-cancer-overview-risk-factors-screening-genetic-testing-and-prevention (accessed March 10, 2020). 2015.

Jones JGA, Mills CN, Mogensen MA, Lee CI. Radiation Dose from Medical Imaging: A Primer for Emergency Physicians. *West J Emerg Med*. 2012;13(2):202-210. doi:10.5811/westjem.2011.11.6804.

Jong RA, Yaffe MJ, Skarpathiotakis M, et al. Contrast-enhanced digital mammography: initial clinical experience. *Radiology*. 2003;228(3):842-850. doi:10.1148/radiol.2283020961.

Kerlikowske K, Miglioretti DL, Vachon CM. Discussions of Dense Breasts, Breast Cancer Risk, and Screening Choices in 2019. *JAMA*. 2019;322(1):69-70. doi:10.1001/jama.2019.6247.

Kim Y, Park H, Lee H-H, et al. Comparison study of reconstruction algorithms for prototype digital breast tomosynthesis using various breast phantoms. *La radiologia medica*. 2016;121(2):81-92. doi:10.1007/s11547-015-0583-4.

Kinnas C. CT Scanner Service Cost Price Info. 2019. https://info.blockimaging.com/bid/95421/ct-scanner-service-cost-price-info (accessed January 10, 2020).

Kopans D, Gavenonis S, Halpern E, Moore R. Calcifications in the breast and digital breast tomosynthesis. *Breast J*. 2011;17(6):638-644. doi:10.1111/j.1524-4741.2011.01152.x.

Krupinski EA, Astley S, Marti R, Tornai MP, Zwiggelaar R. Special Section Guest Editorial: Advances in Breast Imaging. *JMI*. 2019;6(3):031401. doi:10.1117/1.JMI.6.3.031401.

Kuo J, Ringer PA, Fallows SG, Bakic PR, Maidment ADA, Ng S. Dynamic reconstruction and rendering of 3D tomosynthesis images. 2011. In: *Medical Imaging 2011: Physics of Medical Imaging*. Proc. of SPIE Vol 7961, 796116. doi:10.1117/12.878910.

Landis JR, Koch GG. The Measurement of Observer Agreement for Categorical Data. *Biometrics*. 1977;33(1):159-174. doi:10.2307/2529310.

Larke FJ, Kruger RL, Cagnon CH, et al. Estimated Radiation Dose Associated With Low-Dose Chest CT of Average-Size Participants in the National Lung Screening Trial. *American Journal of Roentgenology*. 2011;197(5):1165-1169. doi:10.2214/AJR.11.6533.

Lee YZ, Puett C, Inscoe CR, et al. Initial Clinical Experience with Stationary Digital Breast Tomosynthesis. *Acad Radiol*. 2019;26(10):1363-1372. doi:10.1016/j.acra.2018.12.026.

Lee YZ, Gunnell ET, Inscoe CR, Puett C, Lu J, Zhou O. Initial clinical evaluation of gated stationary digital chest tomosynthesis. 2018. In: *Medical Imaging 2018: Physics of Medical Imaging*. Proc. of SPIE Vol 10573, 105730I. doi:10.1117/12.2293713.

Lehman CD, Arao RF, Sprague BL, et al. National Performance Benchmarks for Modern Screening Digital Mammography: Update from the Breast Cancer Surveillance Consortium. *Radiology*. 2016;283(1):49-58. doi:10.1148/radiol.2016161174.

Lindfors KK, Boone JM, Newell MS, D'Orsi CJ. Dedicated breast CT: The optimal cross sectional imaging solution? *Radiol Clin North Am*. 2010;48(5):1043-1054. doi:10.1016/j.rcl.2010.06.001.

Liu S, Wang H, Feng W, et al. The value of X-ray digital tomosynthesis in the diagnosis of urinary calculi. *Exp Ther Med*. 2018;15(2):1749-1753. doi:10.3892/etm.2017.5531.

Lloyd S. Least squares quantization in PCM. *IEEE Transactions on Information Theory*. 1982;28(2):129-137. doi:10.1109/TIT.1982.1056489.

Lu Y, Peng B, Lau BA, et al. A scatter correction method for contrast-enhanced dual-energy digital breast tomosynthesis. *Phys Med Biol*. 2015;60(16):6323-6354. doi:10.1088/0031-9155/60/16/6323.

Luo Y, Spronk D, Lee YZ, et al. Simulation and optimization of system configuration for the stationary head CT using CNT x-ray source array: reconstruction and quality evaluation. 2020. In: *Medical Imaging 2020: Physics of Medical Imaging*. Proc. of SPIE Vol 11312, 1131238. doi:10.1117/12.2549996.

Mackenzie A, Marshall NW, Hadjipanteli A, Dance DR, Bosmans H, Young KC. Characterisation of noise and sharpness of images from four digital breast tomosynthesis systems for simulation of images for virtual clinical trials. *Phys Med Biol*. 2017;62(6):2376-2397. doi:10.1088/1361-6560/aa5dd9.

Mainiero MB, Moy L, Baron P, et al. ACR Appropriateness Criteria Breast Cancer Screening. *J Am Coll Radiol*. 2017;14(11S):S383-S390. doi:10.1016/j.jacr.2017.08.044.

Marchiori D. *Clinical Imaging - E-Book: With Skeletal, Chest and Abdomen Pattern Differentials*. Elsevier Health Sciences; 2004.

Marshall NW, Bosmans H. Measurements of system sharpness for two digital breast tomosynthesis systems. *Phys Med Biol*. 2012;57(22):7629. doi:10.1088/0031-9155/57/22/7629.

Mauriello S, Platin E, Broome A, et al. Use of Stationary Digital Intraoral Tomosynthesis (sIOT) for Bitewing Radiography. 2018. https://iadr2018.zerista.com/event/member/491099 (accessed February 24, 2020).

Mauriello S, Broome A, Platin E, et al. The role of stationary intraoral tomosynthesis in reducing proximal overlap in bitewing radiography. *Dentomaxillofacial Radiology*. 2020;20190504. doi:10.1259/dmfr.20190504.

McCollough CH, Bushberg JT, Fletcher JG, Eckel LJ. Answers to Common Questions About the Use and Safety of CT Scans. *Mayo Clinic Proceedings*. 2015;90(10):1380-1392. doi:10.1016/j.mayocp.2015.07.011.

Michael J. Thali, Brogdon BG, Viner MD. *Forensic Radiology*. CRC Press; 2002.

Michaelides L. Inventions: Diagnostic X-Rays. 2009. https://engineering.dartmouth.edu/magazine/inventions-diagnostic-x-rays/ (accessed March 10, 2020).

Mol A, Gaalaas L, Platin E, et al. Intraoral tomosynthesis using carbon nanotube (CNT) X-ray technology: Primary caries detection. *American Academy of Oral and Maxillorfacial Radiology*. 2015.

Nair MK, Tyndall DA, Ludlow JB, May K, Ye F. The effects of restorative material and location on the detection of simulated recurrent caries. A comparison of dental film, direct digital radiography and tuned aperture computed tomography. *Dentomaxillofac Radiol*. 1998;27(2):80-84. doi:10.1038/sj/dmfr/4600323.

Nalawade YV. Evaluation of breast calcifications. *Indian J Radiol Imaging*. 2009;19(4):282-286. doi:10.4103/0971-3026.57208.

Nascimento MLF. Brief history of X-ray tube patents. *World Patent Information*. 2014;37:48-53. doi:10.1016/j.wpi.2014.02.008.

NDT. History of Radiography. 2014. https://www.nde-ed.org/EducationResources/CommunityCollege/Radiography/Introduction/history.htm (accessed March 10, 2020).

Nobel Media. The Nobel Prize in Physics 1901. NobelPrize.org. 2020. https://www.nobelprize.org/prizes/physics/1901/summary/ (accessed March 10, 2020).

Noone AM, Howlader N, Krapcho M, et al. SEER Cancer Statistics Review, 1975-2015, National Cancer Institute. 2018. https://seer.cancer.gov/csr/1975_2015/ (accessed March 10, 2020).

Otto SJ, Fracheboud J, Verbeek ALM, et al. Mammography Screening and Risk of Breast Cancer Death: A Population-Based Case–Control Study. *Cancer Epidemiol Biomarkers Prev*. 2011. doi:10.1158/1055-9965.EPI-11-0476.

Park Y-S, Ahn J-S, Kwon H-B, Lee S-P. Current status of dental caries diagnosis using cone beam computed tomography. *Imaging Sci Dent*. 2011;41(2):43-51. doi:10.5624/isd.2011.41.2.43.

Parmee RJ, Collins CM, Milne WI, Cole MT. X-ray generation using carbon nanotubes. *Nano Convergence*. 2015;2(1):1. doi:10.1186/s40580-014-0034-2.

Peppard HR, Nicholson BE, Rochman CM, Merchant JK, Mayo RC, Harvey JA. Digital Breast Tomosynthesis in the Diagnostic Setting: Indications and Clinical Applications. *RadioGraphics*. 2015;35(4):975-990. doi:10.1148/rg.2015140204.

Pesce M, Wang X, Rowland P. Using Carbon Nano-Tube Field Emitters to Miniaturize X-Ray Tubes. 2017. Carestream White Paper.

PHE. NHS Breast Screening Programme Equipment Report: Technical evaluation of Hologic 3Dimensions digital breast tomosynthesis system. 2019. https://assets.publishing.service.gov.uk/government/uploads/system/uploads/attachment_data/file/788832/Technical_evaluation_of_Hologic_3Dimensions_digital_breast_tomosynthesis_system.pdf (accessed March 10, 2020).

Pisano ED, Gatsonis C, Hendrick E, et al. Diagnostic Performance of Digital versus Film Mammography for Breast-Cancer Screening. *NEJM*. 2005;353(17):1773-1783. doi:10.1056/NEJMoa052911.

Power SP, Moloney F, Twomey M, James K, O'Connor OJ, Maher MM. Computed tomography and patient risk: Facts, perceptions and uncertainties. *World J Radiol*. 2016;8(12):902-915. doi:10.4329/wjr.v8.i12.902.

Puett C, Calliste J, Wu G, et al. Contrast enhanced imaging with a stationary digital breast tomosynthesis system. 2017. In: *Medical Imaging 2018: Physics of Medical Imaging*. Proc. of SPIE Vol 10132, 1013225. doi:10.1117/12.2254348.

Puett C, Inscoe C, Hartman A, et al. An update on carbon nanotube-enabled X-ray sources for biomedical imaging. *Wiley Interdiscip Rev Nanomed Nanobiotechnol*. 2018a;10(1). doi:10.1002/wnan.1475.

Puett C, Inscoe C, Lee YZ, Zhou O, Lu J. Phantom-based study exploring the effects of different scatter correction approaches on the reconstructed images generated by contrast-enhanced stationary digital breast tomosynthesis. *J Med Imaging*. 2018b;5(1):013502. doi:10.1117/1.JMI.5.1.013502.

Puett C, Inscoe C, Hilton R, et al. Stationary digital intraoral tomosynthesis: demonstrating the clinical potential of the first-generation system. 2018c. In: *Medical Imaging 2018: Physics of Medical Imaging*. Proc. of SPIE Vol 10573, 105730E. doi:10.1117/12.2293722.

Puett C, Gao J, Tucker A, et al. Visualizing microcalcifications in lumpectomy specimens: an exploration into the clinical potential of carbon nanotube-enabled stationary digital breast tomosynthesis. *Biomed Phys Eng Express*. 2019a;5(4):045040. doi:10.1088/2057-1976/ab3320.

Puett C, Inscoe C, Lu J, Lee Y, Zhou O. Generating synthetic mammograms for stationary 3D mammography. 2019b. In: *Medical Imaging 2019: Physics of Medical Imaging*. Proc. of SPIE Vol 10948, 1094807. doi:10.1117/12.2513017.

Puett C, Inscoe C, Lu J, et al. Advancing synthetic mammography for stationary digital breast tomosynthesis. 2020a. In: *Medical Imaging 2020: Physics of Medical Imaging*. Proc. of SPIE Vol 11312, 113125F. doi:10.1117/12.2549421.

Puett C, Inscoe C, Perrone L, et al. Displaying information collected by intraoral tomosynthesis as multi-view synthetic radiographs. 2020b. In: *Medical Imaging 2020: Physics of Medical Imaging*. Proc. of SPIE Vol 11312, 113122R. doi:10.1117/12.2549417.

Qian X, Rajaram R, Calderon-Colon X, et al. Design and characterization of a spatially distributed multibeam field emission x-ray source for stationary digital breast tomosynthesis. *Med Phys*. 2009;36(10):4389-4399. doi:10.1118/1.3213520.

Qian X, Tucker A, Gidcumb E, et al. High resolution stationary digital breast tomosynthesis using distributed carbon nanotube x-ray source array. *Medical Physics*. 2012;39(4):2090-2099. doi:10.1118/1.3694667.

Ratanaprasatporn L, Chikarmane SA, Giess CS. Strengths and Weaknesses of Synthetic Mammography in Screening. *RadioGraphics*. 2017;37(7):1913-1927. doi:10.1148/rg.2017170032.

Regan Anderson M. Stationary intraoral tomosynthesis imaging for vertical root fracture detection. 2017. University of Minnesota. http://conservancy.umn.edu/handle/11299/191233 (accessed January 7, 2020).

Rodríguez-Ruiz A, Krupinski E, Mordang J-J, et al. Detection of Breast Cancer with Mammography: Effect of an Artificial Intelligence Support System. *Radiology*. 2018;290(2):305-314. doi:10.1148/radiol.2018181371.

Rodriguez-Ruiz A, Lång K, Gubern-Merida A, et al. Stand-Alone Artificial Intelligence for Breast Cancer Detection in Mammography: Comparison With 101 Radiologists. *J Natl Cancer Inst*. 2019;111(9):916-922. doi:10.1093/jnci/djy222.

Röntgen WC. ON A NEW KIND OF RAYS. *Science*. 1896;3(59):227-231. doi:10.1126/science.3.59.227.

Saslow D, Boetes C, Burke W, et al. American Cancer Society Guidelines for Breast Screening with MRI as an Adjunct to Mammography. *CA: A Cancer Journal for Clinicians*. 2007;57(2):75-89. doi:10.3322/canjclin.57.2.75.

Schulze R, Heil U, Groβ D, et al. Artefacts in CBCT: a review. *Dentomaxillofac Radiol*. 2011;40(5):265-273. doi:10.1259/dmfr/30642039.

Sechopoulos I, Suryanarayanan S, Vedantham S, D'Orsi CJ, Karellas A. Scatter radiation in digital tomosynthesis of the breast. *Med Phys*. 2007;34(2):564-576. doi:10.1118/1.2428404.

Sechopoulos I. X-ray scatter correction method for dedicated breast computed tomography: X-ray scatter correction for dedicated breast CT. *Medical Physics*. 2012;39(5):2896-2903. doi:10.1118/1.4711749.

Sechopoulos I. A review of breast tomosynthesis. Part I. The image acquisition process. *Med Phys*. 2013a;40(1). doi:10.1118/1.4770279.

Sechopoulos I. A review of breast tomosynthesis. Part II. Image reconstruction, processing and analysis, and advanced applications. *Med Phys*. 2013b;40(1):014302. doi:10.1118/1.4770281.

Shan J, Tucker AW, Lee YZ, et al. Stationary chest tomosynthesis using a carbon nanotube x-ray source array: a feasibility study. *Phys Med Biol*. 2015;60(1):81-100. doi:10.1088/0031-9155/60/1/81.

Shan J, Tucker AW, Gaalaas LR, et al. Stationary intraoral digital tomosynthesis using a carbon nanotube X-ray source array. *Dentomaxillofacial Radiology*. 2015;44(9):20150098. doi:10.1259/dmfr.20150098.

Shen L, Margolies LR, Rothstein JH, Fluder E, McBride R, Sieh W. Deep Learning to Improve Breast Cancer Detection on Screening Mammography. *Scientific Reports*. 2019;9(1):1-12. doi:10.1038/s41598-019-48995-4.

Sickles EA, D'Orsi CJ, Bassett LW. ACR BI-RADS® Mammography. In: *ACR BI-RADS Atlas, Breast Imaging Reporting and Data System*. Reston, VA: American College of Radiology; 2013.

Smith A. Synthesized 2D Mammographic Imaging: Theory and Clinical Performance. 2016. http://www.lowdose3d.com/images/C-View-White-Paper.pdf (accessed January 9, 2020).

Smith-Bindman R, Lipson J, Marcus R, et al. Radiation Dose Associated with Common Computed Tomography Examinations and the Associated Lifetime Attributable Risk of Cancer. *Arch Intern Med*. 2009;169(22):2078-2086. doi:10.1001/archinternmed.2009.427.

Spangler ML, Zuley ML, Sumkin JH, et al. Detection and classification of calcifications on digital breast tomosynthesis and 2D digital mammography: a comparison. *AJR Am J Roentgenol*. 2011;196(2):320-324. doi:10.2214/AJR.10.4656.

Sprague BL, Conant EF, Onega T, et al. Variation in mammographic breast density assessments among radiologists in clinical practice: Findings from a multicenter observational study. *Ann Intern Med*. 2016;165(7):457-464. doi:10.7326/M15-2934.

Sprenger F, Calderon X, Gidcumb E, et al. Stationary digital breast tomosynthesis with distributed field emission X-ray tube. 2011. *Proc SPIE*. 2011;7961. doi:10.1117/12.878280.

Spronk D, Luo Y, Inscoe C, et al. Feasibility of a stationary head CT scanner using a CNT x-ray source array. 2020. In: *Medical Imaging 2020: Physics of Medical Imaging*. Proc. of SPIE Vol 11312, 1131237. doi:10.1117/12.2549335.

Tabár L, Vitak B, Chen TH-H, et al. Swedish Two-County Trial: Impact of Mammographic Screening on Breast Cancer Mortality during 3 Decades. *Radiology*. 2011;260(3):658-663. doi:10.1148/radiol.11110469.

Tabár L, Yen AM-F, Wu WY-Y, et al. Insights from the breast cancer screening trials: how screening affects the natural history of breast cancer and implications for evaluating service screening programs. *Breast J*. 2015;21(1):13-20. doi:10.1111/tbj.12354.

Tagliafico A, Mariscotti G, Durando M, et al. Characterisation of microcalcification clusters on 2D digital mammography (FFDM) and digital breast tomosynthesis (DBT): does DBT underestimate microcalcification clusters? Results of a multicentre study. *Eur Radiol*. 2014;25(1):9-14. doi:10.1007/s00330-014-3402-8.

Tagliafico AS, Valdora F, Mariscotti G, et al. An exploratory radiomics analysis on digital breast tomosynthesis in women with mammographically negative dense breasts. *Breast*. 2018;40:92-96. doi:10.1016/j.breast.2018.04.016.

Tagliafico AS, Bignotti B, Rossi F, et al. Breast cancer Ki-67 expression prediction by digital breast tomosynthesis radiomics features. *Eur Radiol Exp*. 2019;3. doi:10.1186/s41747-019-0117-2.

Taşkın F, Polat Y, Erdoğdu İH, Türkdoğan FT, Öztürk VS, Özbaş S. Problem-solving breast MRI: useful or a source of new problems? *Diagn Interv Radiol*. 2018;24(5):255-261. doi:10.5152/dir.2018.17504.

The Market Reports. Global Digital Breast Tomosynthesis (DBT) System Market 2018 by Manufacturers, Regions, Type and Application, Forecast to 2023. 2018. https://www.themarketreports.com/report/global-digital-breast-tomosynthesis-dbt-system-market-2018-by-manufacturers-regions-type-and-application-forecast-to-2023 (accessed March 10, 2020).

Tucker AW, Lu J, Zhou O. Dependency of image quality on system configuration parameters in a stationary digital breast tomosynthesis system. *Med Phys*. 2013;40(3):031917. doi:10.1118/1.4792296.

Tucker AW, Calliste J, Gidcumb EM, et al. Comparison of a Stationary Digital Breast Tomosynthesis System to Magnified 2D Mammography Using Breast Tissue Specimens. *Academic Radiology*. 2014a;21(12):1547-1552. doi:10.1016/j.acra.2014.07.009.

Tucker A. Development of a Stationary Digital Breast Tomosynthesis System for Clinical Applications. 2014b. The University of North Carolina at Chapel Hill. https://pdfs.semanticscholar.org/84ec/c4a68b2123c0673665450b21b33a898650d6.pdf (accessed January 15, 2020).

Tyndall DA, Rathore S. Cone-Beam CT Diagnostic Applications: Caries, Periodontal Bone Assessment, and Endodontic Applications. *Dent Clin N Am*. 2008;52:825-841.

Ullman G, Sandborg M, Dance DR, Hunt R, Carlsson GA. Distributions of Scatter-to-Primary Ratios in Chest PA Radiography Using Grid or Air Gap for Scatter-Rejection. 2004. Report 100. Universitetet I Linkoping.

US FDA. Digital Accreditation. FDA. 2018. http://www.fda.gov/radiation-emitting-products/facility-certification-and-inspection-mqsa/digital-accreditation (accessed March 10, 2020).

van Daatselaar AN, Tyndall DA, van der Stelt PF. Detection of caries with local CT. *Dentomaxillofac Radiol*. 2003;32(4):235-241. doi:10.1259/dmfr/86813332.

Vedantham S, Karellas A, Vijayaraghavan GR, Kopans DB. Digital Breast Tomosynthesis: State of the Art. *Radiology*. 2015;277(3):663-684. doi:10.1148/radiol.2015141303.

Vera C, De Kok IJ, Chen W, Reside G, Tyndall D, Cooper LF. Evaluation of post-implant buccal bone resorption using cone beam computed tomography: a clinical pilot study. *Int J Oral Maxillofac Implants*. 2012;27(5):1249-1257.

Wallis MG, Moa E, Zanca F, Leifland K, Danielsson M. Two-view and single-view tomosynthesis versus full-field digital mammography: high-resolution X-ray imaging observer study. *Radiology*. 2012;262(3):788-796. doi:10.1148/radiol.11103514.

Webber RL, Horton RA, Tyndall DA, Ludlow JB. Tuned-aperture computed tomography (TACT). Theory and application for three-dimensional dento-alveolar imaging. *Dentomaxillofac Radiol*. 1997;26(1):53-62. doi:10.1038/sj.dmfr.4600201.

Wei J, Sahiner B, Hadjiiski LM, et al. Computer-aided detection of breast masses on full field digital mammograms. *Med Phys*. 2005;32(9):2827-2838. doi:10.1118/1.1997327.

Wei J, Chan H-P, Helvie MA, et al. Synthesizing mammogram from digital breast tomosynthesis. *Phys Med Biol*. January 2019. doi:10.1088/1361-6560/aafcda.

Wu G, Mainprize JG, Boone JM, Yaffe MJ. Evaluation of scatter effects on image quality for breast tomosynthesis. *Med Phys*. 2009;36(10):4425-4432. doi:10.1118/1.3215926.

Wu G, Inscoe C, Calliste J, Lee YZ, Zhou O, Lu J. Adapted fan-beam volume reconstruction for stationary digital breast tomosynthesis. 2015. In: *Medical Imaging 2015: Physics of Medical Imaging*. Proc of SPIE Vol 9412, 94123J. doi:10.1117/12.2081931.

Wu G, Inscoe CR, Calliste J, et al. Estimating scatter from sparsely measured primary signal. *J Med Imaging*. 2017;4(1). doi:10.1117/1.JMI.4.1.013508.

Wu T, Moore RH, Rafferty EA, Kopans DB. A comparison of reconstruction algorithms for breast tomosynthesis. *Med Phys*. 2004;31(9):2636-2647. doi:10.1118/1.1786692.

Xu S, Lu J, Zhou O, Chen Y. Statistical iterative reconstruction to improve image quality for digital breast tomosynthesis. *Med Phys*. 2015;42(9):5377-5390. doi:10.1118/1.4928603.

Yala A, Lehman C, Schuster T, Portnoi T, Barzilay R. A Deep Learning Mammography-based Model for Improved Breast Cancer Risk Prediction. *Radiology*. 2019;292(1):60-66. doi:10.1148/radiol.2019182716.

Yang G, Qian X, Phan T, et al. Design and feasibility studies of a stationary digital breast tomosynthesis system. *Nucl Instrum Methods Phys Res A*. 2011;648(Suppl 1):S220-S223. doi:10.1016/j.nima.2010.11.147.

Yang K, Burkett Jr George, Boone JM. An object specific and dose-sparing scatter correction approach for a dedicated cone-beam breast CT system using a parallel-hole collimator. In: *Medical Imaging 2012: Physics of Medical Imaging*. Proc of SPIE Vol 8313, 831303. doi:10.1117/12.911093.

Zhang X-H, Xiao C. Diagnostic Value of Nineteen Different Imaging Methods for Patients with Breast Cancer: a Network Meta-Analysis. *Cell Physiol Biochem*. 2018;46(5):2041-2055. doi:10.1159/000489443.

Zheng J, Fessler JA, Chan H-P. Effect of source blur on digital breast tomosynthesis reconstruction. *Medical Physics*. 2019;46(12):5572-5592. doi:10.1002/mp.13801.

Zhou J, Zhao B, Zhao W. A computer simulation platform for the optimization of a breast tomosynthesis system. *Med Phys*. 2007;34(3):1098-1109. doi:10.1118/1.2558160.

Zhou O, Calderon-Colon X. Carbon Nanotube-Based Field Emission X-Ray Technology. In: Saito Y, ed. *Carbon Nanotube and Related Field Emitters*. Weinheim, Germany: Wiley-VCH Verlag GmbH & Co. KGaA; 2010:417-437. doi:10.1002/9783527630615.ch26.